DISSERTATION

MULTISCALE STUDY OF THE PEARLITIC MICROSTRUCTURE IN CARBON STEELS: ATOMISTIC INVESTIGATION AND CONTINUUM MODELING OF IRON AND IRON-CARBIDE INTERFACES

Submitted by
Matthew Guziewski
Department of Mechanical Engineering

In partial fulfillment of the requirements
For the Degree of Doctor of Philosophy
Colorado State University
Fort Collins, Colorado
Summer 2018

Doctoral Committee:

Advisor: Dr. Christopher Weinberger

Dr. Paul Heyliger
Dr. Arun Kota
Dr. Kaka Ma

ABSTRACT

MULTISCALE STUDY OF THE PEARLITIC MICROSTRUCTURE IN CARBON STEELS: ATOMISTIC INVESTIGATION AND CONTINUUM MODELING OF IRON AND IRON-CARBIDE INTERFACES

While the behavior of carbon steel has been studied extensively for decades, there are still many questions regarding its microstructures. As such, classical atomistics is utilized to obtain further insight into the energetics, structure, and mechanical response of the various interfaces between iron and iron-carbides. Simulations were constructed for the commonly reported orientation relationships between ferrite and cementite within pearlite: the Bagaryatskii, the Isaichev, and the Pitsch-Petch, as well as their associated near orientations. Dislocation arrays are found to form for all orientation relationships, with their spacing and direction a function of lattice mismatch. Within each orientation relationship, different interfacial chemistries are found to produce identical dislocation spacings and line directions, but differing interfacial energies. This chemistry component to the interfacial energy is characterized and it is determined that in addition to the lattice mismatch, there are two structural factors within the cementite terminating plane that affect the energetics: the presence of like site iron pairs and proximity of carbon atoms to the interface. Additionally, an alternate method for determining the interfacial energy of systems in which there are multiple chemical potentials for a single element is developed and implemented, an approach which is likely valid for other similar systems. Atomistics finds the Isaichev orientation relationship to be the most favorable, while the “near" orientation relationships are found to be at least as energetically favorable as their parent orientation relationships. A continuum model based on O-lattice theory and anisotropic continuum theory is also applied to the atomistic results, yielding interfacial energy approximations that match well with those from atomistics and allowing for the characterization of the Burgers vectors, which are found to lie in high symmetry directions of the ferrite on the interface plane. The continuum model also allowed for the analysis of the system with changing lattice and elastic constants. This revealed that while most of the orientations had relatively small variation in their energetics with these changes, the Isaichev orientation was in fact very sensitive to variations in the lattice constants. The use of temperature dependent values for lattice and elastic constants suggested that while the Isaichev is most favorable at low tempertaures, other orientations may become more favorable at high temperatures. This combined atomistic/continuum approach was also applied to the austenite-cementite system and used to compare the proposed habit planes of both the Pitsch and Thompson-Howell orientation relationships. This analysis found the two orientation relationships to be unique, a point of previous contention, with the Pitsch the more favorable.

Atomistic modeling was further used to investigate the mechanical response to compressive and tensile straining of the pearlitic orientation relationships. A range of interlamellar spacings and ferrite to cementite ratios are considered, and values for important mechanical properties including elastic modulus, yield stress, flow stress, and ductility are determined. Mechanical properties are shown to be largely dependent on only the volume ratios of the cementite and ferrite, with the interlamellar spacing having an increasing role as it reaches smaller values. Slip systems and Schmid factors are determined for a variety of loading states in both the transverse and longitudinal directions and were used to fit to simple elasto-plastic models. Transverse loading is observed to follow simple 1-D composite theory, while longitudinal loading requires the consideration of the strain compatibility of the interface. Orientation, and specifically the alignment of slip planes in the ferrite and cementite, was also determined to play a role in the mechanical response. Alignment of favorable slip planes in the cementite, notably the $\{100\}_\theta$ and $\{110\}_\theta$, with high symmetry directions in the ferrite was found to greatly enhance the ductility of the system in longitudinal loading, as well as allow for lower flow stresses in transverse loading.

ACKNOWLEDGEMENTS

I would first like to express my sincere gratitude to my advisor, Professor Christopher Weinberger, for his invaluable guidance, inspiration and encouragement during the work. Without his motivation and quest for excellence, this work would have never been fruitful. I would also like to thank both the past and present members of my research group, especially Ian Bakst and Hang Yu, for the insightful conversations and general camaraderie they provided.

Additionally, I'd like to recognize the members of my committee, Dr. Paul Heyliger, Dr. Arun Kota, and Dr. Kaka Ma, for there useful input and guidance during this process, as well as Dr. Shawn Coleman for his collaboration and mentoring.

This research was supported though a grant from the Petroleum Research Fund, PRF #54697-DNI10, as well as through resources provided through collaboration with the Army Research Laboratory under the DoD High Performance Computing Modernization Program. The work utilized the RMACC Summit supercomputer, supported by the National Science Foundation, the University of Colorado Boulder and Colorado State University, as well as Drexel University's University Computing Facility.

Some of the work described herein has been previously published:

- Guziewski, M., Coleman, S. P. & Weinberger, C. R. Atomistic investigation into the atomic structure and energetics of the ferrite-cementite interface: The Bagaryatskii orientation. Acta Materialia 119, 184-192 (2016).
- Guziewski, M., Coleman, S. P. & Weinberger, C. R. Atomistic investigation into the mechanical properties of the ferrite-cementite interface: The Bagaryatskii orientation. Acta Materialia 144, 656-665 (2018).
- Guziewski, M., Coleman, S. P. & Weinberger, C. R. Interface energetics and structure of the pearlitic microstructure in steels: An atomistic and continuum investigation. Acta Materialia 155, 1-11 (2018).

TABLE OF CONTENTS

LIST OF TABLES

LIST OF FIGURES

Chapter 1

Introduction

Steel is one of the most prevalent materials found in modern society, with over 1.6 billion metric tons produced in 2017. In addition to its high strength and low cost [1], the common usage of steel can be also be attributed to the wide range of physical properties that it exhibits, allowing its use in a range of applications. With different processing routes and alloy content the microstructure and properties of steel can be dramatically altered, affecting mechanical properties such as strength, ductility, and toughness [2]. Carbon steels for example, which may be the most prevalent by volume, have wildly different properties as the carbon content is changed, with low carbon steels (wrought iron) being easily workable while ultra-high carbon steels (cast iron) are extremely hard and very brittle. Additionally, there are a wide range of microstructures that form within carbon steels, including pearlite, banite, and martensite, that alter the mechanical properties [3]. Even as alloying content is introduced into carbon steel, these microstructures are still found, making understanding them vital to understanding steel. However despite the enormous amount of research conducted on carbon-based steels, there are still a great number of outstanding questions regarding the microstructure of these steels and the associated mechanical properties. This includes pearlite, which is perhaps the most studied of these carbon steel microstructures. This work seeks to answer some of these questions with regards to the pearlitic microstructure through the use of both atomistics and continuum models, with the major thrust of this dissertation focused on answering the following:

1. Which of the commonly reported orientation relationships within pearlite is the most energetically favorable?
2. What occurs structurally at the interface between ferrite and cementite within each of these orientation relationships?

3. What effect does the orientation relationship, and the corresponding interface structure, have on the mechanical properties of the system?
4. How can this atomic scale information be applied to larger length scales?

Chapter 2

Background

2.1 The Iron-Carbon System

This work focuses on two forms of iron, ferrite (α-Fe) and austenite (γ-Fe), which are metals, and the interfaces they form with cementite (Fe_3C), a ceramic. These crystals are all known to have different structure, with ferrite being body centered cubic (BCC), austenite face centered cubic (FCC), and cementite orthorhombic with a unit cell containing 16 atoms (12 Fe, 4 C) [4] (Fig. 2.1). It is these phases within the iron-carbon system that in different combinations are among the main components in carbon steels. One of the most fundamental questions to these systems is what is the orientation relationship (OR), or relative alignment of the two crystals, between the layers of iron and cementite. As the OR of any laminate system will affect both energetics and mechanical response [5, 6], understanding how the OR influences the system is fundamental to understanding the microstructure. However, there is no consensus as to what is the most favorable OR within either the ferrite-cementite or austenite-cementite system. Therefore it is necessary to first look at the various proposed ORs within each system before any deeper analysis is undertaken.

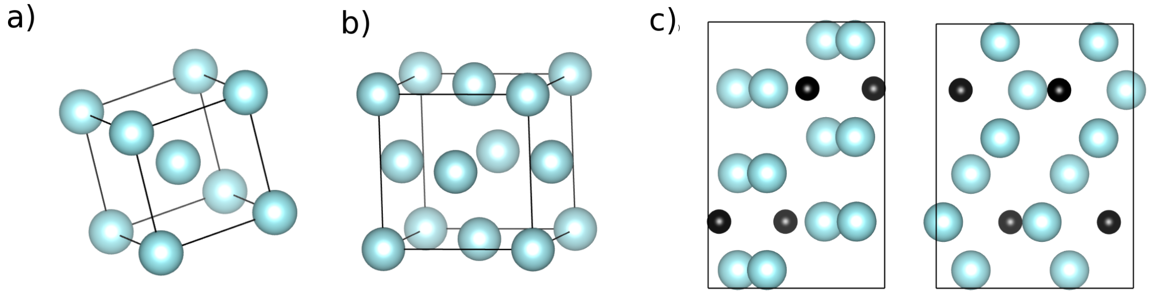

Figure 2.1: The iron and iron-carbides important to this work. a) Ferrite (BCC) b) Austenite (FCC) c) Cementite (Orthorhombic). Blue atoms represent iron and black represent carbon.

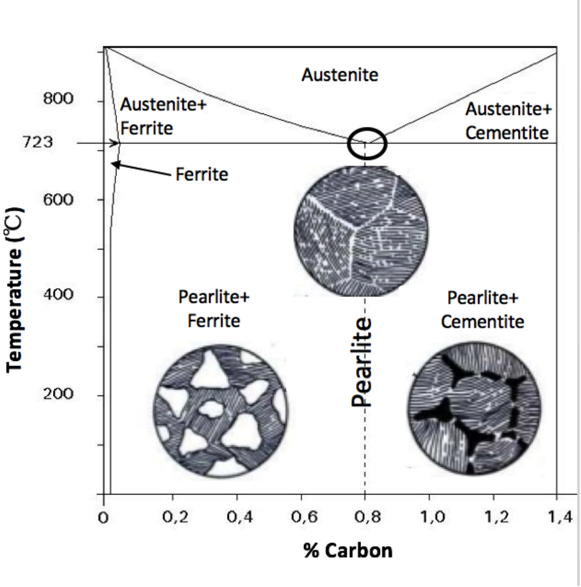

Figure 2.2: The Fe-C phase diagram. Reproduced from www.phase-trans.msm.cam.ac.uk.

2.1.1 Orientation Relationships

Ferrite-Cementite

Pearlite is derived from the eutectoid transformation of austenite (Fig. 2.2), and occurs at approximately 723 $^{\circ}C$ and 0.8$\%$ carbon content by weight. The transition from austenite to pearlite is a fairly complex one, involving both the diffusion of carbon to nucleate cementite, as well as the transformation of austenite into ferrite. The resultant ferrite and cementite regions arrange themselves in a lamellar structure, with contiguous regions of these alternating lamella known as pearlite colonies (Fig. 2.3). Within each colony, the lamella maintain the same orientation relationship [8], however this OR is not the same for all pearlite colonies. Several different ORs have been experimentally observed, with three in particular being reported the most often. Following the convention $a \leq b \leq c$ for the unit cell of cementite, these are:

the Bagaryatskii OR [9]:

$$[100]_\theta || [1\bar{1}0]_\alpha$$

$$[010]_\theta || [111]_\alpha$$

$$(001)_\theta || (11\bar{2})_\alpha$$

the Isaichev OR [10]:

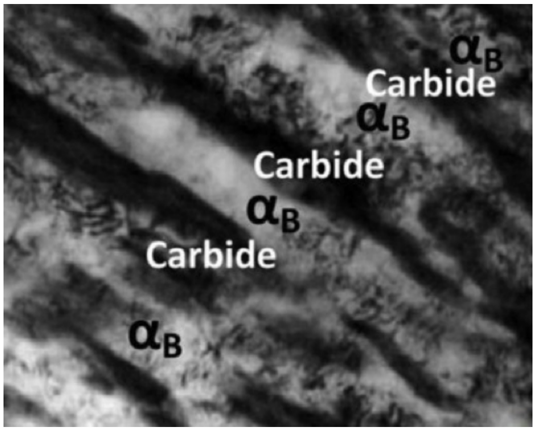

Figure 2.3: The iron-iron carbide microstructure. In pearlite, this consists of alternating layers of ferrite (α) and cementite (carbide). Reproduced from [7].

$$[010]_\theta || [111]_\alpha$$
$$[101]_\theta || [0\bar{1}1]_\alpha$$
$$(\bar{1}01)_\theta || (2\bar{1}\bar{1})_\alpha$$

and the Pitsch-Petch OR [11]:

$$[100]_\theta \text{ 2.6° from } [\bar{1}3\bar{1}]_\alpha$$
$$[010]_\theta \text{ 2.6° from } [\bar{1}13]_\alpha$$
$$(001)_\theta || (521)_\alpha$$

with θ denoting cementite and α for ferrite.

While the Bagaryatskii OR, the Isaichev OR, and the Pitsch-Petch OR are all commonly reported, there is no consensus as to which of the three ORs is the most favorable or prevalent in pearlite. The Isaichev OR was even thought to be an approximation of the Bagaryatskii OR, the two vary by only $3.8°$, until Zhou and Shiflet [12] proved it to be its own OR. Some research has shown the Bagaryatskii OR to be the most common [13], while others have suggested the Pitsch-Petch OR [14, 15]. Other work found the Pitsch-Petch and Bagaryatskii ORs [16] to occur with similar frequency, while a different study found the Pitsch-Petch and Isachev ORs [17] to be the most prevalent and occur with approximately the same frequency. Early work used transmission electron microscopy (TEM) to determine the ORs of pearlite, while more recent work has used electron backscatter diffraction (EBSD) to determine the ORs [11, 18]. The use of EBSD has validated many of the ORs found through TEM investigations, including the three mentioned above, but has done little to clarify which is the most favorable. It has been suggested that which OR forms is determined by the manner in which it nucleates, as the Pitsch-Petch has been found to nucleate from pure austenite [19], while the Bagaryatskii appears to form when nucleating from pre-eucteoid ferrite [20] or cementite [21]. The Isaichev OR has been observed much more seldomly, and often times in alloyed steels, raising the possibility that it is this alloying content that contributes to its formation. There have also been proposals that factors as wide ranging as heat treatment [11] and the applied magnetic field [22] determine the OR that forms. Regardless of the manner in which they nucleate, there are clear structural reasons for the favorability of these ORs, as all three are seen to have relatively good atomic coherency between the ferrite and cementite at the interface plane (Fig. 2.4). It has also been suggested by Zhang el al. [23] that the Bagaryatskii and Pitsch-Petch ORs are actually incorrect, with the true ORs varying by a small angle rotation of the habit plane. These "near" ORs are defined as follows:

Near Pitsch-Petch

$$[010]_\theta || [\bar{1}31]_\alpha$$

$$(103)_\theta || (110)_\alpha$$

Near Bagaryatskii

$$[010]_\theta || [111]_\alpha$$

$$(103)_\theta || (110)_\alpha$$

As error in TEM can rise to as high as 5% [10], this is indeed possible, and convergent beam Kikuchi line diffraction patterns (CBKLDP) found only the near Bagaryatskii, near Pitsch-Petch OR, and Isaichev ORs. It is notable that all three of these ORs share a $(103)_\theta || (110)_\alpha$ symmetry, which are close packed planes in within their respective crystal structures. The favorability of near ORs over their parents works under the assumption that the alignment of these planes (Fig. 2.5) will enhance atomic registry through the interface, and are therefore energetically favorable. The favorability of the $(103)_\theta||(110)_\alpha$ symmetry is further supported by Zhong et al. [24], who using edge to edge matching principles found the alignment of these planes to be among the most favorable in the ferrite-cementite system. However, while there appears to be a very compelling argument for the non-existence of the Bagaryatskii and Pitsch-Petch ORs in pearlite, both are widely accepted to be present in ferrite-cementite interfaces of both banite [15] and tempered martensite [25]. Additionally, while aligning the $(103)_\theta$ and $(110)_\alpha$ planes will certainly help the ferrite better act as a continuation of the cementite structure, it can also slightly decrease the atomic coherency of the interface. These would have contradictory effects energetically, with former decreasing the energy of the interface and the latter increasing it. As the exact magnitude of these effects are unknown, it is still not clear if the near ORs are in fact more favorable than their parent ORs. As such, all five of these potential ORs warrant further investigation.

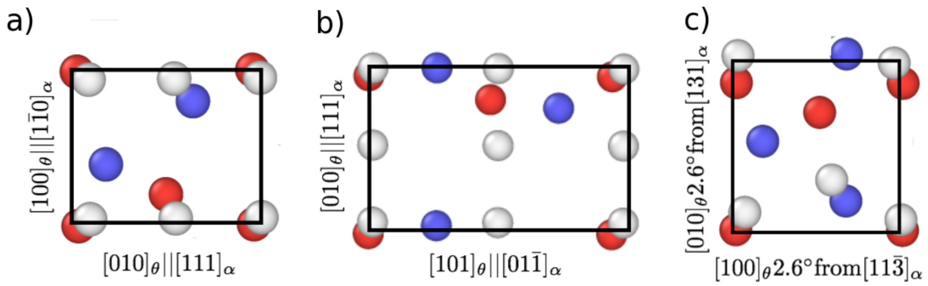

Figure 2.4: Interface coherency of the a) Bagaryatskii, b) Isaichev and c) Pitsch-Petch ORs in pearlite. All ORs are found to have good alignment between the two lattices. The interfaces shown consist of ferrite iron (white) and cementite carbon (blue) and iron (red).

Austenite-Cementite

Since pro-eutectoid cementite nucleates out of austenite at higher temperatures (Fig. 2.2), forming at the boundary between grains, the ORs for austenite and cementite have also been studied. The most commonly reported is the Pitsch OR [19,26]. Similar to the near ORs in pearlite however, there are questions as to whether the original formulation is correct. Much of the dispute centers on the definition of orientation of the interface plane, also known as the habit plane, within the

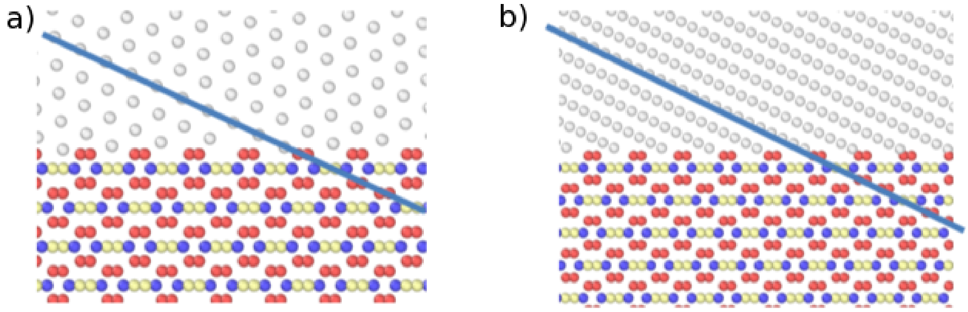

Figure 2.5: Alignment of the $(103)_\theta$ and $(110)_\alpha$ in the a) Near Bagaryatskii and b) Near Pitsch-Petch ORs. The interfaces shown consist of ferrite iron (white) and cementite carbon (blue) and iron (red and yellow).

OR, a microscopic degree of freedom (DOF) which is oftentimes difficult to determine using TEM and EBSD. The determination of the habit plane is further complicated by the stepped structure of the austenite-cementite interface (Fig. 2.6) which raises questions as to whether the reported habit planes are the true habit planes or simply the net plane formed by these various steps. As a result of these ambiguities, there are three proposed habit planes for the Pitsch OR, :

Pitsch 1 [19, 27]:

$$[010]_\theta || [10\bar{1}]_\gamma$$
$$(\bar{1}03)_\theta || (\bar{1}1\bar{1})_\gamma$$

Pitsch 2 [28]:

$$[010]_\theta || [10\bar{1}]_\gamma$$
$$[\bar{1}01]_\theta || [323]_\gamma$$
$$(101)_\theta || (1\bar{3}1)_\gamma$$

Pitsch 3 [29, 30]:

$$[010]_\theta || [10\bar{1}]_\gamma$$
$$(405)_\theta || (1\bar{4}1)_\gamma$$

with γ denoting austenite.

The differences between the various formulation of the Pitsch OR are similar to those between the parent and near ORs within pearlite, and thus raises the similar question of is it energetically favorable to slightly reduce interface coherency in order to align a high symmetry directions (Pitsch 1), or is the coherency the overriding factor. The idea of aligning high symmetry directions is taken further by the Pitsch 3, which arrises from work by Zhang et al. [29] in which the habit plane is determined by minimizing the distance between high symmetry directions in reciprocal space. In addition to the Pitsch OR, the Thompson-Howell (T-H) OR has also been observed at austenite-cementite interfaces. There are the same difficulties in determining the proper habit plane within this OR, and as such, there are also several formulations of the Thompson-Howell OR:

T-H 1 [27]:

$$[010]_\theta||[10\bar{1}]_\gamma$$

$$(103)_\theta||(\bar{1}1\bar{1})_\gamma$$

T-H 2 [28]:

$$[010]_\theta||[110]_\gamma$$

$$[\bar{1}01]_\theta||[323]_\gamma$$

$$(10\bar{1})_\theta||(1\bar{3}1)_\gamma$$

T-H 3 [29,30]:

$$[010]_\theta||[110]_\gamma$$

$$(30\bar{4})_\theta||(1\bar{4}1)_\gamma$$

It can be observed that the formulations of the Thompson-Howell are vary similar to those of the Pitsch. Additionally, as the $(101)_\theta$ and $(10\bar{1})_\theta$ are mirrors of each other, the resultant atomic coherency of the interface is the same as the Pitsch OR (Fig. 2.7). As a result, the only difference between the two ORs is the alignment of secondary symmetries, the $[100]_\theta||[[5\bar{5}4]_\gamma$ and $[001]_\theta||[\bar{2}25]_\gamma$ for the Pitsch and the $[100]_\theta||[[181]_\gamma$ and $[001]_\theta||[\bar{4}1\bar{4}]_\gamma$ for the Thompson-Howell. This has led several researchers to suggest that the Thompson-Howell is simply a variant of the Pitsch OR [10,31], created through the formation of a $(101)_\gamma$ twin in the austenite. However, while it appears this twinning operation does allow for the relation of the two ORs, it does not define what the habit planes would be and as such, the difference between the Pitsch and Thompson-Howell ORs is still an open question.

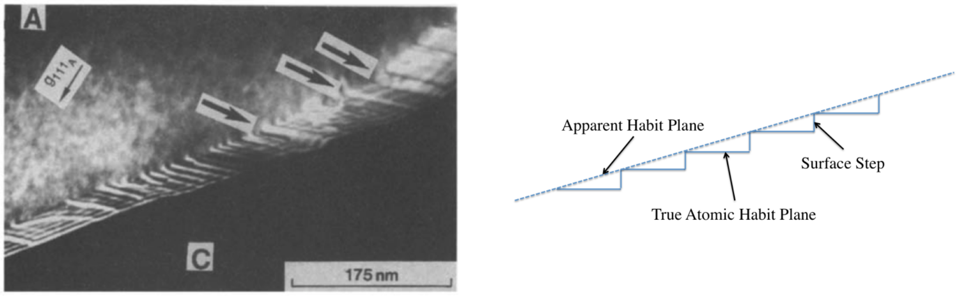

Figure 2.6: TEM image produced by Spanos and Aaronson [28] showing the presence of surface steps at the austenite-cementite interface. These steps create ambiguity in defining the true habit plane between the two crystals. Reproduced from [28]

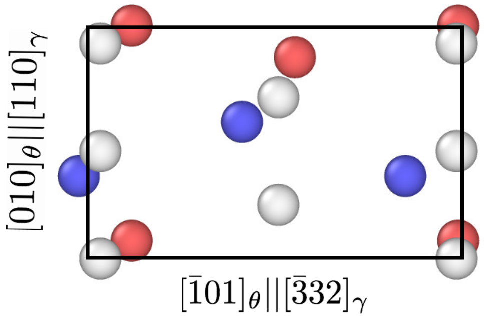

Figure 2.7: Interface coherency of the Pitsch and Thompson-Howell ORs for the $(101)_\theta||(1\bar{1}3)_\gamma$ habit plane. The interfaces shown consist of austenite iron (white) and cementite carbon (blue) and iron (red).

2.2 Interface Thermodynamics

Classical nucleation and growth theory states that the interfacial energy between two crystals is an important factor in determining orientation between materials. This interfacial energy, which will vary with changes in orientation relationship and habit plane, is similar to the concept of the free surface energy of a crystal. However, whereas free surface energy is generally with regards to a vaccuum, interfacial energy is with regards to a second crystal or phase. The introduction of this non-coherent interface increases the energy of the system, and smaller this increase, the easier it is for the particular interface is to form. In order to define the interfacial energy of a system, thermodynamics is used, with the first consideration being the Gibbs free energy (G) of the system. This is given by

$$G = U + PV - TS \tag{2.1}$$

where P is pressure, V is volume, T is temperature, S is entropy, and U is the internal energy of the system. If we consider a bicrystal which is growing by accretion from a reservoir of C different component atoms, the change in energy of this system can be determined by combining the first and second laws of thermodynamics, and is given by:

$$dU = TdS - PdV + \sum_{i=1}^{C} \mu_i dN_i + \gamma dA \tag{2.2}$$

where μ is the chemical potential, N the number of atoms, A is the area of the interface, and γ is the interfacial energy. By integrating Equation 2.2 and combining it with Equation 2.1, the interfacial energy of the system can then be shown to be:

$$\gamma = \frac{1}{A}[G - \sum_{i=1}^{C} \mu_i N_i] \tag{2.3}$$

This then allows for the calculation of interfacial energy through consideration of the total energy of the system along with the chemical potentials of the various atom types and the associated number of atom of each type.

2.3 Atomistic Modeling

Atomistic modeling has been used extensively to investigate the structure, energetics and mobility of metal interfaces. Grain boundaries have been studied in face-centered cubic (FCC) metals including their structure [32, 33], energetics [34–36], mobility and migration [37–40], mechanical response [41–44], and damage tolerance [45]. Similar work is ongoing in body-centered-cubic

(BCC) metals [46–51]. There has also been substantial work on modeling BCC-FCC interfaces, including radiation damage tolerance [52], interfacial structure [53–55], and mechanical properties [56, 57] and phase transformations [58]. There have been fewer atomic level studies of interfaces of ceramics or metal-ceramic interfaces. However, work has been conducted on grain boundaries in oxides such as alumina [59,60], ZnO [61], MgO [62] as well as silicon [63], diamond [64], and silicon carbide [65]. Atomistics has also been used to study the mechanical response of systems at the nanoscale. Much of this work was done on nanowires [66–68] and nanotubes [69, 70]. These simulations have been found to be fairly accurate, and include the successful prediction of the strength of gold nanowires prior to experimental measurements [71]. While this is not an exhaustive list, it does point to the utility of using atomistic simulation methods to gain insight into the energetics, structure, and mechanical behavior of interfaces.

2.3.1 Interatomic Potentials

Atomistic simulations however, are only as effective as the interatomic potentials they use and ceramics are notoriously difficult to model. It therefore becomes necessary to consider multiple interatomic potentials, and while there many different formulations, three different types were considered during the scope of this work: Embedded Atom Method (EAM), Modified Embedded Atom Method (MEAM), and Tersoff.

EAM

This formulation approximates the energy of each atom as the sum of a pair wise interaction and an embedding term representing the energy cost of placing the atom in the electron cloud. It is given by the expression:

$$E_i = F_\alpha\big(\sum_{i\neq j}\rho_\beta(r_{ij})\big) + \frac{1}{2}\sum_{i\neq j}\phi_{\alpha\beta}(r_{ij})$$

where r_{ij} is the distance between atoms i and j, $\phi_{\alpha\beta}$ is the pair potential between atom i of type α and atom j of type β, ρ_β is the charge contributed at distance r_{ij} by an atom of type β, and F_α the embedding function for an atom of type α in the electron cloud. The pair potential, charge density function, and embedding function are fit to the material properties of the system.

MEAM

Similar in form to the EAM, this method's charge density function takes into account the presence of multiple atoms in the local neighborhood with an angular dependent screening function and then is normalized by the number of atoms in the local neighborhood (Z_i):

$$E_i = F_\alpha\left(\sum_{i\neq j}\frac{\bar{\rho}_\beta(r_{ij})}{Z_i}\right) + \frac{1}{2}\sum_{i\neq j}\phi_{\alpha\beta}(r_{ij})$$

The pair potential, charge density function, and embedding function are again fit to the material properties of the system however due to the angular dependent screening function, this type of potential can model angular dependent bonds, such as covalent, better than the EAM. It is significantly more expensive computationally however, as the charge density function for each atom must account for the combined contribution of multiple atoms in the local neighborhood, as opposed to the 2-body functional form that it takes for the EAM potential.

Tersoff

The Tersoff potential is similar to a pair potential in that there is an attractive term, representing the bond energy, and a repulsive term to the energy of each atom. The strength of the bond is modified by the b_{ijk}, which is a 3-body function.

$$E_i = \sum_{j\neq i}\big(\phi_{\alpha\beta}(r_{ij}) + \sum_{k\neq i,j} b_{ijk}\phi_{\alpha\beta,bond}(r_{ij})\big)$$

where $\phi_{\alpha\beta,bond}$ is the bond energy function for atoms of type α and β. Again, these values are fit to material properties to create the appropriate potential. Due to the 3-body b_{ijk} term this type of potential is also able to account for directionality. Computationally it is less expensive than the MEAM but more expensive than the EAM.

2.3.2 Interfacial Energy

When considering interfacial energy within atomistic simulations, the most common approach, referred to as the “slab" approach in this work, starts with the creation of two cuboidal region. Using Equation 2.3, and considering a system at constant temperature and pressure, it becomes possible to simply the expression for interfacial energy to several values easily determined using atomistics. This includes the bulk energies of the two regions (E_1, E_2) and their free surface energies (γ_1, γ_2). These values, along with the total energy of the system (E_{tot}) and the interface size (L_x, L_y), allow for the calculation of interfacial energy using the following equation:

$$E_{\text{int}} = \frac{E_{\text{tot}} - E_1 - E_2 - E_\epsilon}{L_x L_y} - \gamma_1 - \gamma_2 \tag{2.4}$$

The strain energy, E_ϵ, is a result of two non-coherent lattices being strained to created a periodic interface, and can be approximated by:

$$E_\epsilon = E_{\epsilon,1} + E_{\epsilon,2} = \sum_{j=1}^{2} \sum_{i=1}^{2} \frac{1}{2}(V_1 C_{ij,1} \epsilon_{i,1}^2 + V_2 C_{ij,2} \epsilon_{i,2}^2) \tag{2.5}$$

where V is the volume of each region and C_{ij} and ϵ_i represent the elastic constants and strain, respectively, in the interface plane directions. If the simulation is made sufficiently large in order to minimize ϵ however, this term becomes negligible.

The slab approach essentially treats the system as two independent crystals placed adjacent to each other, and all atoms are assigned to the crystal in which they were originally created, regardless of any changes that may occur during the simulation. However, in systems in which both component crystals have common elements, such as those discussed in this work, this raises the potential for ambiguity near the interface plane as to which crystal the element should be associated with. This ambiguity is not unique to iron-iron carbide systems, as it has been discussed in other multiphase interfaces [72] as well. Therefore it is necessary to consider alternate methods for calculating interfacial energy, methods which will be discussed later in this work.

2.3.3 Atomic Stress

In addition to energetics, atomistics can also be used to understand the mechanical response of systems. The bulk stress state in all simulations performed in this work is determined using the standard virial formulation, in which the stress tensor is defined as the functional derivative of the free energy of the system with respect to the deformation tensor. This formulation has been shown to converge to the Cauchy stress [73] for sufficiently large volumes. It is additionally possible to to determine the stress state of regions of the system by summing the per-atom virial [74] of the atoms within and dividing by the volume they occupy. The virial of a constituent region is given by:

$$S_{ij} = \sum_{n=1}^{N_p} [m^{(n)}(v_i^{(n)} - \bar{v}_i)(v_j^{(n)} - \bar{v}_j) + \frac{1}{2}\sum_{p=1}^{N} r_i^{(np)} F_j^{(np)}] \tag{2.6}$$

where V is the volume of the region, n is an atom in the region being considered, p is any atom in the simulation, v is atomic velocity, $\bar{v}$ is the mean velocity of the deforming box, $r^{(np)}$ is the displacement vector between atoms n and p and $F^{(np)}$ is the force between the two.

In order to determine the stress of a region, its volume must therefore be known. While this is a simple endeavor when considering a whole simulation box, it becomes more complicated when attempting to determine the volume of atoms in a system that is changing both shape and size. In order to address this issue, Voronoi tessellation [75] is used. In this method, the volume of each atom is determined by creating linear partitions equidistant between the atom and all its neighbors, creating a volume in which the atom is the centroid. Using this approach, atomic volume can be approximated at every timestep and when combined with Eq. 2.6 yields an expression for stress of a group of atoms:

$$\sigma_{ij} = -\frac{\sum^{N} S_{ij}}{\sum^{N} V_{vor}} \tag{2.7}$$

where N is number of atoms in the region and V_{vor} the as calculated Voronoi volumes of each atom. This ability to evaluate the stress state of specific regions within a simulation is very powerful when applied to the lamellar structures being investigated here, as it allows for a deeper understanding of what is occurring within each of the constituent phases.

2.4 O-Lattice Theory

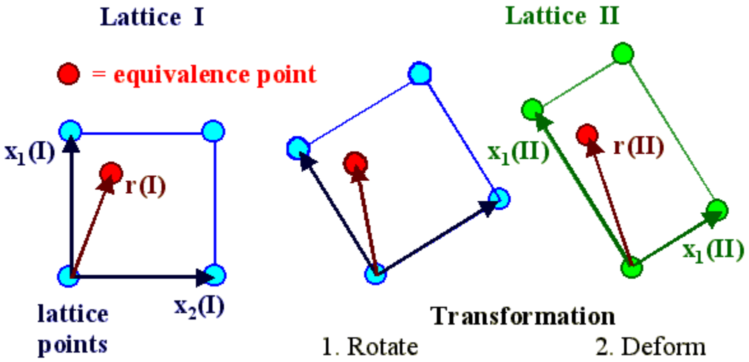

Figure 2.8: Example of a transformation in O-lattice theory. One crystal can be transformed into the other or both can be transformed into an intermediate configuration. Reproduced from www.tf.uni-kiel.de.

A common feature to lamellar systems with semi-coherent lattices, such as those being studied here, is the presence of interfacial dislocations [76–78]. These types of interfacial dislocations have previously been suggested for pearlite [79, 80], and later in this work will be shown to be present for both the ferrite-cementite and austenite-cementite interfaces. It is therefore useful to find tools that can describe qualities of these dislocations such as spacing, line direction, and Burgers vectors, and resultantly help to validate atomistic results. One such method is O-Lattice theory [81], a variant of the classic Frank-Bilby equation [82] for characterizing dislocations. In this continuum method, the two semi-coherent lattices that form the interface are strained to create a coherent, intermediate reference interface (Fig. 2.8) . Given the dislocation line directions and spacing, it becomes possible to determine Burgers vectors (**b**) for the given intermediate lattice using the Frank-Bilby equation:

$$B = \sum_{i=1}^{2} (\frac{\mathbf{n} \times \boldsymbol{\xi}_i}{d_i} \cdot \mathbf{p})\mathbf{b}_i = (F_A^{-1} - F_B^{-1})\mathbf{p} \tag{2.8}$$

where **n** is the unit vector normal to the interface, $\boldsymbol{\xi}$ is the line direction, d_i is the dislocation spacing, F_A^{-1} and F_B^{-1} are the transformation matrices from the natural states of the two crystals to the intermediate reference lattice, and **p** is an arbitrary probe vector. O-lattice theory further states that the dislocation line directions will be in the same directions as the O-points, or points of high coherency between the two lattices. Figure 2.9 shows an example of the O-points in the Bagaryatskii OR of pearlite created by overlaying the two component lattices. If the O-points are known, it then becomes possible to predict the Burgers vector without knowing the the line direction and spacing, as the Burgers vectors can be given by:

$$\mathbf{b}_i = (F_A^{-1} - F_B^{-1})\mathbf{p}_i^o \tag{2.9}$$

where $\mathbf{p}_i^o$ are the O-points. This creates a very robust methodology for characterizing these systems independent of atomistics, as the O-points and transformation matrices are both functions of the lattice structure of the crystals. Additionally, this aids in overcoming a shortcoming in atomistics, as it is often difficult to determine the Burgers vector from simulations results. This arrises from the fact that there is not a clear way to construct a Burgers circuit (Fig. 2.10) across a non-coherent interface. However, while O-lattice theory is extremely useful in determining the character of the dislocations, it is incapable of determining the exact magnitude of the Burgers vectors. Different reference lattices will result in dislocations sharing the same character but with differing magnitudes. It is therefore necessary to use expansions of this formulation, which will be discussed in detail in Section 3.3.

2.5 Interface Compatibility

For metal-ceramic systems such as those under investigation here, it is important to consider interface compatibility as well. This is the constraint that the two lamella must remain ideally

Figure 2.9: Example of O-points (highlighted by yellow circles) in the Bagaryatskii OR. These points were visualized by overlaying the appropriately oriented lattices of ferrite and cementite.

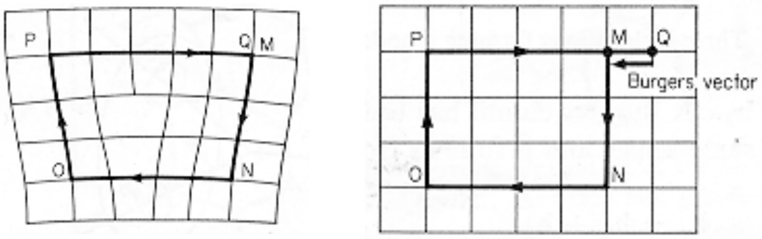

Figure 2.10: Burgers circuit method for determining the Burgers vector. In incoherent interfaces this is not possible as the atomic arrangement is different on each side of the interface. Reproduced from www.onlinemetallurgy.com.

bonded, and thus have identical interface dimensions . During the elastic response of the system, this is of limited importance, as the rate at which both the cementite and ferrite contract or expand, is relatively similar. Once the ductile ferrite yields however, the cementite acts as a constraint, thus increasing the stress state of the system. During longitudinal loading, the lamella are in an iso-stress state, and thus:

$$\sigma_{zz} = \sigma_{zz}^{\theta} + \sigma_{zz}^{\alpha} \tag{2.10}$$

where z is the direction of loading. The strain in this direction in each layer is not the same, and is the volume fraction of the total applied strain, while the strain in the transverse is constant for both lamella

$$\begin{gathered}
\epsilon_{zz} = \frac{V_\theta}{V}\epsilon_{zz}^{\theta} + \frac{V_\alpha}{V}\epsilon_{zz}^{\alpha} \\
\epsilon_{xx} = \epsilon_{xx}^{\theta} = \epsilon_{xx}^{\alpha} \\
\epsilon_{yy} = \epsilon_{yy}^{\theta} = \epsilon_{yy}^{\alpha}
\end{gathered} \tag{2.11}$$

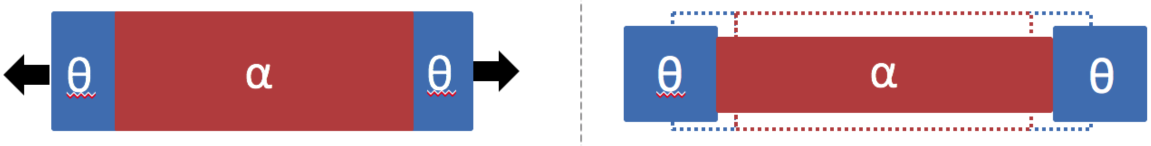

Figure 2.11: Visualization of interface compatibility in longitudinal loading. The brittle cementite acts as a constraint to the expansion or contraction of the ductile ferrite, thus increasing the stress state of the system.

The total stress in the transverse directions should be 0, and a volume fraction of the stresses in the ferrite and cementite:

$$\begin{aligned} \sigma_{xx} = 0 = \frac{V_\theta}{V}\sigma^\theta_{xx} + \frac{V_\alpha}{V}\sigma^\alpha_{xx} = \frac{V_\theta}{V}E^\theta_{xx}\epsilon^\theta_{xx} + \frac{V_\alpha}{V}E^\alpha_{xx}\epsilon^\alpha_{xx} \\ \sigma_{yy} = 0 = \frac{V_\theta}{V}\sigma^\theta_{yy} + \frac{V_\alpha}{V}\sigma^\alpha_{yy} = \frac{V_\theta}{V}E^\theta_{yy}\epsilon^\theta_{yy} + \frac{V_\alpha}{V}E^\alpha_{yy}\epsilon^\alpha_{yy} \end{aligned} \tag{2.12}$$

If it is assumed that the strain in the transverse direction of each lamella is related to the applied strain in the longitudinal direction by some constant r, it then becomes possible to relate the stress in the transverse directions with the applied strain.

$$\begin{aligned} 0 = \frac{V_\theta}{V}E^\theta_{xx}r_{\theta,x}\epsilon^\theta_{zz} + \frac{V_\alpha}{V}E^\alpha_{xx}r_{\alpha,x}\epsilon^\alpha_{zz} \\ 0 = \frac{V_\theta}{V}E^\theta_{yy}r_{\theta,y}\epsilon^\theta_{zz} + \frac{V_\alpha}{V}E^\alpha_{yy}r_{\alpha,y}\epsilon^\alpha_{zz} \end{aligned} \tag{2.13}$$

This suggests that the actual strain load carried by each layer is not just the volume ratio, but instead affected by a wide array of factors in the transverse directions:

$$\begin{aligned} \frac{\epsilon^\alpha_{zz}}{\epsilon^\theta_{zz}} = -\frac{V_\theta}{V_\alpha}\frac{E^\theta_{xx}}{E^\alpha_{xx}}\frac{r_{\theta,x}}{r_{\alpha,x}} \\ \frac{\epsilon^\alpha_{zz}}{\epsilon^\theta_{zz}} = -\frac{V_\theta}{V_\alpha}\frac{E^\theta_{yy}}{E^\alpha_{yy}}\frac{r_{\theta,y}}{r_{\alpha,y}} \end{aligned} \tag{2.14}$$

This change in the strain load of the lamella can be expressed as a constraint stress and is of the form $\frac{V_\theta}{V_\alpha}K$, where K is a material constant. This stress will change with volume ratio, and therefore has implications for events such as yield stress, flow stress, and ductility. It is worth noting that his phenomenon is sometimes mistaken in composites as an inverse Hall-Petch effect, as if care is not taken to keep the volume ratio constant, smaller sizes will change the ratio, and thus the constraint stress. There are no size effects in the formulation presented however, and as will be shown later in this work, during longitudinal loading, yield stress, flow stress, and ductility do in fact change with volume ratio but not size.

Chapter 3

Literature Review

3.1 Pearlite Formation

The theoretical modeling of the formation of pearlite has always proven difficult due to the many competing mechanisms of the process, including the transformation of austenite into ferrite, the diffusion of carbon, and the nucleation and growth of cementite colonies. The earliest work on this topic by Zener [83] sought to explain the phenomenon through simply the carbon diffusion mechanism (Fig. 3.1). This worked under the assumption that the movement of iron atom between the austenitic and ferritic phases was relatively small when compared to the movement of carbon between interstitial positions, and as such it would be this carbon diffusion that acted as a limiting factor on the transformation. However, the transformation rates of austenite to pearlite predicted by this model differed from experimentally observed values by an order of magnitude. Despite this discrepancy, carbon diffusion is clearly an important part of the transformation, as the processes generally used to define the transformation from an FCC lattice to a BCC lattice, such as the Bain transformation path [84], require the movement of carbon due to the low solubility of carbon in ferrite. Therefore the process has been attempted to be described thermodynamically as follows: graphite precipitates out of the autenite, the austeinte transforms into ferrite, graphite combines with ferrite in the proper proportions to form cementite [85]. While this is certainly a simplification, and thermodynamically incorrect as cementite is metastable, the theoretical enthalpies of this process compare well with experimentally observed values [86]. A similar process can also be used to explain the formation of the austenite-cementite system, except in this case not all the carbon precipitates from the austenite, only enough transform an appropriate amount ferrite for formation of cementite. The specifics of these processes are complicated however, by effects of temperature and composition [87].

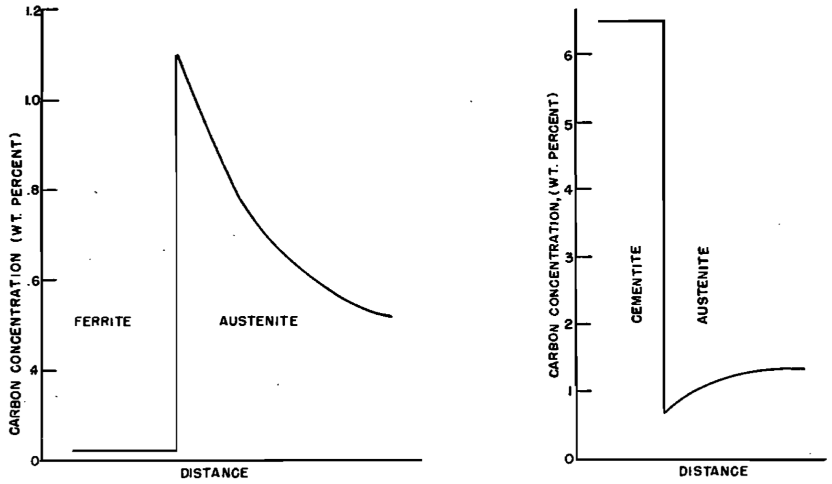

Figure 3.1: Carbon concentration across interface between austenite and ferrite and austenite and cementite as proposed by Zener [83]. Reproduced from [83].

These models also fail to account for the effect that the formation of interfaces between the ferrite, austenite, and cementite will have on the system, such as the introduction of lattice mismatch and interfacial energy. More recent work on this subject has attempted to account for these factors showing for instance, that this lattice strain can affect the rate of carbon diffusion [88, 89], bringing predicted nucleation rates closer to those observed experimentally. It has also been suggested by Zhang et al. [90], that a metastable intermediate structure (MIS) may be formed that acts as a transition layer between the austenite and the nucleating pearlite (Fig. 3.2). This would reduce the energetics of the system by removing the interface between the pearlite and the austenite. This does not account however, for the the interfacial energy between the cementite and ferrite within the pearlite which will also influence the nucleation rate, as well as the resultant microstructure.

3.2 Interfacial Energy

There have been attempts, both experimentally and computationally, to determine the interfacial energy of the ferrite-cementite interface. A survey of these values can be found in Table 3.1. While each is a valid approximation and provide an approximate range of expected values, there are ambiguities or flaws in the various approaches that warrant the further investigation of this topic that is undertaken in this work.

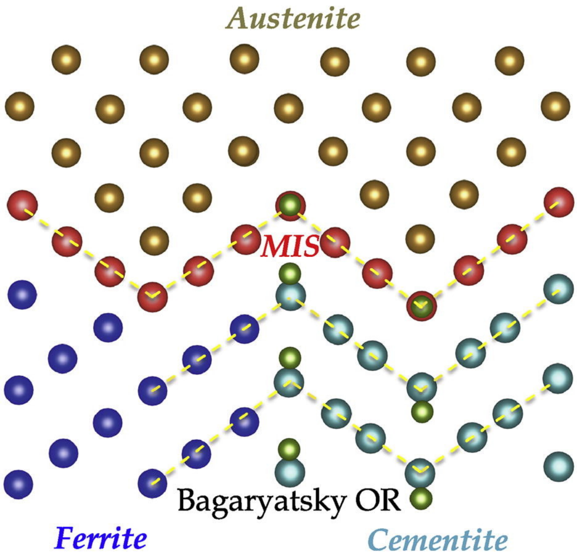

Figure 3.2: Potential metastable intermediate structure proposed by Zhang et al. [90] for the Bagaryatskii OR. This structure would act as a transition layer between the austenite and the nucleating pearlite, reducing interfacial energy for the system. Reproduced from [90].

Table 3.1: Survey of reported interfacial energy values between cementite and ferrite. Reproduced form [91].

Method	Coarsening rate and data fitting	Interfacial enthalpy measurement	Atomistic Simulations	Density Functional Theory	Dihedral Angle
Interfacial Energy (J/m^2)	0.56 [92] 0.248-0.417 [93]	0.7±0.3 [94] 0.5±0.36 [95]	0.615 [96] 0.50-0.66 [97]	0.45 [90] 0.45 [98]	0.52±0.13 [99]

3.2.1 Experimental Results

The experimental calculation of interfacial energy is a complicated endeavor in even the simplest of system, let alone one containing two different elements in three different phases. There have been several values reported experimentally for the interfacial energy of pearlite however. Early attempts sought to use calorimetry on the transformation from austenite to pearlite. Constant heat-flow calorimeters were used to measure the change in enthalpy during the transformation of pure austenite into pearlite. As the energy of formation for all components is known, the difference between measured and theoretical values must be the interfacial free energy. There are several potential sources of error in this formulation however. As pearlite is a line compound, if there an excess or deficiency of carbon the pearlite will form within a ferrite or cementite matrix, thus introducing another interface that will affect the energetics. Additionally there is the issue of free surface energies, which are different for austenite and pearlite. Another method to determine the interfacial energy is to use growth kinetics to infer the energetics from the coarsening rate of pearlite grains. The rate constant for diffusion controlled coarsening (K^*) is given by the expression:

$$K^* = \frac{8\gamma D_{eff} C_e V_m^2}{9RT} \tag{3.1}$$

where γ is the interfacial energy, D_{eff} the effective diffusion coefficient, C_e the concentration of solute atoms, V_m the molar volume of cementite, and T is temperature. By considering volume and composition constraints, this can be related to ferrite and carbon values for diffusion (D), concentration (C), and molar volume (V) using:

$$D_{eff} = \frac{C_{Fe} V_{Fe}^2}{C_C V_C^2} D_{Fe} \tag{3.2}$$

Combining these equations and assuming that C_e and C_C are roughly equivalent gives:

$$K^* T = \frac{8\gamma C_{Fe} V_{Fe}^2 V_m^2 D_0}{9RV_C^2} \exp\left(-Q/RT\right) \tag{3.3}$$

where $D_{Fe} = D_0 \exp\left(-Q/RT\right)$. As γ and K^* are the only temperature dependent quantities in the expression, it then becomes possible to determine interfacial energy through the consideration of coarsening rates at various temperatures. This approach has its limitations however, as this expression is only valid for systems in which the volume fraction of secondary particles is near zero, and as such if used on alloyed steels can yield incorrect results. Additionally, the OR of the pearlite colonies in these studies is unknown. These results nonetheless do give an idea as to what order these results should be, as energies have generally been found to be in the range of 0.25-0.5 J/m^2 [92, 93].

3.2.2 Computational Results

There have been several previous attempts to model the ferrite-cementite using computational methods. One of the earliest was by Ruda et al. [96] in their development of an EAM potential for the iron-carbon system. Their work found the interfacial energy of the Bagaryatskii OR to be 0.615 J/m^2. However, EAM potentials do not take into account the directionality of bonds, something that is extremely relevant to the covalent bonds formed with the carbon in the cementite. As a result, while they can be useful for qualitative analysis, EAM potentials are not always the most accurate for energetic analysis. Additionally, the simulation box in this study was approximately 20 Å× 20 Å and consisted of 4442 atoms. Smaller simulation domains have larger elastic strains, and therefore generally higher interfacial energies. More importantly, the smaller simulation dimensions suppress the relaxation of the interface, and thus the correct interface structure is unlikely to be observed, especially if interfacial dislocations form. Similarly, for reasons of computational cost, Density Functional Theory (DFT) simulations generally consist of only a few unit cells and several hundred atoms. Such is the case for the work performed by Zhang et al. [90] and Zhou et al. [100]. These works studied the Bagaryatskii and Isaichev ORs, respectively, with both yielding interfacial energy values of 0.45 J/m^2. However, the identical values are likely an artifact of the different psuedopotential and integration techniques used more so than equivalent interfacial energies for the two ORs. Research conducted simultaneously to this work by Kim et al. [101] used a MEAM potential to study the ORs of pearlite. Table 3.2 shows the interfacial energy results of these simulations. Despite their simulation cell size being on the order of 20 nm $\times$ 20 nm, in several cases even this is too small to observe dislocation formation. One example is their simulations for the Isaichev OR, in which only one dislocation set was observed. If the dislocation spacing for lattice mismatch, $\frac{a_1 a_2}{a_1 - a_2}$, is used with the lattice constants from the MEAM potential, a dislocation spacing of approximately 80 nm is predicted, explaining why no dislocations were observed in one dimension of the simulation. This highlights the importance of constructing simulations with physical phenomena in mind.

Table 3.2: Ferrite-cementite interfacial energy values predicted by Kim et al. [101]

Orientation	Bagaryatskii	Isaichev	Pitsch-Petch	Near Bagaryatskii	Near Pitsch-Petch
Interfacial Energy (J/m^2)	0.628	0.500	0.660	0.536	0.555

In addition to simulation size, another important factor to consider is interfacial chemistry. While the ORs define the macroscopic degrees of freedom, it is also necessary to test the influence of the microscopic degrees of freedom. This consists of both in-plane translation and normal to plane translation relative to the interface, factors which will be discussed in depth later in this work. While in DFT simulations the in-plane translation is important to consider due to simulation size, it is less of a concern in atomistic simulations. The normal to plane translation is quite important though, as it can change the chemistry at the interface. Interfacial chemistry has been shown to play a substantial role in the interfacial energy of this system, initially in published work by the author [102, 103], but also in the DFT work done by Zhou [98], further validating its relevance. Table 3.3 shows the interfacial energies predicted by Zhou, and significant variation between the various chemistries can be observed. Ruda, Zhang and Kim all neglected to consider this factor, and in most cases it is ambiguous as to which chemistry is being considered, making it difficult to use the results in context to each other. It can also be observed that the computationally determined values lie near or above the upper limit of the experimentally reported values. This is somewhat surprising as all simulations were performed with perfect crystals and completely planar interfaces, and as such one would expect the predicted value to be lower than those found in experiments. This suggests that there may be some error within either or both classes of results.

Table 3.3: Interfacial energies of the possible terminating planes of the Isaichev OR predicted by Zhou et al. [100].

Model	1	2	3	4	5
Interfacial Energy (J/m^2)	0.449	1.125	1.651	0.687	1.765

3.3 Continuum Models

As previously noted, O-lattice theory is potentially a powerful tool in its ability to characterize Burgers vectors for an interface. However, it has one major weakness, the ambiguity as to what is the proper reference lattice. In recent years, there have been several approaches developed to deal with this potential problem, the most prominent being the Atomically Informed Frank-Bilby (AIFB) [104, 105], and a methodology incorporating anisotropic elastic theory by Vattré and Demkowicz [106].

The AIFB method attempts to determine the reference lattice, and associated Burgers vector magnitudes, by minimizing the difference between the first and second halves of Equation 2.8, representing the discrete and continuum formulations, respectively.

$$B = \sum_{i=1}^{2} (\frac{\mathbf{n} \times \boldsymbol{\xi}_i}{d_i} \cdot \mathbf{p})\mathbf{b}_i = (F_A^{-1} - F_B^{-1})\mathbf{p} \qquad \text{(2.8 revisited)}$$

Atomistic values for line direction and spacing are used for the discrete portion of the equation, and a list of translational vectors between atomic positions in each of the lattices is created to serve as potential Burgers vectors. The transformation from one of the crystal lattices to the other is determined and expressed as [101]:

$$F_{A \to B} = Q \cdot T \cdot M \tag{3.4}$$

where Q, T, and M are the rotation, shear, and dilation transformation matrices and are given by:

$$Q = \begin{bmatrix} \cos\theta & -\sin\theta \\ \sin\theta & \cos\theta \end{bmatrix} \qquad T = \begin{bmatrix} 1 & \gamma \\ 0 & 1 \end{bmatrix} \qquad M = \begin{bmatrix} m_x & 0 \\ 0 & m_z \end{bmatrix}$$

These matrices are then parameterized with values χ_θ, χ_γ, χ_x, and χ_z, and used to describe the transformation from lattice A ($\mathbf{x}_\mathrm{A}$) to an intermediate reference lattice $\mathbf{x}_\mathrm{R}$.

$$\mathbf{x}_R = F_A \mathbf{x}_A = F_B \mathbf{x}_B \tag{3.5}$$

where the rotation, shear and dilation matrices for F_A are given by:

$$Q_A = \begin{bmatrix} \cos \chi_\theta \theta & -\sin \chi_\theta \theta \\ \sin \chi_\theta \theta & \cos \chi_\theta \theta \end{bmatrix} \qquad T_A = \begin{bmatrix} 1 & \chi_\gamma \gamma \\ 0 & 1 \end{bmatrix} \qquad M_A = \begin{bmatrix} \chi_x m_x & 0 \\ 0 & \chi_z m_z \end{bmatrix}$$

The χ values are then varied from 0 to 1, with the list of potential Burgers vectors also undergoing the appropriate transformation, and a multivariable search applied to find the proper reference lattice and associated Burgers vectors by minimizing the difference between the two halves of the Frank-Bilby equation (Eq. 2.8). This approach is flawed though, as the discrete and continuum formulations of this equation should always be equal, regardless of the reference lattice chosen. It appears what is actually being minimized is the error in the atomistic simulations, likely in measuring line direction, spacing, or atomic positions. This is not to say that the Burgers vectors that are calculated are completely erroneous, their general character is correct. These AIFB results, however, are associated with uncertainty in the atomistic calculations and thus the determined reference lattice and Burgers vector magnitudes have no apparent physical meaning. An alternate approach to this method uses disregistry analysis, the variation from the unrelaxed and relaxed atomistic structures, and compares it to the determined reference lattice in order to find the Burger vectors. This suffers from the same issues as the reference lattice will still be associated with atomistic uncertainty. The AIFB approach is also limited by its reliance on atomistic values, as it is therefore limited to use on states of a system on which simulations have been performed.

The continuum method developed by Vattré and Demkowicz took an alternate approach and postulated that the proper reference state was that which results in a zero far-field strain state, essentially balancing the strain that was applied to form the reference state with that from the dislocations (Fig. 3.3). This approach has been seen to be valid for multiple systems [107–109], and has the additional benefit of accounting for the anisotropy in the two crystals. This approach has a rather complex mathematical formulation which will be summarized here, but a full description of the formulation can be found in [106]. It is worth noting that there are several typos within that text that have been corrected in the equations below.

The required inputs for this approach are simply the lattice structure of the two crystals, the associated O-points (Fig. 2.9), and the elastic constants of crystals. With the lattice structure and O-points known it possible to determine the Burgers vector for a given reference lattice (generally made to be one of the two lattices) using Equation 2.9.

$$\mathbf{b}_i = (F_A^{-1} - F_B^{-1})\mathbf{p}_i^o \tag{2.9 revisited}$$

Once the Burgers vector is known it is possible to determine theoretical line directions and spacings using the Frank-Bilby equation (Eq. 2.8). These values are invariant with reference lattice, and therefore can be compared to atomistic results to ensure the proper Burgers vector was chosen. As mentioned during the discussion on AIFB, there is often slight variations between the atomistic and theoretical values due to factors such as measurement errors and the enforced periodicity of simulation, but atomistics nonetheless serve as good check. For any given reference lattice, the far-field effects of the dislocations are then determined. This begins with by determining the set of eigenvalues, p, and eigenvectors, **a**, in each crystal for the equations det(Π) = 0 and Π **a** = **0**. Π is given by:

$$\begin{aligned} \Pi_1 &= C_{1(1)} + p_1(C_{2(1)} + C_{2(1)}^T) + p_1^2 C_{3(1)} \\ \Pi_2 &= C_{1(2)} + p_2(C_{2(2)} + C_{2(2)}^T) + p_2^2 C_{3(2)} \end{aligned} \tag{3.6}$$

where the C matrices are functions of the elastic constants, appropriately transformed to correspond to the system, and given by:

$C_{1(1)} = C_{i1j1}$ $C_{2(1)} = C_{i1j2}$ $C_{3(1)} = C_{3(2)} = C_{i2j2}$

$C_{1(2)} = C_{i1j1}\cos^2\phi + C_{i3j3}\sin^2\phi - \frac{1}{2}C_{i1j3}\sin 2\phi$ $C_{2(2)} = -C_{i1j2}\cos\phi + C_{i3j2}\sin\phi$

where ϕ is the angle between the dislocation lines. Each set of eigenvectors, $\mathbf{a}^\alpha$ is then used to determine the complex fitting parameters, $\bar{\lambda}$ and $\bar{\zeta}$, using the expression:

$$\sum_{\alpha=1}^{3} \bar{\lambda}_A^\alpha \mathbf{a}_A^\alpha - \bar{\zeta}_B^\alpha \mathbf{a}_{*B}^\alpha = -\mathbf{b} \tag{3.7}$$

where A and B represent the two crystals, **b** the Burgers vectors, and * signifies the complex conjugate. These fitting parameters can then be used to determine the far-field distortion of the dislocations (D^{∞}_{dis}) with the following:

$$\begin{aligned} G^{\alpha}_{(1)} &= \mathbf{a}^{\alpha}_{i(1)}(\delta_{j1} + p^{\alpha}_{1}\delta_{j2}) \\ G^{\alpha}_{(2)} &= \mathbf{a}^{\alpha}_{i(2)}(-\delta_{j1}\cos\phi + p^{\alpha}_{2}\delta_{j2} + \delta_{j3}\sin\phi) \end{aligned} \tag{3.8}$$

$$D^{\infty}_{\text{dis}} = \sum_{i=1}^{2} d_i^{-1} \sum_{\alpha=1}^{3} \left[\bar{\lambda}^{\alpha}_{i} G^{\alpha}_{i} + \bar{\zeta}^{\alpha}_{i} G^{\alpha}_{*i}\right] \tag{3.9}$$

where δ is the Kronecker delta and d is the dislocation spacing. The far-field strains of the the system can then be defined as the real, symmetric component of D^{∞}_{dis}. This dislocation strain can be calculated for both crystals, and the values summed with the strain on the lattice to transform it to the reference lattice. As was stated, the basis for this approach is that these strains should be zero in the far-field, and thus using multivariable minimization, all reference lattices between the two natural lattices are scanned and the zero value found. As the dislocations in the systems considered in this work are found to occur only within the interface plane, it is only necessary to consider the ϵ_{xx}, ϵ_{zz}, and ϵ_{xz} strains in this minimization, assuming the interface is in the x-z plane as this formulation does.

With the proper reference state chosen, it is possible to unambiguously determine the Burgers vectors for the system using the transformation from lattice state in which the Burgers vector was originally calculated to the one determined by this continuum approach. This methodology can also calculate the interface elastic strain energy of the system. Wave functions for the system are made to be:

$$\mathbf{k}\cdot\mathbf{r} = k_1 x_1 + k_3 x_3 = \left(\frac{n\csc\phi}{|p^{o}_{1}|} - \frac{m\cot\phi}{|p^{o}_{2}|}\right)x_1 + \frac{m}{|p^{o}_{2}|}x_3 \tag{3.10}$$

where n and m are integers, and combined with elastic constants to create the following tensors:

W_1 =

$$\begin{bmatrix} k_1^2C_{11}+2k_1k_3C_{15}+k_3^2C_{55} & k_1^2C_{16}+k_1k_3(C_{14}+C_{56})+k_3^2C_{45} & k_1^2C_{15}+k_1k_3(C_{13}+C_{55})+k_3^2C_{35} \\ & k_1^2C_{66}+2k_1k_3C_{46}+k_3^2C_{44} & k_1^2C_{56}+k_1k_3(C_{36}+C_{45})+k_3^2C_{34} \\ sym & & k_1^2C_{55}+2k_1k_3C_{35}+k_3^2C_{33} \end{bmatrix}$$

$$\mathrm{W}_2 = \begin{bmatrix} k_1C_{16}+k_3C_{56} & k_1C_{16}+k_3C_{25} & k_1C_{14}+k_3C_{45} \\ k_1C_{66}+k_3C_{46} & k_1C_{26}+k_3C_{24} & k_1C_{46}+k_3C_{44} \\ k_1C_{56}+k_3C_{36} & k_1C_{25}+k_3C_{23} & k_1C_{45}+k_3C_{34} \end{bmatrix} \qquad \mathrm{W}_3 = \begin{bmatrix} C_{66} & C_{26} & C_{46} \\ & C_{22} & C_{24} \\ sym & & C_{44} \end{bmatrix}$$

Following the same form as Equation 3.6 (det(Π) = 0 and Π **a** = **0**) and simply replacing the C matrices with the W matrices, the eigenvalues, p^α, and eigenvectors, $\mathbf{a}^\alpha$, are calculated for the state of the system at the interface as opposed to in the far-field. Tractions along the interface are then determined with the following expression:

$$\sigma(x_1, 0, x_3)\mathbf{n} = \sum_{k\neq 0} \exp\left(i2\pi\mathbf{k}\cdot\mathbf{r}\right) \sum_{\alpha=1}^{3} \left(\lambda^\alpha \mathbf{h}^\alpha + \zeta^\alpha \mathbf{h}_*^\alpha\right) \tag{3.11}$$

with λ and ζ are determined by an equation of similar form to Equation 3.7:

$$\sum_{\alpha=1}^{3} \lambda_A^\alpha \mathbf{a}_A^\alpha - \zeta_B^\alpha \mathbf{a}_{*B}^\alpha = \boldsymbol{\vartheta} \tag{3.12}$$

where $\boldsymbol{\vartheta}$ is 0 if mn $\neq$ 0, -b_1 if m = 0, and -b_2 if n = 0. h^α can be related to a^α with:

$$\mathbf{h}^\alpha = (W_2^T + p^\alpha W_3)\mathbf{a}^\alpha \tag{3.13}$$

These traction values can be combined with the displacement discontinuity produced by the dislocations:

$$\Delta u_{dis}(x_1, x_3) = \sum_{n=1}^{\infty} -\frac{b_1}{n\pi} \sin\left(2n\pi \frac{\csc\phi x_1}{|p_1^o|}\right) + \sum_{m=1}^{\infty} -\frac{b_2}{m\pi} \sin\left(2m\pi \frac{x_3 - \cot\phi x_1}{|p_2^o|}\right) \tag{3.14}$$

After summing the tractions and displacements over all wave function, it is then possible to calculate the interface elastic strain energy with use of the divergence theorem:

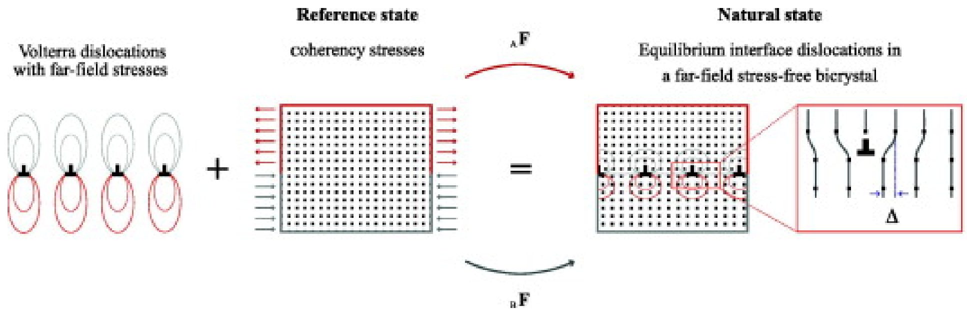

Figure 3.3: Methodology for the the Vattre and Demkowicz method. Reference state is the state in which the strain from deforming the crystals to the reference state is made to balance with the strain fields from the dislocations Reproduced from [106].

$$E_e = \frac{1}{2A} \iint_A \Delta u_{dis}(x_1, x_3)\, \sigma(x_1, 0, x_3)\mathbf{n}\, dS \tag{3.15}$$

where A is the area inside the dislocation array. However, as this formulation assumes Volterra dislocations, there will be a singularity in the energy value at the dislocation itself. Integration therefore begins at a distance of $\frac{1}{2}b$ from the dislocation, a fairly standard approximation for this type of model. This continuum approach is not without its limitations, as in addition to this cutoff issue it cannot consider the affects of interfacial chemistry. It does serve as useful tool to validate atomistic results though, and has the additional benefit of being able to calculated the energetics with changes in lattice and elastic constants.

3.4 Mechanical Response

While there has been very little work done evaluating the mechanical properties of the interfaces under consideration here computationally, the topic has been studied experimentally for decades. The focus of the work has generally been on the macro-scale response of the system as a whole, as opposed to the affect of the microstructure. These studies are still useful to the work undertaken here however, as micro-structural behavior often influences the macro-scale response.

Much of the early work on this topic focused on determining the factors that affect the interlamellar spacing (S) of the pearlite colony. The strength and hardness of pearlite has been shown to follow a Hall-Petch type relation to this spacing [111–113] (Fig. 3.4):

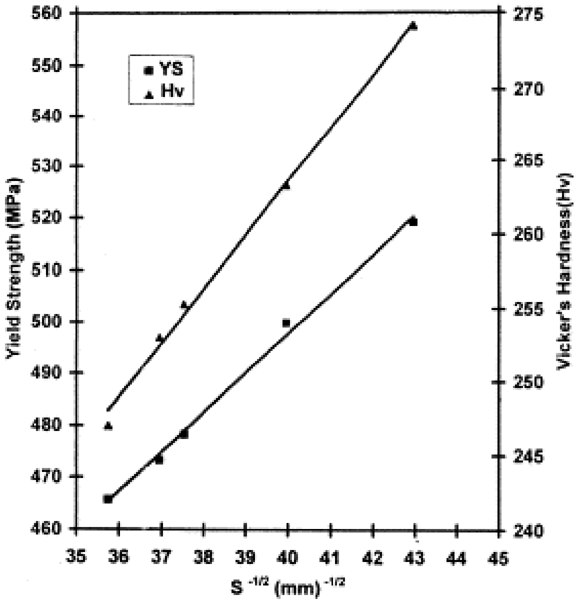

Figure 3.4: Effect of interlammelar spacing on the yield stress (YS) and Vicker's hardness (H_v) of pearlite. Both are shown to follow a Hall-Petch type relationship. Reproduced from [110].

$$\sigma_y = \sigma_0 + \frac{k_y}{\sqrt{S}} \tag{3.16}$$

$$H_v = H_0 + \frac{k_H}{\sqrt{S}} \tag{3.17}$$

These are empirical laws, and values of $\sigma_0 \approx 200$ MPa, $k_y \approx 7.5$ MPa·mm$^{1/2}$, $H_0 \approx 100$ HV, and $k_H \approx 4$ HV·mm$^{1/2}$ have been determined experimentally [110]. It has also been suggested that this spacing will affect other mechanical properties, such as flow stress (σ_f) [114, 115]:

$$\sigma_f = \sigma_y + k' \epsilon_{pl}^{n'} \tag{3.18}$$

where ϵ_{pl} is the true plastic strain, and k' and n' are material constants, estimated to be approximately 2800 MPa and 0.65, respectively, in pearlite. Larger interlamellar spacing has also been found to increase the likelihood of void formation [116], possibly reducing the barrier for delamination at the interface. There are a multitude of factors that play a role in the determination of the spacing within a pearlite colony, including carbon content [117] and austenitizing temperature [118]. The specifics of these formation mechanisms are outside the scope of this dissertation however. Ductility in pearlite colonies has also been studied at great length, and has been found to be related not to interlamellar spacing, but the prior austenite grain size [119]. This appears to arise from the size of pearlite colony that forms, with larger colonies allowing for localized flow over larger distances. As larger austenite grains result in larger pearlite colonies, coarser grained austenite will result in higher ductility within pearlite.

Pearlite's high strength has often been attributed to the cementite interface acting as a barrier to dislocation motion [120, 121], with dislocations in the ferrite lamella of pearlite being well observed [114, 122]. It has also been proposed that this interface acts as a nucleation site for dislocations [115, 123], which has been observed computationally by the author [124]. There has been very little discussion of dislocations in the cementite lamella of pearlite [125], however. This likely arrises from the brittle nature of cementite, which suggest and dislocation formation will precede failure of the system. When failure occurs in pearlitic systems though, it has been shown to occur nearly perpendicular to the interface planes within the pearlite [126], suggesting it could in fact be formation of these cementite dislocations. Cementite is known to be able to deform at temperature as low as room temperature [127, 128], with multiple potential slip systems having been characterized [129, 130]. The slip systems were long thought to lie only on the $\{100\}$ and $\{110\}$ family of planes in the cementite, but more recent work has postulated a host of other slip planes including the (102) and (103) [131]. There has also been work by Karkina et al. [131] proposing potential slip transfer mechanism across the ferrite-cementite interface for both the Bagaryatskii and Isaichev ORs. This suggests that this may be an important mechanism in the deformation of pearlite and requires further analysis.

As was noted, much of the experimental work mentioned above examined the macro-scale response of pearlite colonies, and as such generally considered interlamellar spacings outside the realm of atomistics. As there is often localized behavior at smaller scales that is not observed at larger scales, it is important to consider work at these length scales as well. Modi et al. [110] found that below a critical interlammelar spacing ($\approx$ 712 nm), the ultimate tensile strength and ductility remain constant (Fig. 3.5). This is likely due to the residual stress of the ferrite-cementite

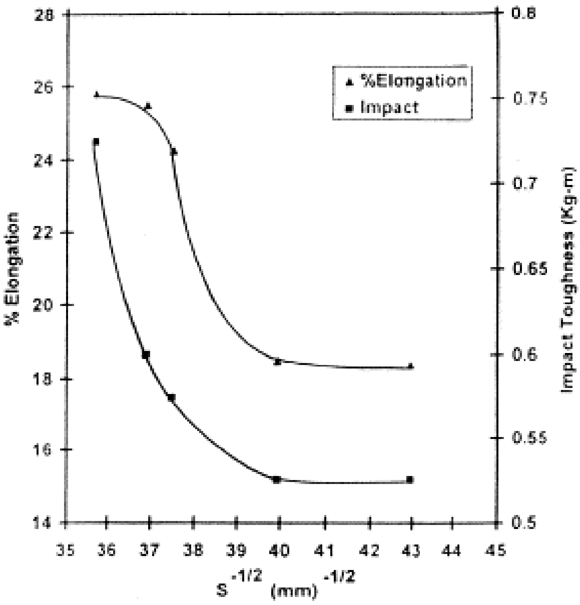

Figure 3.5: Effect of interlammelar spacing on impact toughness and elongation of pearlite. Both are shown to be invariant below a critical type interlamellar spacing ($\approx$ 712 nm). Reproduced from [110].

interface, as the plastic zones emanating from adjacent interfaces begin to overlap. This causes emitted dislocations to interact with each other, limiting their motion. In addition to pearlite, there has also been work done considering localized effects in other ferrite/cementite systems. Mohsenzadeh and Mazinani [132] examined the phenomenon for cementite regions within a ferrite matrix and postulated that the magnitude of the stress drop after ferrite yield could be minimized by increasing the ratio of cementite to ferrite. While pearlite that nucleates from austenite will always have a volume ratio of roughly 7:1 between ferrite and cementite on account of its line compound nature, there are recently developed techniques that allow for the amount of cementite to be increased [133]. This suggests that the volume ratio may be another important variable to consider when analyzing the mechanical response of pearlite.

There has also been analysis on the effects of interfaces in other metallic-ceramic systems. This includes characterization of the interface as a site for crack growth [134] in copper-sapphire, its effect on fracture toughness [135] in aluminum-alumina composites, and how cohesion at the interface influences plasticity of the ductile layer [136] in the SiO_2-TiN system. These studies all highlight the importance of understanding interfacial behavior in order to understand mechanical response. Another study of note is that on the mechanical response within laminates consisting of ductile austenitic steel and a brittle martensitic steel [137]. This work found that the brittle layer was able to reach significantly higher strains when between two ductile layers than would be possible in the bulk material, highlighting the importance of evaluating pearlite as a whole as opposed to just inferring properties from its well studied component phases.

While there has been little work done computationally on pearlite, atomistics are an ideal method for evaluating micro-laminate systems, as both creation and deformation of the structures is a relatively straightforward endeavor. As such, atomistics have been used extensively to study the mechanical response of interfaces [138]. For homophase interfaces, grain boundaries and lamella thickness have been observed to influence the strength of the material in FCC [139], BCC [140], and HCP [141] crystals. Interfaces have also been found to serve as dislocation sources [142, 143] in metals. In studies exploring dynamic conditions, such as copper grain boundaries under shock, it has been shown that coherent grain boundaries will nucleate voids while incoherent grain boundaries will not [144] and that the interface structure can influence the flow stress [145, 146]. There has also been work done on the shear response of heterogeneous interfaces, including Cu-Nb, examining the anisotropy of the shear resistance [56], and Cu-Ta [147], relating the yield stress to the interfacial energy. These studies all highlight the importance of considering the energetics and interface structure when examining mechanical properties. As such, when considering the response of an interface, orientation relationship and interfacial chemistry will almost certainly have an effect on the observed results.

It is worth reiterating that almost all of work mentioned above focuses on the bulk response of pearlite (and other laminates), with very little mention of how these structures response to specific loading states. Additionally, there is no mention of how the specific ORs will influence the response. However there is a clear structure-property relationship in these materials that highlight the importance of obtaining a deeper understanding of the underlying microstructure, particularly at the interface, within pearlitic steels.

Chapter 4

Interatomic Potential Testing

In atomistic simulations, the results will only be as accurate as the interatomic potential used. As such, extensive testing is necessary in order to validate any potentials to be used. For this work, six potentials were initially considered, two EAMs, one by Lau [148] and one by Hepburn [149], two MEAMs, one by Lee [150] and one by Liyanage [151], and two Tersoffs, both by Henriksson [152, 153].

In analyzing the potentials, the first step was to investigate how these potentials model known iron carbides. Table 4.1 shows values for lattice constants, formation energy, and elastic constants for α-Fe, γ-Fe, Fe_3C, Fe_5C_2, Fe_7C_3, graphite, diamond and Fe_4C (both tetragonal and octahedral interstitials). While for the most part these values compare well with each other as well as with experimental and ab-initio observations, there are some variations. As ferrite, austenite, and cementite are the structures being analyzed in this work, it is particularly important that the values from these potentials match with experimental results. This is the case for ferrite and austenite for all the potentials, which is unsurprising as iron potentials are generally fit to these relatively simple crystal structures. For cementite however, the EAMs are notable outliers. The Lau EAM potential yields elastic constants that are both negative and several orders of magnitude too large. Since elastic constants are known to influence both energetics and dislocation behavior, this potential was eliminated from consideration. The Hepburn EAM potential on the other hand poorly predicts the b lattice value for cementite. As lattice constants are the main factor in determining dislocations spacing, this potential was also eliminated as a potential for in depth analysis. It is worth noting that the Hepburn EAM potential's prediction of elastic constants and relative atomic positions for cementite are otherwise accurate, and since its computational cost is significantly lower than that of the MEAM and Tersoff, it proves useful as a benchmark, so some results using this potential have been included in this work.

Table 4.1: Calculated lattice constants (Å), formation energies (eV), and elastic constants (GPa) of iron carbides for the six interatomic potentials initially considered in this work.

	EAM (Hepburn)	EAM (Lau)	MEAM (Lee)	MEAM (Liyange)	Tersoff	Tersoff/ ZBL		EAM (Hepburn)	EAM (Lau)	MEAM (Lee)	MEAM (Liyange)	Tersoff	Tersoff/ ZBL
FCC Fe							Fe_7C_3						
a	3.69	3.66	3.61	3.60	3.61	3.95	a	4.55	4.25	4.84	4.48	4.48	4.45
E/atom	4.23	3.89	4.24	4.17	4.25	4.14	b	6.88	7.11	6.66	6.80	6.55	6.62
C_{11}	228	84.9	193	136	205	206	c	11.9	12.3	11.5	11.6	11.8	11.4
C_{12}	121	49.6	161	169	144	141	E/atom	5.25	4.28	5.29	5.18	5.14	5.06
C_{44}	107	21	81.6	85.8	101	101	C_{11}	393	3.42e4	507	300	378	513
							C_{22}	481	-6490	571	328	408	432
BCC Fe							C_{33}	486	6.03e4	413	306	398	449
a	2.87	2.86	2.86	2.85	2.86	2.89	C_{12}	242	-8150	234	153	151	141
E/atom	4.28	4.01	4.29	4.28	4.28	4.18	C_{23}	271	-2.57e4	260	175	174	199
C_{11}	243	244	243	213	225	219	C_{13}	245	-7980	165	119	140	182
C_{12}	138	146	138	143	142	142	C_{44}	107	8390	114	-2.59e5	117	118
C_{44}	122	116	122	119	128	130	C_{55}	98	2110	78	77.5	89.3	84.6
							C_{66}	93	-218	154	-4.58e5	98.8	68.7
Fe_3C													
a	2.458	4.84	4.64	4.47	4.47	4.48	Fe_5C_2						
b	5.16	4.41	5.18	5.09	5.07	4.96	a	10.4	9.82	10.0	10.0	10.2	9.82
c	6.66	6.50	6.32	6.67	6.45	6.47	b	4.58	4.77	4.83	4.53	4.47	4.49
C_{11}	368	-1.65e6	353	336	373	422	c	5.1	4.52	4.86	4.95	4.85	4.85
C_{22}	398	4.04e6	368	329	332	391	E/atom	5.23	4.48	5.19	5.13	5.13	5.05
C_{33}	417	-6.30e6	345	236	356	370	C_{11}	397	6.76e5	386	565	575	525
C_{12}	213	3.10e6	263	175	174	184	C_{22}	389	8.68e5	458	407	439	487
C_{23}	220	3.87e6	184	142	183	192	C_{33}	433	-2.45e5	424	304	400	455
C_{13}	196	-1.25e6	136	123	133	151	C_{12}	211	5.36e5	222	187	205	195
C_{44}	94	-1.41e4	100	69.4	128	131	C_{23}	254	2.77e5	295	211	229	247
C_{55}	93	6980	34.9	17.9	68.8	50.3	C_{13}	239	-5.92e4	326	218	246	247
C_{66}	107	-4.71e5	103	106	118	136	C_{44}	106	1.17e5	119	121	132	160
							C_{55}	91	-1.96e4	151	113	144	159
Graphite							C_{66}	87	1.61e5	36.3	86.5	109	89.2
a	3.03	2.85	2.45	2.53	2.51	2.52	C_{15}	8.7	-1.42e5	-4.8	-12.2	1.39	14.5
c	8.38	8.38	8.38	8.46	8.38	8.38	C_{25}	1.9	-3.54e5	-16.4	-7.11	1.41	4.32
E/atom	5.09	3.05	7.33	7.37	7.38	7.36	C_{35}	-1.4	-4.4e5	-41	-33.5	-3.39	-5.48
C_{11}	232	5310	848	748	678	679	C_{46}	5.2	-7.54e4	9.12	-1.2	12.3	-2.2
C_{12}	232	5190	26	42.2	68.9	284							
C_{66}	0	55.4	411	353	5.85	198	Fe_4C Tetragonal						
							a	3.87	3.82	3.99	3.85	3.74	3.77
FeC Rock Salt							E/atom	4.73	4.29	4.38	4.32	4.66	4.41
a	4.07	3.84	4.09	3.84	3.91	3.79	C_{11}	180	804	6.56e6	142	175	181
E/atom	5.65	4.55	5.36	5.82	5.05	5.46	C_{12}	112	-1.21e4	35.9	133	137	136
C_{11}	1270	7.13e4	747	566	732	870	C_{44}	2.07					
C_{12}	645	-386	256	213	74.2	107							
C_{44}	380	-408	37.4	145	55.8	72.6	Fe_4C Octahedral						
							a	3.86	3.78	3.85	3.69	3.71	3.71
							E/atom	4.90	4.29	4.56	4.86	4.82	4.77
							C_{11}	338	822	427	346	365	398
							C_{12}	133	19.8	104	148	111	124
							C_{44}	71.8	-3.3	17.4	68.2	61.1	84.1

Having considered known iron-carbides, it was also important to check that these potentials do not predict any low energy, stable iron-carbides that have not been experimentally observed. The convex hull for the iron carbon system consists of only ferrite and graphite, with cementite being one of the lower energy, but metastable, structures. In order to test this, an evolutionary algorithm, USPEX [154], was used to search for potentially low energy structures. The known iron-carbon structures were seeded into the program, along with 50 randomly generated structures and run for 45 generations. While the convex hulls in Figures 4.1a, b, and d exhibit the straight line that is to be expected, the convex hull for Lee MEAM potential (Fig. 4.1c) predicts low energy structures in the range of 40-50% carbon by composition. These are not experimentally observed structures, and thus this potential was also eliminated from consideration. (Note: EAM potentials lack directionality in their formulations and thus do a poor job of modeling covalent bonds. Thus they poorly predict values for diamond and graphite and produce meaningless convex hulls.) Lastly, while both of the Tersoff potentials are valid, their formulations are nearly identical. Therefore only one was used in this work.

This analysis led to two potentials being chosen, the Tersoff by Henriksson [152] and the MEAM by Liyanage [151], and as such all future references to the Tersoff and MEAM potentials in this work will be referring to these. Tables 4.2-4.4 show the lattice constants and elastic constants computed using these potentials for ferrite, austenite, and cementite, respectively, compared with experimental values.

Table 4.2: The lattice constants and elastic constants of ferrite predicted by the interatomic potential used in this work, as well as experimental values.

	MEAM	Tersoff	Experimental [155]
a (Å)	2.85	2.86	2.87
C_{11} (GPa)	213	225	242
C_{12} (GPa)	143	142	147
C_{44} (GPa)	119	128	112

Table 4.3: The lattice constants and elastic constants of austenite predicted by the interatomic potential used in this work, as well as experimental values.

	MEAM	Tersoff	Experimental [156]
a (Å)	3.60	3.61	3.64
C_{11} (GPa)	169	205	160
C_{12} (GPa)	136	144	130
C_{44} (GPa)	85.8	101	101

Table 4.4: The lattice constants and elastic constants of cementite predicted by the interatomic potential tested used in this work, as well as experimental values.. (NOTE: Experimental elastic constants determined using density functional theory)

	MEAM	Tersoff	Experimental [4, 157]
a (Å)	4.47	4.47	4.52
b (Å)	5.06	5.07	5.09
c (Å)	6.70	6.45	6.74
C_{11} (GPa)	326	373	322
C_{22} (GPa)	322	332	388
C_{33} (GPa)	232	356	345
C_{12} (GPa)	170	174	164
C_{23} (GPa)	137	183	156
C_{13} (GPa)	118	133	162
C_{44} (GPa)	64	128	134
C_{55} (GPa)	17	68.8	15
C_{66} (Gpa)	103	118	134

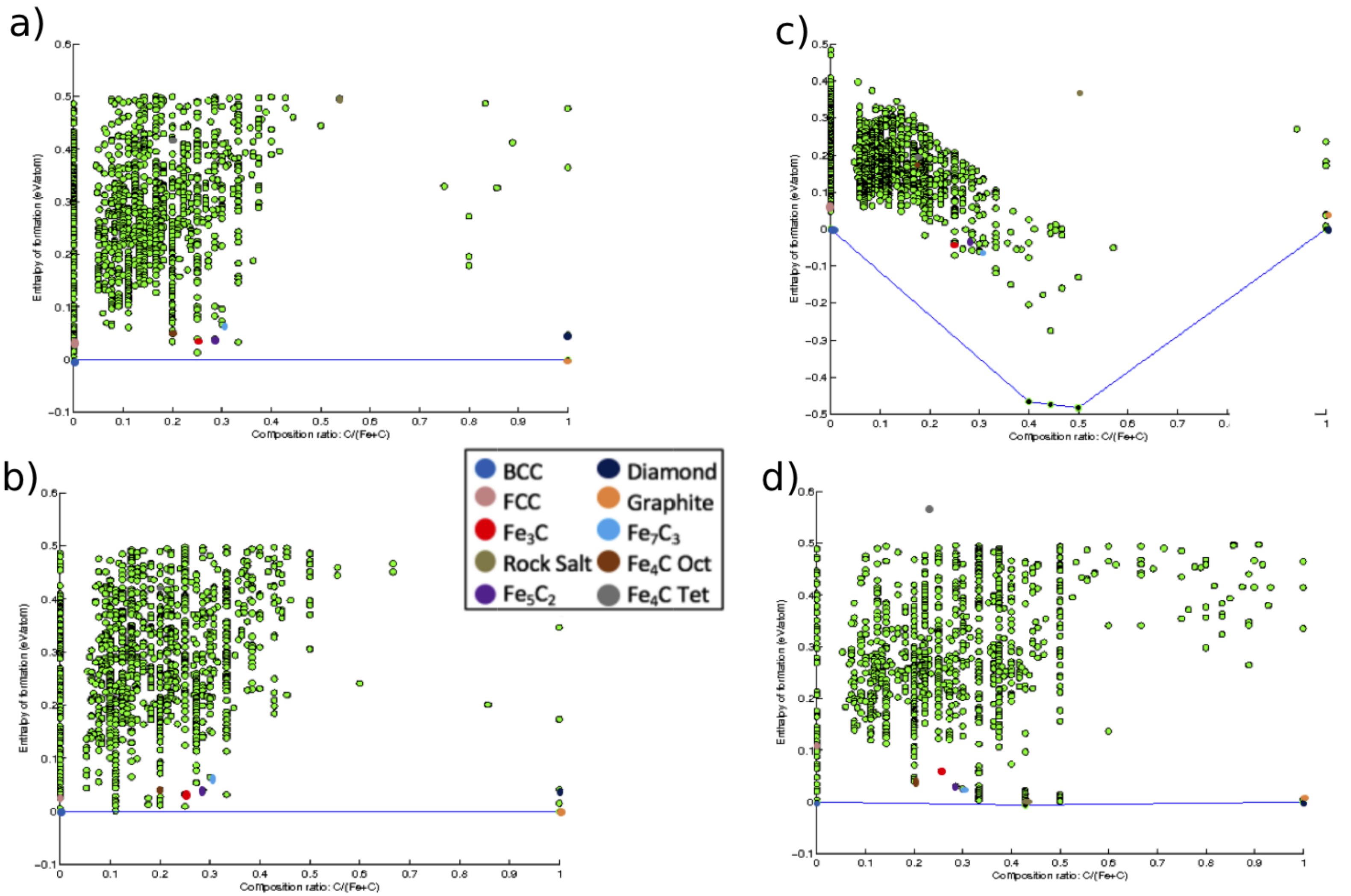

Figure 4.1: Convex hulls for the a) Henriksson Tersoff b) Henriksson Tersoff/ZBL c) Lee MEAM and d) Liyange MEAM potentials.

Chapter 5

Interface Energy and Structure

5.1 Ferrite-Cementite

In order to maximize use of computational resources, a single orientation was chosen, the Bagaryatskii OR, to initially develop and test scripts and methodology on. Once the approach was deemed successful, simulations were then run on the other ORs. As such, their will be an in depth discussion as to the approach used to obtain the results for the Bagaryatskii, with only the relevant results and comparisons between the ORs discussed for the others.

5.1.1 The Bagaryatskii Orientation Relationship

The Bagaryatskii OR, due to its frequent reports in literature and the high symmetry directions that compose the interface plane, was chosen to be the first OR for analysis. The Bagaryatskii OR is defined as follows:

$$[100]_\theta||[1\bar{1}0]_\alpha$$

$$[010]_\theta||[111]_\alpha$$

$$(001)_\theta||(11\bar{2})_\alpha$$

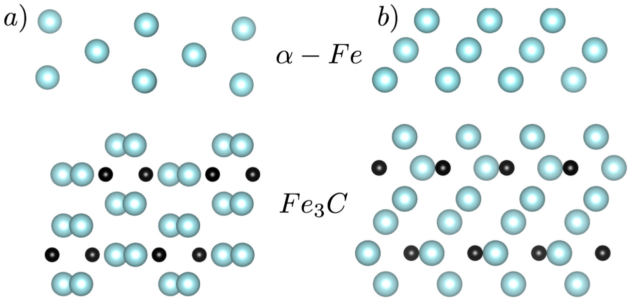

Figure 5.1: The ferrite and cementite structures in the Bagaryatskii OR showing the (a) $(010)_\theta||(111)_\alpha$ projection (b) $(100)_\theta||(1\bar{1}0)_\alpha$ projection.

The Bagaryatskii OR has been observed to have a high degree of registry between ferrite and cementite at the interface. Figure 5.2 shows the positions of the atoms of cementite overlaid with those of ferrite. The iron atoms for both lattices are very close in position, which should facilitate the formation of a low energy semi-coherent interface. The misfit strain can be approximated as: $\epsilon = 2\left|\frac{a_1-a_2}{a_1+a_2}\right|$, yielding strains of 10.7% in the $[100]_\theta||[1\bar{1}0]_\alpha$ direction and 2.4% in the $[010]_\theta||[111]_\alpha$ direction, corroborating the hypothesis of a semi-coherent interface.

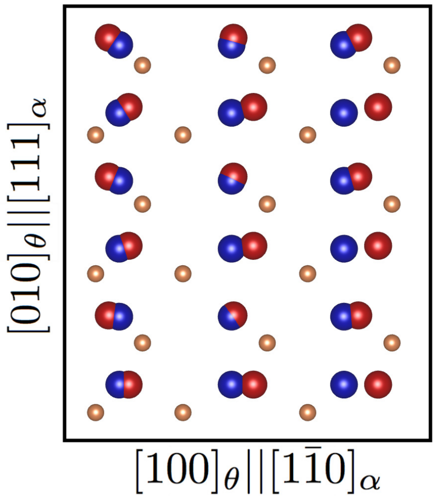

Figure 5.2: The relative positions of atoms of a 3×3 unit cell of cementite overlaid with the matching ferrite layer; the $(001)_\theta||(11\bar{2})_\alpha$ projection. Blue atoms represent $\alpha - Fe$, red represent Fe in Fe_3C, brown C in Fe_3C.

While the orientation relationship fully describes the macroscopic degrees of freedom of the interface, there are additional microscopic degrees of freedom that need to be accounted for in any atomic level description of an interface. One is the relative in-plane positions of the crystals, while another is the terminating planes within each unit cell that comprises the interface itself. The former can be addressed by running multiple simulations as the two lattices are shifted relative to each other within the interface plane and will be discussed in more detail later. As for the latter, due to the high symmetry of the BCC lattice, the structure and chemistry of the terminating planes of the BCC structure are the same, varying only by an in-plane shift. Within the cementite crystal however, there are six distinct terminating planes that could form the interface with the ferrite. These planes can be classified by the atoms in the first two layers starting from the interface (Fig. 5.3): Fe-FeC, FeC-Fe, and Fe-Fe. By this classification, each type of terminating planes occurs twice, denoted as class a and class b in Figure 5.3. In the $[100]_\theta||[1\bar{1}0]_\alpha$ direction, these a and b planes are identical. In the $[010]_\theta||[111]_\alpha$ though, the direction of the atoms in cementite relative to that of the ferrite is different between for the a and b planes i.e. nearby atoms to the terminating plane trend in the positive or negative y directions. This requires that each be analyzed separately to detect if this variation affects the energetics or structure of the interface.

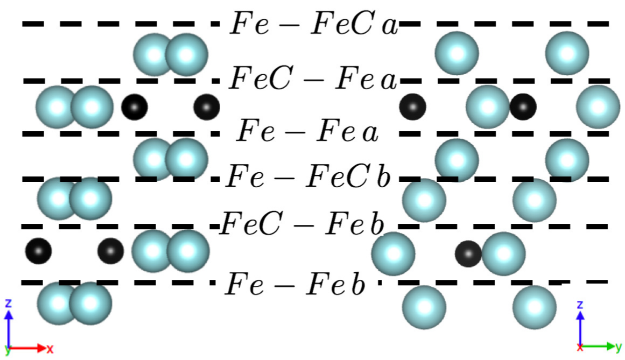

Figure 5.3: Possible terminating planes within the cementite unit cell for the Bagaryatskii OR. The dotted lines represent where the cementite structures is cut to form and interface with ferrite. The atoms below the dashed line represent the structure of cementite at the interface. Three pairs of terminating plane can be described by the atomic content of their first two layers (from dotted line down): Fe-FeC, FeC-Fe, Fe-Fe. Additionally, due to differences in the relative direction of the atoms in the $(100)_\theta||(1\bar{1}0)_\alpha$ projection plane, each pair of planes is further differentiated into two classes: a and b.

The simulations domains are constructed to be sufficiently large as to allow for extended defects to form and minimize elastic strain required for in-plane periodicity. All simulations are made to be periodic in the directions of the interface and have free surfaces in the direction normal to the interface. The interface plane dimensions are made to be a multiple of the ferrite lattice in the relevant directions and the cementite lattice was then strained to fit these dimension, followed by subsequent relaxation of the total energy and stress. Dimensions are deemed sufficient when the imposed elastic strain on the cementite, prior to relaxation, was less than 0.5%. Six repeats of each lattice in the normal direction are found to be sufficient to eliminate the effects of free surfaces on

Table 5.1: The details of the Bagaryatskii simulation domains: geometry, strain state, and the number of atoms

	$[100]_\theta \vert\vert [1\bar{1}0]_\alpha$		$[010]_\theta \vert\vert [111]_\alpha$			
	Length(Å)	Strain(%)	Length(Å)	Strain(%)	Height(Å)	Atoms
EAM	24.19	0.14	213.06	0.02	80.96^{a} 82.91^{b} 84.86^{c}	39792^{a} 41172^{b} 42092^{c}
MEAM	205.60	0.01	167.90	-0.01	81.92^{a} 83.92^{b} 85.92^{c}	270576^{a} 279684^{b} 285756^{c}
Tersoff	84.93	0.01	202.73	-0.02	80.71^{a} 82.64^{b} 84.57^{c}	141624^{a} 146412^{b} 149604^{c}

a) Fe-FeC b) FeC-Fe c) Fe-Fe

computed interfacial energies. Table 5.1 shows the dimensions of the simulation, along with in-plane strains. All simulations were performed using the LAMMPS molecular dynamics code [158] using a conjugate gradient minimization technique at 0 K using a Parrinello-Rahmen barostat.

Interfacial Energy

The interfacial energy is computed using the slab method (Eq. 2.4). In order to account for the in-plane DOF, the origin of ferrite portion of the simulation is shifted by increments of 20% of its unit cell. This in-plane shifting has the added effect of modeling the various interface planes of ferrite. However, the different terminating planes of cementite need to be accounted for directly. All six possible terminating planes were modeled, and there was noticeable variation in the energetics of the three different cementite plane types. There was however, no distinguishable difference in the energies between the a and b planes. Table 5.2 shows the results of these simulations, and while the magnitudes of the interfacial energies predicted by each potential are different, there is a clear trend regarding the role of the interfacial chemistry (or terminating plane). The interface energies for the various terminating planes are ordered: FeC-Fe $<$ Fe-FeC $<$ Fe-Fe. This clearly suggests that chemistry plays a major role in determining the interfacial energy, and highlights the shortcomings of other atomistic studies of this system that failed to account for it.

Table 5.2: The interfacial energy of the Bagaryatskii OR predicted by the interatomic potentials for the three cementite terminating planes (J/m^2)

		Range	Mean	Standard Deviation
Tersoff	FeC-Fe	0.45-0.58	0.52	0.05
	Fe-FeC	0.93-1.14	1.03	0.06
	Fe-Fe	2.26-2.32	2.29	0.02
EAM	FeC-Fe	1.10-1.32	1.23	0.06
	Fe-FeC	1.45-1.56	1.47	0.03
	Fe-Fe	2.48-2.75	2.65	0.06
MEAM	FeC-Fe	0.83-0.92	0.88	0.04
	Fe-FeC	1.04-1.19	1.12	0.03
	Fe-Fe	2.21-2.40	2.31	0.07

Interfacial Structure

The structure of the relaxed Bagaryatskii OR interface, as elucidated by the atomistic simulations, is a set of orthogonal dislocations along the $[100]_\theta||[1\bar{1}0]_\alpha$ and $[010]_\theta||[111]_\alpha$ directions as shown in Figures 5.4 and 5.5. Figure 5.4a plots displacement vectors of the atoms in the interface, which clearly shows the formation of two sets of parallel regions with a higher density of atoms. The atomic rearrangement is also shown through an analysis of the change of the energy of the interfacial atoms relative to their bulk values, as shown in Figure 5.4b. Similar interfacial structures are formed for all three potentials, each terminating plane, as well as all in-plane shifts. Additionally, the dislocation spacing remains constant as the simulation dimensions are increased. This suggests the general features of the interfacial structure is independent of the local chemistry and is tied to the misfit strain. It should be noted that while all potentials exhibited the same behavior, the Tersoff potential was chosen for in-depth structural analysis as it provided the necessary combination of accuracy and a lower computational cost.

From the analysis of the interfacial energy, it is noted that there are differences between the various cementite terminating planes that suggests there should be structural differences as well. These differences must lie in the details of the dislocation itself since the dislocation spacing and line direction remained the same for all the analyzed chemistry. One approach to quantify and visualize these differences is through the use of cluster analysis. This algorithm within the OVITO [159] vi-

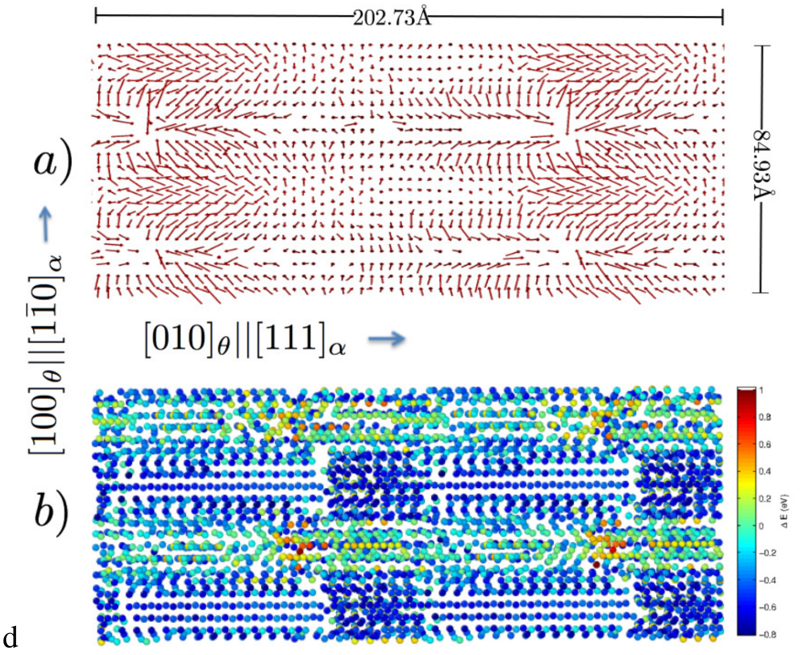

Figure 5.4: The local interfacial structure of the FeC-Fe interface modeled by the Tersoff potential a) Displacement map of the atoms between their bulk and interfacial positions b) Energy map showing the difference of atomic energy in the interface relative to the bulk. These maps highlight the formation of dislocations in the interface.

sualization program analyzes the positions of all the atoms and determines continuous groups that are within an assigned cutoff radius. By choosing a value slightly smaller than that of the nearest neighbor in the ferrite lattice, it becomes possible to assign a relative size to the dislocations. While this is a qualitative measurement to be sure, it does allow for the comparison of the dislocations in each interfacial chemistry of an OR.

Figure 5.5 shows the results of the cluster analysis applied to ferrite for the various terminating planes modeled using the Tersoff potential and a cutoff radius 0.03 Å less than that of the nearest neighbor in the BCC lattice of ferrite. The resultant regions allows for the determination of the spacing of the dislocations, as well as relative widths and heights of the dislocation for the given cutoff radius. It is noted that the spacings observed using this method are consistent with those observed in the displacement and energy maps (Fig. 5.4a,b). And while the size of the regions from cluster analysis are relative, they are a function of the cutoff for allowable variation from the undeformed lattice, there are discernible trends. Figure 5.6 shows these values for spacing, height,

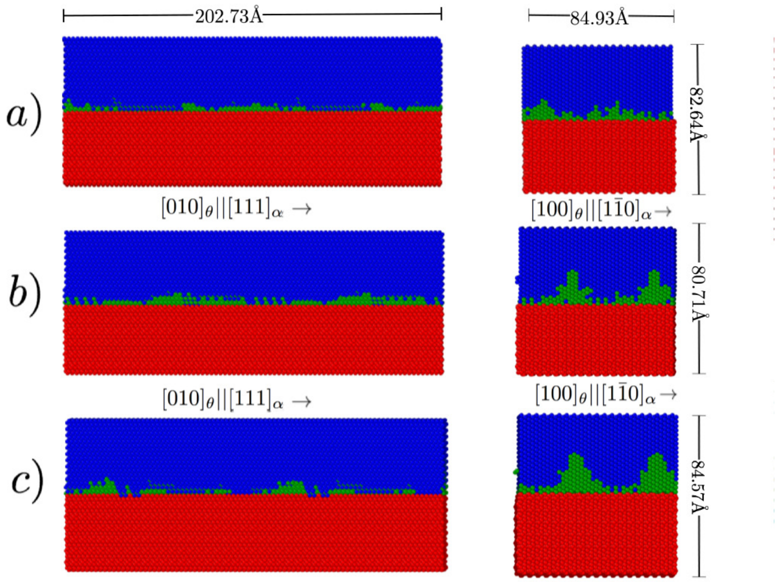

Figure 5.5: Visualization of atoms in ferrite displaced by the formation of interfacial dislocations for the Tersoff potential using cluster analysis. Green represents ferrite atoms with displacement greater than 0.03 Å from BCC lattice positions. (a) FeC-Fe terminating plane (b) Fe-FeC terminating plane (c) Fe-Fe terminating plane.

and width of the dislocations for each terminating plane for the Tersoff potential obtained from the cluster analysis. This reveals three interesting relations: (i) the dislocation spacing remains constant for each dislocation set regardless of terminating plane, (ii) the height and width of the dislocation sets within each terminating plane are notably different, and (iii) the height and width of the dislocation sets vary modestly with terminating plane.

A dislocation spacing that is invariant with respect to the terminating plane is a consequence of the lattice mismatch between the two crystals. If the values from atomistic simulations are compared to those predicted by lattice mistmatch ($\frac{a_1 a_2}{a_1 - a_2}$), it is found that there is excellent agreement for both line directions. Atomistics predicts values of 106.0 Å and 40.5 Å for the $[100]_\theta||[1\bar{1}0]_\alpha$ and $[010]_\theta||[111]_\alpha$ line direction dislocation sets, respectively, while lattice mismatch predicts 105.8 Å and 42.5 Å.

Figure 5.6 demonstrates that two orthogonal sets of dislocations within any single interface are structurally quite different. The $[100]_\theta||[1\bar{1}0]_\alpha$ dislocation spreads out significantly more than the

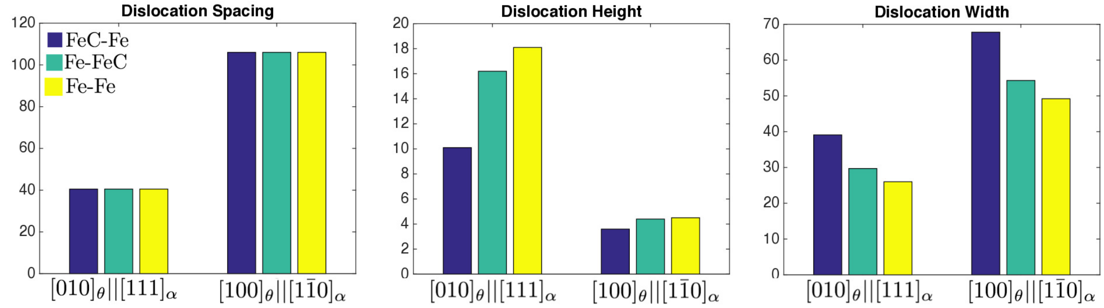

Figure 5.6: The spacing, relative height, and relative width (Å) of the displaced atoms obtained from cluster analysis (Fig. 5.5) for the Tersoff Potential. Three trends can observed here: constant dislocation spacing, increasing dislocation height, and decreasing dislocation width.

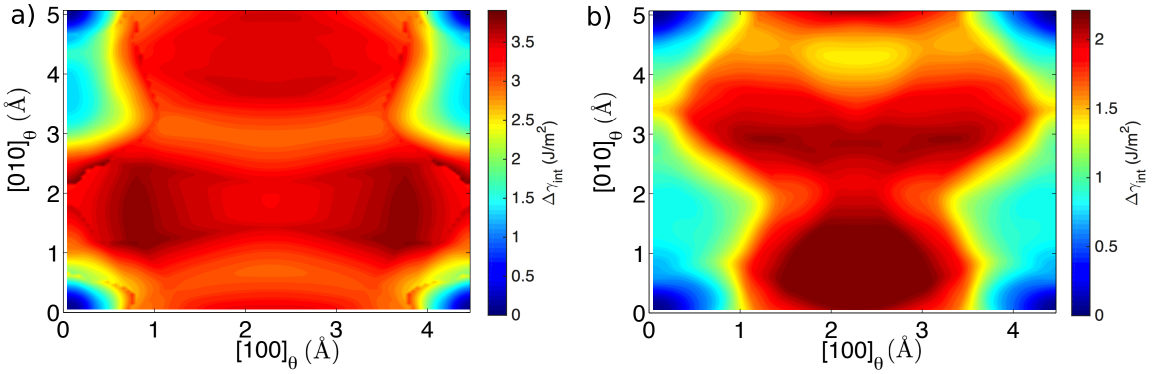

Figure 5.7: Generalized stacking fault surfaces of cementite generated using the Tersoff potential between a) Fe-Fe layers b) Fe-FeC layers. These surfaces predict higher stacking fault energy in the $[100]_\theta$ direction for both, and lower overall stacking fault energy between the Fe and FeC layers.

$[010]_\theta||[111]_\alpha$ dislocations. Dislocation core spreading is commonly associated with the Peierls-Nabarro model [160], with spreading being inversely related to the generalized stacking fault energy (GSF) in the direction of the spreading. While it is not possible to create a GSF energy surface for the interface itself, it is possible to make an approximation using the cementite crystal structure, due to its structural similarities with ferrite at the interface. This can be observed in the relatively high coherency between the iron atoms in the cementite and ferrite lattices at the interface seen in Figure 5.2. This allows the terminating planes in the cementite unit cell to becomes a valid, albeit rough, substitute for the interface itself. Kar'kina et al. [130] computed the generalized stacking fault energies of cementite on the $(001)_\theta$ plane and found that the $[100]_\theta$ direction has a stacking fault energy significantly higher than that of the $[010]_\theta$ direction. These stacking fault energies are a function of many variables though, including geometry, elastic moduli and terminating plane chemistry. Therefore it is necessary to compute these energies with the potentials used in these simulations. The Tersoff generalized stacking fault surfaces found similar results as Kar'kina, as seen in Figure 5.7. The $[100]_\theta$ direction is perpendicular to the more compact dislocation, the $[010]_\theta||[111]_\alpha$, and the higher stacking fault energy would provide a larger resistive force to spreading. Thus, it would be expected that dislocation in the $[010]_\theta||[111]_\alpha$ would be more compact than the $[100]_\theta||[1\bar{1}0]_\alpha$, as is observed in the simulations.

The other notable result from the cluster analysis is that the heights and widths of the dislocations vary with the terminating planes of the cementite structure. By comparing Figure 5.6 and Table 5.2, it is noted that the width of the dislocations decrease and the heights increase as the interfacial energy increases. This suggests that higher interfacial energy is related, at least in part, to the inability of the dislocations to spread; which again can be related to the lattice resistance in cementite. Kar'kina [130] also considered two planes within the cementite structure, one between an FeC and Fe layer, analogous to the FeC-Fe interface plane, and another between two layers of Fe, which would be similar to the Fe-FeC and Fe-Fe interface. They showed that the stacking fault energy was lower between the FeC and Fe layers, which is consistent with the findings here. However, these results do not fully explain why the Fe-FeC and Fe-Fe interfaces have different energies. The most obvious difference between these two interfacial chemistries is the presence of carbon. As it is the FeC-Fe interface that has the lowest interfacial energy, this suggests that carbon near the interface lowers the energy. The cementite crystal structure itself supports this as the per particle energies show that iron atoms near carbon have a lower energy than both the other iron atoms in cementite and the bulk atoms in the ferrite (-5.11 eV vs -4.86 eV vs -4.28 eV for the Tersoff potential).

As the chemistry of the interface has been seen to be important, it is also necessary to consider that there may be alternate, lower energy interface chemistries that are not described by the terminating planes in cementite. In order to test this hypothesis, simulations were run that removed the

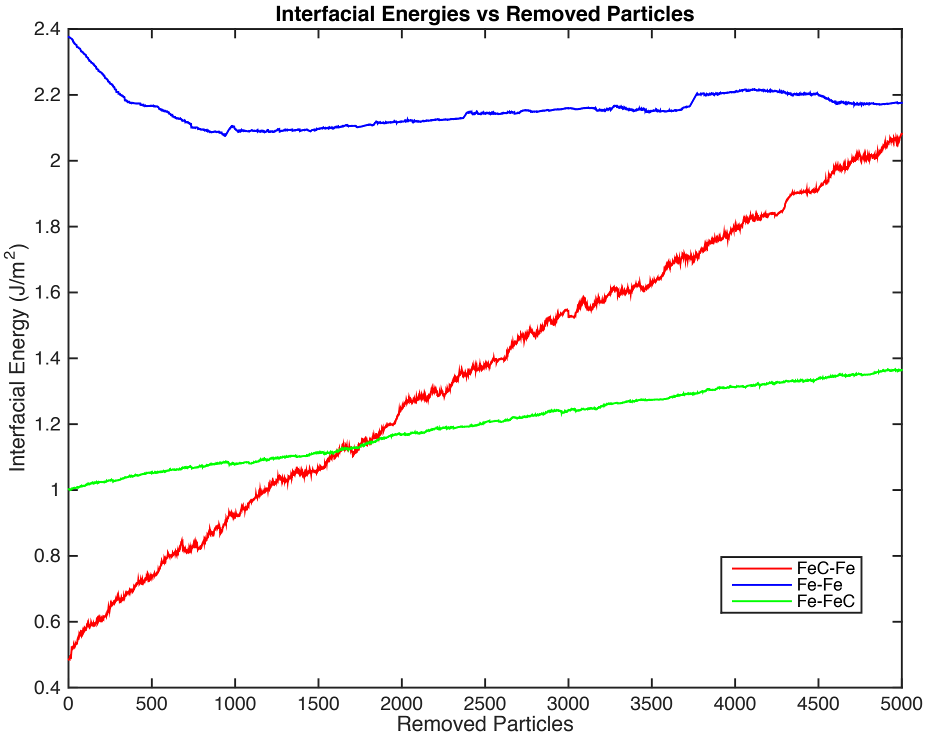

Figure 5.8: Variation in interfacial energy for each terminating planes as the highest energy atoms are sequentially removed. This shows the stability of the FeC-Fe and Fe-FeC interfaces, as well as the lack thereof in the Fe-Fe.

highest energy atom from the relaxed simulation domain. The simulations were then relaxed again, and the process repeated. This was done for each terminating plane, with a total of 5,000 atoms being removed from each. This corresponds to the number of atoms in the first layer immediately adjacent to the interface in both the cementite and ferrite in the FeC-Fe plane, 4998 atoms, and is significantly more than the amount in the Fe-FeC and Fe-Fe terminating planes, 3402 atoms, for the Tersoff potential. Interfacial energy values are then calculated by reducing the bulk energy of the system by the chemical potential of the removed atoms. Figure 5.8 shows the interfacial energy plotted against number of atoms removed. For both the FeC-Fe and Fe-FeC interfaces, the interfacial energy increases after each high energy atom is removed. This suggests a high stability of the original interface, and supports the idea that the FeC-Fe terminating plane is in fact the lowest energy chemistry. Conversely, for the higher energy Fe-Fe terminating plane, the interfacial energy is reduced initially by the removal of these high energy atoms. This is likely due to the previously

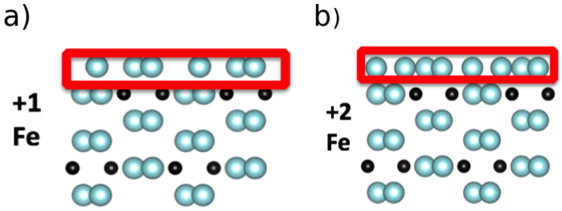

Figure 5.9: Altered cementite unit cells through the addition (a) One Fe atom (b) Two Fe atoms. This increases the areal density of the Fe-FeC interface and shows the the unit cells to be used at the interface in Figure 5.10

noted affect of carbon on lowering the interfacial energy, as the removal of these atoms essentially brings carbon closer to the interface.

While the interfacial energy of the Fe-FeC terminating plane is closer to that of the FeC-Fe, the height and width found through the cluster analysis as well as the stacking fault energy, is much closer in value to that of the Fe-Fe interface. This suggest an additional contributing factor beyond the interfacial energy. It could be hypothesized that the higher planar atomic density of the FeC-Fe interface lowers the stacking fault energy and allows for more in-plane movement of atoms, analogous to motion being easier on smoother surface that a rough one. To test this, Fe atoms were artificially inserted into the Fe-FeC interface layer of the cementite, thus increasing its areal density. Figure 5.9 shows the cementite cells used in the simulation after one (a) and two (b) iron atoms were inserted. This resulted in an additional 798 and 1596 atoms, respectively, being added to the simulation. After the atoms were added, the simulation was relaxed again. While it is not possible to make an exact calculation for interfacial energy, by using the highest energy value for an iron atom (5.11 eV) in the cementite unit cell, a lower bound can be found. This yields values of 2.3 J/m^2 and 2.6 J/m^2 for the two simulations. The actual values are likely higher, as outside of ferrite and graphite, cementite has one of the lowest formation energies per atom of the iron-carbon system. By inserting iron atoms into the lattice, an unstable iron-carbide has essentially been created, one that even after relaxation would have a higher energy per atom. However, it is possible to qualitatively observe the effect it has through the cluster analysis. Figure 5.10 shows the disturbance on the BCC lattice, using the same cutoff value as the previous figures. After

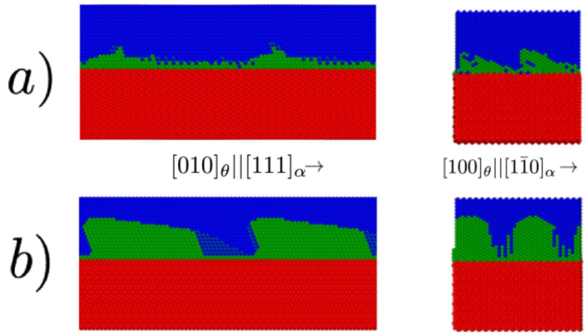

Figure 5.10: Visualization of atoms in the ferrite displaced by the formation of interfacial dislocations for the Tersoff potential using cluster analysis after the insertion of a) one Fe atom into cementite lattice b) two Fe atoms into cementite lattice. Green represents iron atoms with displacement greater than 0.03 Å from BCC lattice positions.

the addition of one atom into the lattice, the size of the region found through cluster analysis is only slightly larger than that of the Fe-FeC. This is despite the high energy cost of embedding the additional atom in the cementite lattice. When another atom is added, the displaced region grows larger. This suggests while areal density plays a role in the structure and energetics of the interface, for reasons of registry at the interface as well as the energy cost of embedding the atoms into the lattice, it is unlikely to create a new lower energy interface.

The existence of interfacial dislocations observed in the atomistic simulations follow long standing classical descriptions of material interfaces [32] and suggest that continuum models can be used to describe some aspects of the interface. A comparison of Figures 2.9 and 5.4 that the Bagaryatskii OR does in fact follow classic O-lattice theory with the O-points and dislocation sharing the same line directions. As such, the formulation of Vattre and Demkowicz [106] was employed for the system. Following the formulation, and using the determined O-points for the Bagaryatskiii, the Burgers vectors are found to have magnitudes of 4.25 Å for the dislocation with line direction $[1\bar{1}0]_\alpha$ and 2.51 Å for the $[111]_\alpha$ line direction. As would be expected, the spacing from Frank-Bilby match the previous estimates from simple lattice mismatch arguments.

It is worth noting however, that while all interatomic potentials exhibited the same trends, there is a discrepancy between the MEAM values reported here, and the interfacial energy determined by Kim et al. [101]. Their value of 0.628 J/m^2 is appreciably lower than the values of any of the interfacial chemistries modeled in this work. This difference likely arises from the simulated annealing procedure used in their work. In order to attempt to reproduce their results, the same method was applied to the simulations performed here. After the initial minimization, the system was given a temperature of 700 K and then ramped down to 5 K over a period of 100 ps using a Nosé-Hoover thermostat and Parrinello-Rahmen barostat. The system was then again minimized at 0 K and zero pressure. This simulated annealing should then find the global minimum for the system. This method did bring find results much closer to those of Kim, with a value of 0.68 J/m^2 for the MEAM potential. However, when applied to the Tersoff potential, there was actually found to be a negative interfacial energy, -0.32 J/m^2, for the FeC-Fe interfacial chemistry. Negative interfacial energies are extremely unlikely for this system however, as they suggest that pearlite would instantaneously form for even the smallest of carbon content within ferrite, which is known to be untrue. A far more likely explanation is that these values actually arise from an improper definition of the initial energy of atoms near the interface.

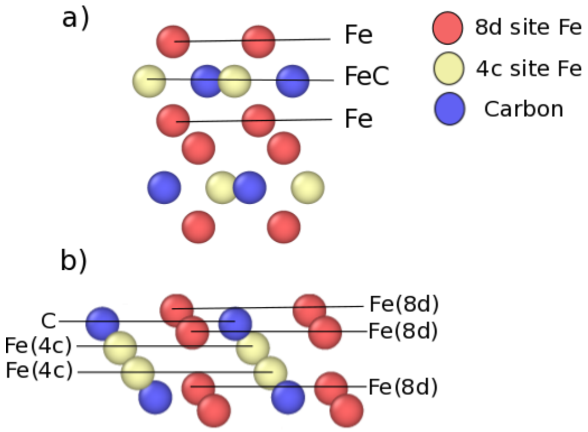

Figure 5.11: Possible interfacial chemistries created by terminating planes within the cementite for the a) Bagaryatskii and Pitsch-Petch ORs b) Isiachev OR. The interface with the ferrite is occurs immediately above these cuts within the cementite unit cell with the interfacial chemistry named for the two layers immediately below the cut. The cementite unit cell contains carbon (blue) and iron in the 8d (red) and 4c (yellow) sites.

5.1.2 Chemical Potential Informed Method

The negative interfacial energy value served as an impetus for the development of a new method for determining interfacial energy. As previously stated, the original calculations for the Bagaryatskii were done using the slab approach:

$$\gamma_{\text{int}} = \frac{E_{\text{tot}} - E_{\alpha} - E_{\theta} - E_{\epsilon}}{L_x L_y} - \gamma_{\alpha} - \gamma_{\theta} \qquad \text{(2.4 revisited)}$$

This approach essentially treats the system as two independent crystals placed adjacent to each other, and all atoms are assigned to the crystal in which they were originally created, regardless of any changes that may occur during minimization. However, due to the fact that there are multiple chemical potentials for iron within the ferrite-cementite system, this formulation may be incorrect. From Figure 5.11, it can be seen that cementite has two possible sites for iron, 8d and 4c, with atoms in these sites have chemical potentials using the Tersoff potential of -5.11 eV and -4.86 eV, respectively. Ferrite atoms are found to have a chemical potential of -4.28 eV. The multiplicity of these chemical potentials creates difficulty in defining the proper initial energy of iron atoms near the interface, as there is ambiguity as to which crystal structure the atom should be associated with. This ambiguity is not unique to the pearlite system, as it has been discussed in other multiphase interfaces [72] as well. Figure 5.12 shows the relative positions of atoms in the Bagaryatskii OR, and it can be observed that there is very little variation between the location of the ferrite atoms and the location of the cementite atoms if the lattice had continued, with the same holding true for the other ORs. This then raises the question of what is the proper choice of the Gibbs dividing surface [161], as an atom that was created as part of the ferrite region, but is adjacent to the cementite region, may quickly fall into one of the iron sites in the cementite, particularly the 8d. Figure 5.13 shows just this, as the ferrite atoms forming the interface are found to have energies closer to that of cementite iron atoms. This layer is only one to two atomic layers thick, and the clustering of these atoms can be observed as they move to form the interfacial dislocations. If these atoms had been created as part of the cementite they would behave in the same manner, yet the "slab" approach would find different interfacial energies despite comparable atomic positions.

This was the guiding consideration in the development of a new technique to calculate the interfacial energy. It was therefore decided to use the chemical potential of the atoms to define where the Gibbs dividing surface is. This approach is conceptually similar to work done by Wang et al. [162] on MgO grain boundaries. In their work, both advanced transmission electron microscopy and DFT are used to determine the proper chemical identity and charge state of impurities at the grain boundary; thus allowing them to accurately track the proper reference state in their interface energy calculations. Because classical atomistic simulations can determine the chemical potential of individual atoms, a more straightforward approach is developed for pinpointing the proper reference state. A binning technique is used that groups atoms according to which of the bulk ferrite or cementite chemical potentials is closest to the atom's final, relaxed energy. The change in the energy of an atom, ΔE, is then defined as the difference between its relaxed per atom energy as calculated by LAMMPS and the chemical potential of its associated bin. The interfacial energy can then be defined as the sum of ΔE for all atoms within 20 Å of the interface, far enough that the energy contribution of the interfacial structures to the per atom energies approach zero, divided by the area of the interface:

$$\gamma_{\text{int}} = \frac{\sum\limits_{i=1}^{N} \Delta E_i - E_\epsilon}{L_x L_y} \tag{5.1}$$

where N is the number of atoms in the system. It is worth noting that only atoms near the interface, roughly two atomic layers, will potentially have there initial energies altered from their created state by this new approach. For atoms further away from the interface, the associated bin will be that of the crystallographic site in which it was created, resulting in the same ΔE values that would be found using the slab method. This approach will also result in identical interfacial energy values for systems in which no elements have multiple chemical potentials. The appropriateness of this Chemical Potential Informed (CPI) method is supported further by the process through which pearlite forms. During the eutectoid transformation of austenite, carbon within the matrix diffuses and nucleates regions of cementite, with the carbon deficient austenite transforming into ferrite. As such, even in its formation there is ambiguity as to which matrix the iron atoms are part of, and thus it seems it appropriate that the method for determining the interfacial energy accounts for this. The CPI approach was therefore applied to the Bagaryatskii OR and found to yield a positive energy for FeC-Fe interfacial chemistry, with a value of 0.40 J/m^2. This value is much more physically realistic and is within the range of experimentally observed values. However before any definitive statement on the appropriateness of the CPI method can made it is necessary to apply it to the other ORs.

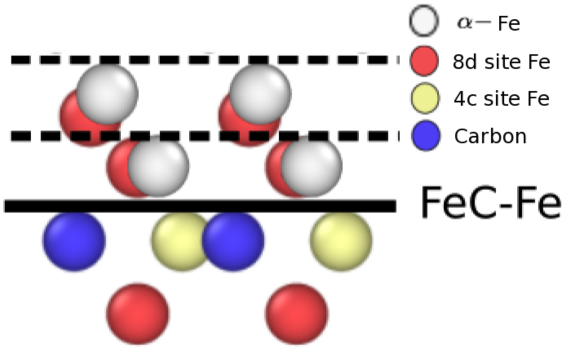

Figure 5.12: Comparison of ferrite atomic positions (white) with those of cementite if the crystal structure were continued past the interface of the FeC-Fe interfacial chemistry of the Bagaryatskii OR. There is seen to be excellent alignment between the two lattices, highlighting the difficulty in choosing the proper Gibbs dividing surface, as either of the dashed lines could also be a reasonable approximation. The cementite unit cell contains carbon (blue) and iron in the 8d (red) and 4c (yellow) sites.

With a methodology in place and two approaches for calculating interfacial energy, simulations were then constructed for the other ORs. While the in-plane periodicity was sufficient to create ORs in which the symmetries were within the interface plane and orthogonal (the Bagaryatskii and Isaichev), the other ORs required the determination of crystallographic directions that would create the proper angular alignment between the two lattices. Due to computational limitations, the creation of periodic simulation boxes that matched perfectly with the proposed ORs was not possible, however all were built for the aligned planes to be within a tolerance of 0.15°. As interfacial chemistry was seen to play a significant role in the interfacial energy of the Bagaryatskii, it was also necessary to account for it in the other ORs. The potential chemistries for the Bagaryatskii,

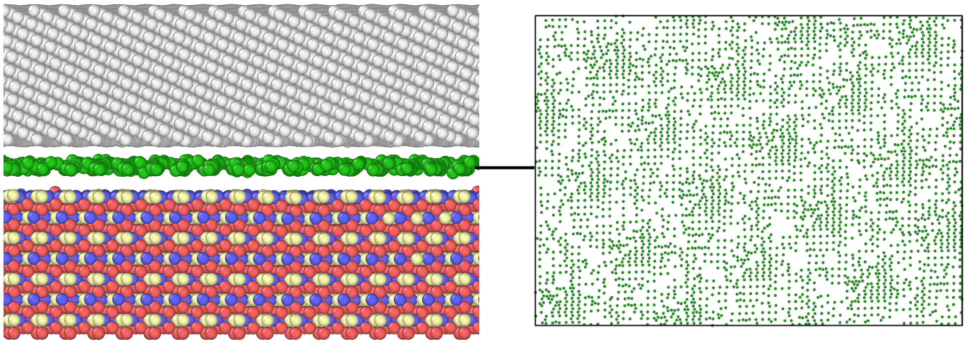

Figure 5.13: Example of ambiguity in defining the Gibbs dividing surface for the FeC-Fe interface of the Pitsch-Petch OR. The layer of green atoms represents iron atoms that were orginally created as part of the ferrite lattice but after relaxation are found to have atomic energies closer to that of cementite iron atoms. It is these bulk crystal chemical potentials that are used to define the bins of the CPI approach, which are ferrite iron (white), carbon (blue) and cementite iron in the 8d (red) and 4c (yellow) sites. Color available online.

the Pitsch-Petch, and their “near" ORs, are the same, and thus the FeC-Fe, the Fe-FeC, and the Fe-Fe (Fig. 5.11a), were once again created. The Isaichev has a different cementite orientation than the other, however a similar convention is used for the five proposed terminating planes of the Isaichev OR, although in this case the specific sites of the iron in the cementite, 8d and 4c, must be differentiated. This resulted in the Fe(8d)-C, C-Fe(8d), Fe(8d)-Fe(4c), Fe(4c)-Fe(4c), and Fe(4c)-Fe(8d) as possible chemistries, which correspond to models 1-5 in the DFT study of the Isaichev by Zhou [98]. For each OR and chemistry nine different in-plane shifts simulations were performed. The free surfaces normal to the interface for all ORs were made to be far enough away as to not influence the interfacial energy, >30 Å, for each layer. All data pertaining to orientation and initial box size of the simulations can be found in Table 5.3. The simulating annealing procedure was used for all simulations and the energetics were determined using both the slab and CPI approaches. While all in-depth structural analysis was done using the Tersoff potential, the energetics using the MEAM potential were also determined to ensure that any observed trends were not simply a function of the potential used.

A brief summary of the structure and energetics of all ORs will be presented below before moving on to an in-depth comparison between all of them.

Table 5.3: Crystallographic directions, associated dimensions (Å), and initial straining of the cementite lattice used to construct simulation cells for the ORs considered in this work using the Tersoff potential.

	Orientation	x	y	z
Isaichev	$[101]_\theta \Vert [01\bar{1}]_\alpha, [010]_\theta \Vert [111]_\alpha, (10\bar{1})_\theta \Vert (2\bar{1}1)_\alpha$	133.5 (0.03%)	208.1 (-0.11%)	83.3-85.3
Pitsch-Petch	$[100]_\theta \Vert [\bar{1}0\ 31\ 1\bar{2}]_\alpha, [010]_\theta \Vert [\bar{1}\bar{1}\ 10\ 35]_\alpha, (001)_\theta \Vert (521)_\alpha$	298.5 (-0.09%)	216.4 (-0.21%)	61.1-63.5
Near Bagaryatskii	$[100]_\theta \Vert [\bar{1}\ 12\ \bar{1}\bar{1}]_\alpha, [010]_\theta \Vert [111]_\alpha, (001)_\theta \Vert (23\ \bar{1}0\ 13)$	233.2 (0.30%)	212.2 (-0.16%)	74.4-76.8
Near Pitsch-Petch	$[010]_\theta \Vert [\bar{1}13]_\alpha, [100]_\theta \Vert [\bar{1}\bar{2}\ 39\ \bar{1}\bar{7}]_\alpha, (001)_\theta \Vert (134\ 53\ 27)$	194.4 (-0.42%)	124.8 (-0.34%)	74.4-76.8

5.1.3 Near Bagaryatskii Orientation Relationship

The Near Bagaryatskii orientation is given as follows:

$$[010]_\theta || [111]_\alpha$$

$$(103)_\theta || (110)_\alpha$$

This OR differs from its parent by only a rotation of the ferrite of 4.3° about the $[111]_\alpha$ direction in order to align the $(103)_\theta$ and $(110)_\alpha$ planes. As a result the coherency at the interface of this OR is nearly identical to that of the Bagaryatskii. However, as can be seen in Figure 5.14d, this rotation results in large change in the interface structure of the OR. Much of this arrises from the alignment of a high symmetry $[11\bar{1}]_\alpha$ direction that had previously been out of plane being brought closer to the interface plane. Using Frank-Bilby this direction was found to be one of the Burgers vector, along with the $[111]_\alpha$ direction that it share with the Bagaryatskii. Line directions and spacing were also found to be in good agreement, with values of 90° and 143.5° versus the predicted 90° and 148.1°, and spacing of 18.1 Å and 52.5 Å as opposed to the 18.8 Å and 47.8 Å predicted by Frank-Bilby.

The interfacial energy of the Near Bagaryatskii was also calculated. The OR shares the same possible interfacial chemistries with its parent ORs, and from Table 5.4 it can be same the interfacial chemistries follow the same trends, FeC-Fe < Fe-FeC < Fe-Fe. Similar to the Bagaryatskii, the lowest energy chemistry is once again found to have negative interfacial energy, lending more credence to the CPI approach. There is a discrepancy between the Tersoff and MEAM potentials here however, as the Tersoff predicts the Near Bagaryatskii to be significantly lower than its parent

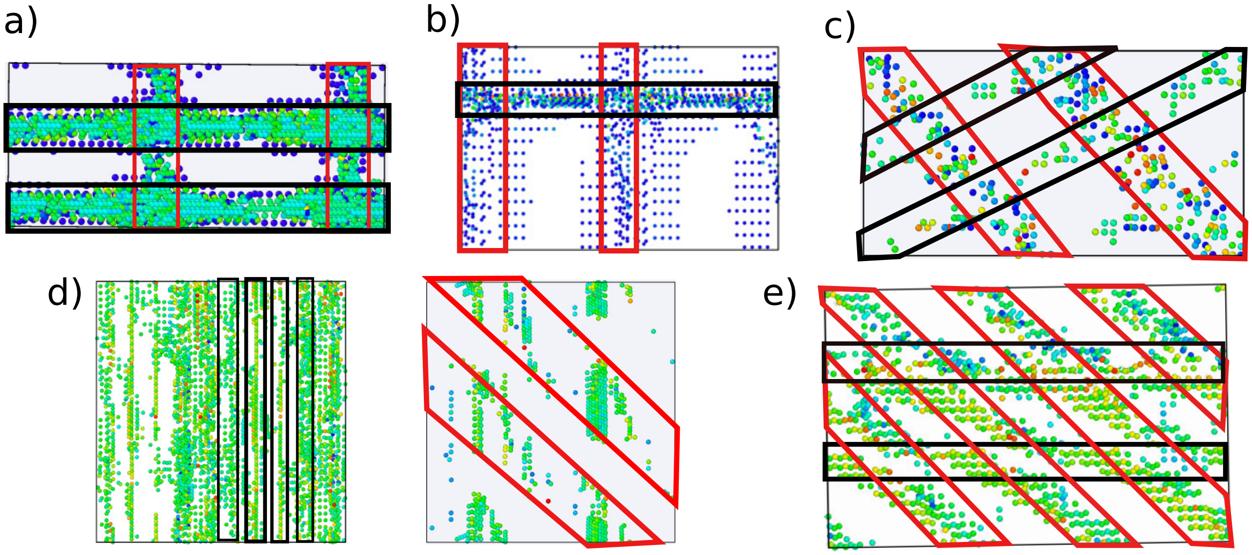

Figure 5.14: Interfacial dislocations for the a) Bagaryatskii, b) Isaichev, c) Pitsch-Petch, d) Near Bagaryatskii, and e) Near Pitsch-Petch ORs formed after simulation relaxation. Dislocations were visualized through plotting the energetics of atoms that were displaced more than 1 Å from their initial, unrelaxed position. Dislocations corresponding to sets one and two in Table 5.8 are outlined in black and red, respectively.

OR, while the MEAM finds them to be nearly identical. This suggests that further investigation may be necessary to determine if this OR is in fact the more energetically favorable.

Table 5.4: The computed interfacial energy (J/m^2) for the interfacial chemistries of the Near Bagaryatskii OR.

		FeC-Fe	Fe-FeC	Fe-Fe
Tersoff	Slab	-0.21	0.66	1.47
	CPI	0.28	0.38	0.78
MEAM	Slab	0.57	0.81	0.88
	CPI	0.38	0.42	0.78

5.1.4 Pitsch-Petch Orientation Relationship

The orientation for the Pitsch-Petch [11] is given by:

$$[100]_\theta \text{ } 2.6^\circ \text{ from } [\bar{1}3\bar{1}]_\alpha$$

$$[010]_\theta \text{ } 2.6^\circ \text{ from } [\bar{1}13]_\alpha$$

$$(001)_\theta||(521)_\alpha$$

The favorability of this OR arises from the near alignment of the high symmetry $\langle 113\rangle_\alpha$ directions in the ferrite to the $[100]_\theta$ and $[010]_\theta$ directions in the cementite. However the slight misorientation of the Pitsch-Petch does create some difficulties in producing the simulation cell as it results in irrational directions aligning with the $[100]_\theta$ and $[010]_\theta$. It was therefore necessary to determine rational directions that approximated these directions, while still allowing for the creation of a reasonable simulation size. The $[\bar{1}0\ 31\ \bar{1}2]_\alpha$ and $[\bar{1}1\ 10\ 35]_\alpha$ were found to fulfill this requirement, creating angles of 2.49° and 2.73° with the $\langle 113\rangle_\alpha$ directions.

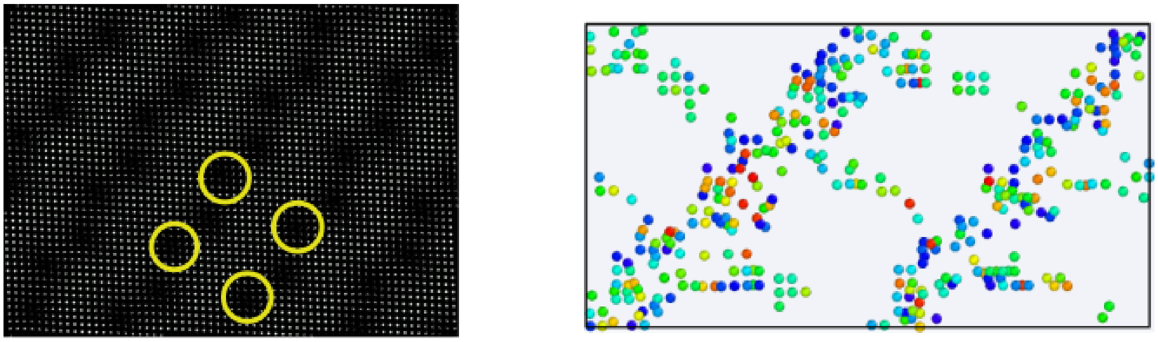

Figure 5.15: O-lattice points and interfacial dislocation structure of the Pitsch-Petch OR. As is postulated by O-lattice theory, O-points and line directions are found to be parallel.

From Figure 5.15 it can be observed that unlike the Bagaryatskii OR where the dislocation line directions were in the same direction as the symmetries, here they lie in the less intuitive directions of $35.7°$ and $135.2°$ from the $[100]_\theta$ directions. Spacings for these dislocations were found to be 58.5 Å and 60.3 Å, respectively. As is predicted by O-lattice theory the O-points are found to be aligned with the line directions after relaxation, so Frank-Bilby was applied to the interface structure. This yielded values that were in good agreement with atomistics for both line direction, 37.7° and 124.2°, and spacings, 61.4 Å and 61.8 Å. Burgers vectors were found to be of the $[100]_\theta||\frac{1}{2}[\bar{1}3\bar{1}]_\alpha$ and $[010]_\theta||\frac{1}{2}[\bar{1}13]_\alpha$ character (Fig. 5.16), consistent with the symmetries of the system. Application of the continuum model to the system determined these Burgers to be 4.61 Å, 1.40° from the $[100]_\theta$ and 4.90 Å, 1.45° from the $[010]_\theta$.

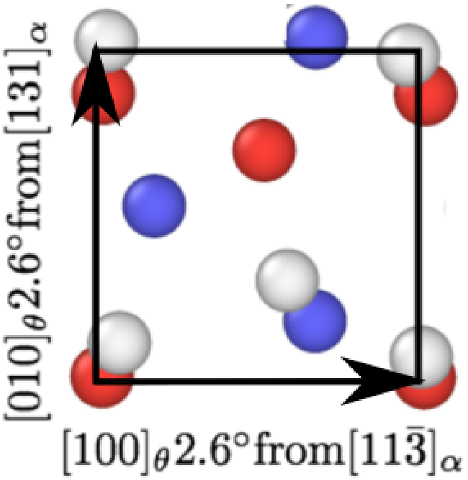

Figure 5.16: Interface coherency and Burgers vectors of the Pitsch-Petch OR. Burgers vectors are found to lie in the symmetry directions of the Pitsch-Petch, the $[100]_\theta||\frac{1}{2}[\bar{1}3\bar{1}]_\alpha$ and $[010]_\theta||\frac{1}{2}[\bar{1}13]_\alpha$. The interfaces shown consist of ferrite iron (white) and cementite carbon (blue) and iron (red and yellow).

Energetic analysis of the Pitsch-Petch found the chemistries to again have the same trend of the FeC-Fe having the lowest energy and the Fe-Fe with the highest. A negative energy value was again calculated using the Tersoff potential as well. Using the CPI method the energy of the FeC-Fe interfacial chemistry to be very close to that of the Bagaryatskii. This holds with what would be expected from experimental results, as the lack of consensus on ORs may arise from similar interfacial energetics.

Table 5.5: The computed interfacial energy (J/m^2) for the interfacial chemistries of the Pitsch-Petch OR.

		FeC-Fe	Fe-FeC	Fe-Fe
Tersoff	Slab	-0.05	0.75	1.53
	CPI	0.39	0.48	0.59
MEAM	Slab	0.66	0.90	0.95
	CPI	0.44	0.54	0.57

5.1.5 Near Pitsch-Petch Orientation Relationship

The Near Pitsch-Petch differs from its parent OR by two rotations. The first is the rotation of the $[\bar{1}13]_\alpha$ by 2.6° in order align it with the $[010]_\theta$ direction of the cementite. The ferrite lattice is then rotated about this new shared axis so as to align the $(103)_\theta$ and $(110)_\alpha$ planes. As such, the OR is described by these symmetries:

$$[010]_\theta||[\bar{1}31]_\alpha$$
$$(103)_\theta||(110)_\alpha$$

Much like the Near Bagaryatskii, these relatively small rotations result in a fairly substantial change in the interface structure of this OR (Fig. 5.14e). This change in structure arises for the same reasons as well, the rotation of a $\langle 111\rangle_\alpha$ direction nearer to the interface plane. This results in a change in Burgers vector from the $[100]_\theta||[\bar{1}3\bar{1}]_\alpha$ to the $\frac{1}{2}[1\bar{1}1]_\alpha$ (Fig. 5.17). As is to be expected, one line direction lies in the shared symmetry direction, while the other then lies at an angle of 118.7° from the $[100]_\theta$ in the atomistic simulations, compared with the predicted 128.6°. Atomistic and theoretical spacing are in very good agreement as well, varying by less than 2 Å for both dislocation sets with respective values of 43.2 Å and 45.1 Å for the $[100]_\theta||[\bar{1}3\bar{1}]_\alpha$ Burgers vector dislocation and 42.7 Å and 43.4 Å for the $\frac{1}{2}[1\bar{1}1]_\alpha$ dislocation.

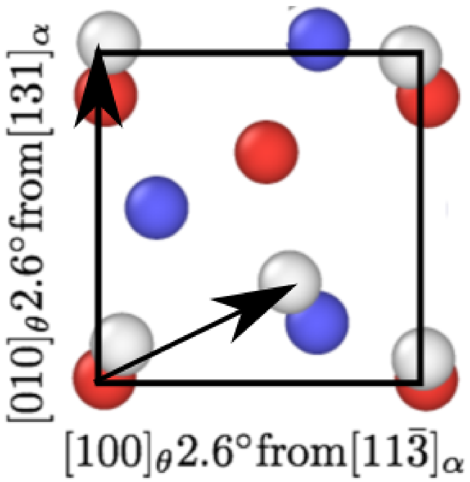

Figure 5.17: Interface coherency and Burgers vectors of the Near Pitsch-Petch OR. The small difference in the orientation relationship results in a change in one of the Burgers vector from $[100]_\theta||\frac{1}{2}[\bar{1}3\bar{1}]_\alpha$ to $\frac{1}{2}[1\bar{1}1]_\alpha$. The interfaces shown consist of ferrite iron (white) and cementite carbon (blue) and iron (red and yellow).

The Near Pitsch-Petch shares the same interfacial chemistries as the previously discussed ORs, with the same trends once again being observed. Both the Tersoff and MEAM potentials predict

Table 5.6: The computed interfacial energy (J/m^2) for the interfacial chemistries of the Near Pitsch-Petch OR.

		FeC-Fe	Fe-FeC	Fe-Fe
Tersoff	Slab	-0.17	0.72	1.53
	CPI	0.40	0.53	0.54
MEAM	Slab	0.58	0.81	0.82
	CPI	0.42	0.44	0.52

this OR to have nearly identical energetics to it parent OR, thus leaving the question of whether the near ORs are more favorable still open. It does appear from atomistic investigation that they are at least as favorable, however.

5.1.6 Isaichev Orientation Relationship

The Isaichev OR [10] is defined as:

$$[010]_\theta || [111]_\alpha$$

$$[101]_\theta || [0\bar{1}1]_\alpha$$

$$(\bar{1}01)_\theta || (2\bar{1}\bar{1})_\alpha$$

This OR is found to have very low lattice mismatch, especially in the $[010]_\theta || [111]_\alpha$ directions, where it is nearly coherent. As the symmetries of the crystal are orthogonal, so too are the dislocation arrays. This structure allows the spacing to be well defined through simple lattice mismatch theory, which predicts spacing of 135.5 Å and 105.5 Å, which compare very well with the values observed by atomistics of 133.5 Å and 104.1 Å.

Table 5.7: The computed interfacial energy (J/m^2) for the interfacial chemistries of the Isaichev OR.

		Fe(8d)-C	Fe(4c)-Fe(4c)	C-Fe(8d)	Fe(4c)-Fe(8d)	Fe(8d)-Fe(4c)
Tersoff	Slab	0.27	1.15	0.31	0.97	2.27
	CPI	0.12	0.33	0.21	0.37	0.67
MEAM	Slab	0.46	0.60	0.55	0.84	1.11
	CPI	0.25	0.38	0.32	0.49	0.86

Due to a different orientation of the cementite as compared to all the other ORs, the Isaichev has a completely different set of chemistries. The Fe(8d)-C is found to be the lowest energy for all approaches and potentials. The Isaichev is found to have the lowest energy of all chemistries and ORs, likely as a result of its near coherency. This is somewhat surprising, as it perhaps the least observed OR. Before any declaration can be made on its status as the most energetically favorable can be made, it is first necessary to perform a more thorough comparison of the ORs.

5.1.7 Comparison Between Orientation Relationships

Structure

For all ORs, dislocation networks were observed to form at the interface between the ferrite and cementite. The line directions of these dislocations is seen to follow O-lattice theory, with line directions lying in the same directions as the O-points. For the Bagaryatskii and Isaichev ORs, in which the interface plane can be defined by two high symmetry, orthogonal crystallographic directions in each crystal, this results in a set of orthogonal dislocations that correspond with these directions. For the "near" ORs, in which there is exact alignment between only one high symmetry direction, $[010]_\theta||[111]_\alpha$ for the near Bagaryatskii and $[010]_\theta||[\bar{1}31]_\alpha$ for the near Pitsch-Petch, it similarly can be observed that one of the dislocation sets lies in these aligned high symmetry directions. The direction of the other dislocation are less intuitive, and seemingly unrelated to high symmetry directions in the crystals. Additionally, the spacings do not follow simple lattice mismatch theory for either dislocation set. The same holds true for the Pitsch-Petch in which there are no perfectly aligned high symmetry directions between the two crystals.

The Frank-Bilby equation (Eq. 2.8) allowed for the determination of theoretical dislocation line directions and spacings for non-orthogonal dislocation sets. For all ORs, the Burgers vectors predicted by O-lattice theory were found to lie within the interface plane and closely correspond, within 0.5 Å, to commonly observed Burgers vector directions and magnitudes in one of the two crystals. These Burgers vectors were generally found to lie in high symmetry directions in the ferrite, favoring the $\langle 111\rangle_\alpha$, which is to be expected as this is the preferred Burgers vector in BCC

Table 5.8: Characterization of the interfacial dislocations for each of the ORs in the pearlite microstructure. The first value given represents dislocation set one and the second dislocation set two, as shown in Figure 5.18. For line direction and dislocation spacing, values in parenthesis represent theoretical continuum model values.

	Bagaryatskii	Near Bagaryatskii	Pitsch-Petch	Near Pitsch-Petch	Isaichev
Burgers Vectors	$[100]_\theta \| \| [1\bar{1}0]_\alpha$ $\frac{1}{2}[111]_\alpha$	$\frac{1}{2}[1\bar{1}1]^*_\alpha$ $\frac{1}{2}[111]_\alpha$	$[010]_\theta \| \| \frac{1}{2}[\bar{1}13]_\alpha$ $[100]_\theta \| \| \frac{1}{2}[\bar{1}3\bar{1}]_\alpha$	$\frac{1}{2}[1\bar{1}1]^*_\alpha$ $[010]_\theta \| \| \frac{1}{2}[\bar{1}13]_\alpha$	$[01\bar{1}]_\theta$ $\frac{1}{2}[111]_\alpha$
Continuum Burgers Magnitude (Å)	4.25 2.51	2.28* 2.51	4.90 4.61	2.31* 4.90	3.98 2.51
Line Direction (°)	0 (0) 90 (90)	90 (90) 143.5 (148.1)	35.7 (37.7) 135.2 (124.2)	0 (0) 118.7 (128.6)	0 (0) 90 (90)
Dislocation Spacing (Å)	42.4 (38.5) 106.1 (105.5)	18.1 (18.8) 52.5 (47.8)	58.5 (61.4) 60.3 (61.8)	43.2 (45.1) 42.7 (43.4)	133.5 (135.5) 104.1 (105.5)

* Actual Burgers vector is the projection of this Burgers vector onto the interface plane.

crystals. When dislocations did not lie in this direction, they were found to be in directions that were high symmetry directions in both crystals. The character of these dislocations are seen to be in excellent agreement with the atomistic results (Table 5.8). Additionally, the Burgers vectors reported here also appear to have the same character as those reported by Kim et al. [101] using AIFB, although they simply reported direction and magnitude, and did not explicitly relate these values to a crystallographic direction. One notable exception to this agreement between the two studies is in the Isaichev OR, in which Kim only reported one dislocation set. This discrepancy appears to be a function of simulation box size though. For the lattice constants of the MEAM potential used in their work, the theoretical dislocation spacing would be approximately 937 Å, much larger than the box sized they used and thus their simulations would likely not develop these dislocations. The use of different lattice parameters is also the reason for the variations in spacings found for the Isaichev in this work and the 50 nm and 25 nm spacings predicted by Zhou et al. [98] using a modified version of Frank-Bilby. However, the agreement in Burgers vector character using two different potentials, whose different lattice constants will result in different line directions and spacings, highlights the robustness of O-lattice theory, and the associated Frank-Bilby equation, in characterizing this system.

The inability of classic O-lattice theory to calculate exact Burgers vector magnitudes however, necessitated the use of the Vattré and Demkowicz approach to better define the system. The dislocation character determined by Frank-Bilby was used in this formulation, in conjunction with the lattice and elastic constants from the potential, and all lattices intermediate to the ferrite and cementite were scanned to minimize the far-field strain. For all ORs, these Frank-Bilby determined Burgers vectors were found to create a zero-strain state, with the exact magnitudes found in Table 5.8. It is worth noting that this approach does have its own limitations, most notably that it cannot account for the effects of interfacial chemistries which have been shown in this work to result in differing interfacial energies. However, as all interfacial chemistries within an OR have the same line directions and spacing, there must be additional structural factors that produce these energy differences.

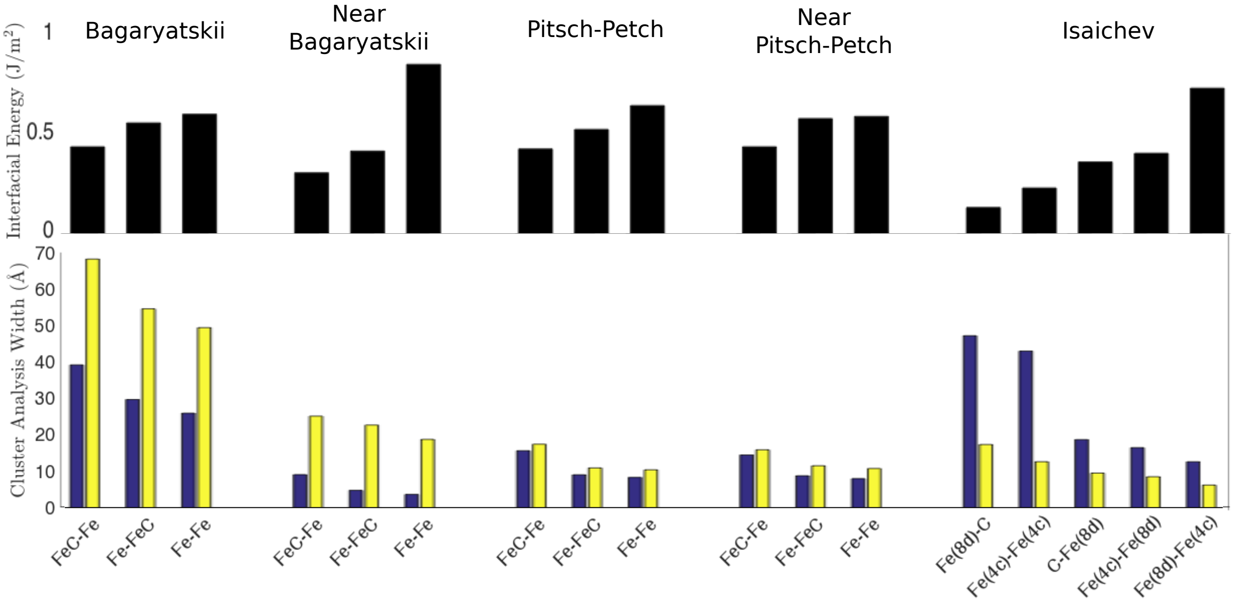

Figure 5.18: Comparison of dislocation width (blue - dislocation set one, yellow - dislocation set two in Table 5.8) using cluster analysis for all interfacial chemistries and ORs and the associated interfacial energies using the CPI approach. Energy is observed to trend opposite that of the dislocation widths, with larger spreading associated with lower energy. For the Isaichev OR, the $[101]_\theta$ Burgers vector direction is found to have the largest width for all chemistries, while for all other ORs the $[010]_\theta$ is largest.

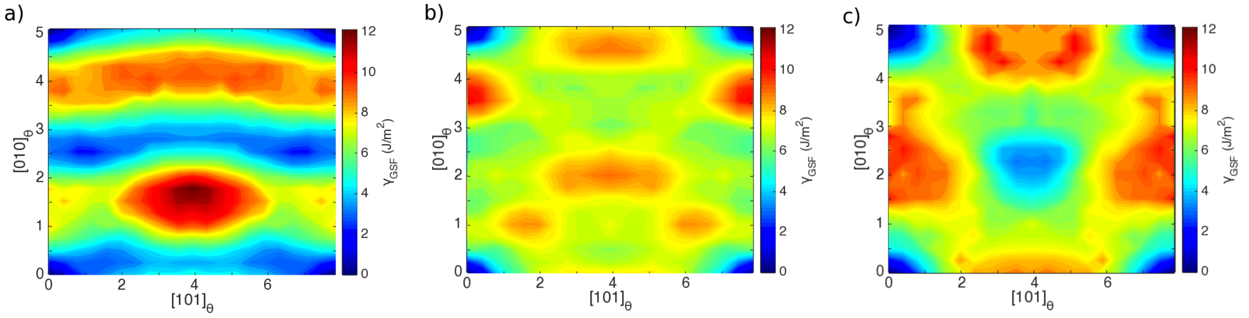

Figure 5.19: Generalized stacking fault energy surfaces in cementite approximating a) the Fe(8d)-C and Fe(4c)-Fe(4c) chemistries, b) the C-Fe(8d), and c) the Fe(4c)-Fe(8d) and Fe(8d)-Fe(4c) interfacial chemistries of the Isaichev OR. For all three surfaces, the $[010]_\theta$ direction in the GSF surfaces is observed to have the higher stacking fault energy, suggesting there will be less core spreading for this Burgers vector direction.

To understand these structural differences, the atomistic results must again be considered. Following the methodology used for the Bagaryatskii OR, cluster analysis was used. While this is a qualitative measurement to be sure, it does allow for the comparison of the dislocations in each interfacial chemistry of an OR. Due to the sensitivity of this approach however, it is not possible to use it to compare the various ORs. In order to construct the periodic simulation box for each OR, small strains must be applied to each lattice ($< 0.25\%$). These small strains, in conjunction with the varying strain fields from the interfacial dislocations themselves, result in slightly different values for nearest neighbor distance in the ferrite lattice, variations that are within the sensitivity of the cluster analysis and require the use of different cutoff radii for the various ORs. Within each OR, it is observed that the width of the dislocations vary both between the interfacial chemistries and between the two dislocation sets within each chemistry (Fig. 5.18). For the Bagaryatskii, the Pitsch-Petch, and their associated near ORs, all of which have the same possible chemistries, a clear trend can be discerned. For both dislocation sets, the FeC-Fe has largest widths, followed by the Fe-FeC, and then the Fe-Fe having the smallest widths. This suggests a clear connection between interfacial chemistry and the “size" of the dislocations. There are also trends between the dislocations sets for each OR. For the Bagaryatskii, the $[100]_\theta||[1\bar{1}0]_\alpha$ Burgers vector direction is always the largest, with the same being true for the $[100]_\theta||[\bar{1}3\bar{1}]_\alpha$ and $[101]_\theta||[01\bar{1}]_\alpha$ Burgers vector directions in the Pitsch-Petch and Isaichev ORs, respectively.

As mentioned during the Bagaryatskii analysis, dislocation core spreading is commonly associated with the Peierls-Nabarro model. The same approach with regards to using GSF curves in cementite to approximate the interface is undertaken for the other ORs. There high coherency between the iron atoms in the cementite and ferrite lattices at the interface for these ORs can be observed in Figure 2.4. As both the Bagaryatskii and the Pitsch-Petch, along with their near ORs, have the same cementite orientation, they can all be approximated using the same set of GSF surfaces (Fig 5.7). It was found that Burgers vectors in the $[100]_\theta$ direction had higher GSF energy values than those in the $[010]_\theta$, and that the GSF values for the interface that best approximated the Fe-FeC and Fe-Fe interfacial chemistries were higher than those for the FeC-Fe. When comparing these GSF curves with the values for dislocation widths found in Figure 5.18, it can be seen that the other ORs also trend with the Peierls-Nabarro model, higher GSF peaks result in less dislocation spreading. Similar analysis was done for the interfacial chemistries of the Isaichev OR (Fig. 5.19), and the same trends were observed, with the lower GSF magnitudes of the $[101]_\theta$ direction for all chemistries resulting in more spreading. Conversely, the Fe(8d)-C and Fe(4c)-Fe(4c) interfacial chemistries result in more dislocation spreading due to the lower GSF peaks in the Burgers vector directions. These trends show that the results from the atomistic simulation can in fact be characterized and explained quite well using continuum concepts.

Table 5.9: Summary of computed interfacial energy (J/m^2) for the interfacial chemistries within each OR using both the slab and CPI methods with the Tersoff interatomic potential.

		FeC-Fe	Fe-FeC	Fe-Fe	-	-
Bagaryatskii	Slab	-0.32	0.55	1.50	-	-
	CPI	0.40	0.51	0.55	-	-
Near Bagaryatski	Slab	-0.21	0.66	1.47	-	-
	CPI	0.28	0.38	0.78	-	-
Pitsch-Petch	Slab	-0.05	0.75	1.53	-	-
	CPI	0.39	0.48	0.59	-	-
Near Pitsch-Petch	Slab	-0.17	0.72	1.53	-	-
	CPI	0.40	0.53	0.54	-	-
		Fe(8d)-C	Fe(4c)-Fe(4c)	C-Fe(8d)	Fe(4c)-Fe(8d)	Fe(8d)-Fe(4c)
Isaichev	Slab	0.27	1.15	0.31	0.97	2.27
	CPI	0.12	0.33	0.21	0.37	0.67

Table 5.10: Summary of computed interfacial energy (J/m^2) for the interfacial chemistries within each OR using both the slab and CPI methods with the MEAM interatomic potential.

		FeC-Fe	Fe-FeC	Fe-Fe	-	-
Bagaryatskii	Slab	0.68	0.76	0.94	-	-
	CPI	0.40	0.45	0.51	-	-
Near Bagaryatski	Slab	0.57	0.81	0.88	-	-
	CPI	0.38	0.42	0.78	-	-
Pitsch-Petch	Slab	0.66	0.90	0.95	-	-
	CPI	0.44	0.54	0.57	-	-
Near Pitsch-Petch	Slab	0.58	0.81	0.82	-	-
	CPI	0.42	0.44	0.52	-	-
		Fe(8d)-C	Fe(4c)-Fe(4c)	C-Fe(8d)	Fe(4c)-Fe(8d)	Fe(8d)-Fe(4c)
Isaichev	Slab	0.46	0.60	0.55	0.84	1.11
	CPI	0.25	0.38	0.32	0.49	0.86

Interfacial Energy

While understanding the structure of the dislocations within each OR is important, in order to determine which is most favorable it is necessary to consider the interfacial energy. Interfacial energy values were calculated for the interfacial chemistries of each OR using both the slab and CPI methods. These two methods are seen to give different results, and therefore before discussing any trends in the energetics, it must first be determined which of these methods is most appropriate. Perhaps the most glaring difference between the two methods is the prediction of negative interfacial energies by the slab method for the lowest energy chemistries of several of the ORs. As stated in the discussion of the CPI approach, negative interfacial energies are extremely unlikely. The CPI approach is further validated by considering the effect of interfacial chemistry on the energetics of the system. As discussed in the previous section, dislocation spacing, line direction, and Burgers vector do not change with interfacial chemistry within each OR. A first-order approximation of the energy of these dislocation scales with b^2, where b is the magnitude of the Burgers vectors. It therefore follows that the energy contribution of the dislocations themselves is roughly the same for all chemistries. Any differences in the interfacial energy must therefore be a function of the atomic alignment and bonding at the interface of the two lattices. As the relative alignment of iron atoms at the interface (Fig. 2.4) is the same for all interfacial chemistries of an OR, it would be expected that variations in chemistry would have only a modest affect on the interfacial energy values. However, it can be seen that the slab methods finds the variation between interfacial energies of an OR to be an order of magnitude larger than the differences predicted by the CPI, suggesting again that the CPI is a more appropriate way to define interfacial energy for this system.

In order to confirm the validity of the CPI approach using non-atomistic methods, the continuum method proposed by Vattré and Demkowicz to predict interfacial energy was used for comparison. From Table 5.11, it can be seen that the continuum model does in fact exhibit the same trends as the CPI, predicting that the near ORs have lower energy than their parent ORs. Additionally, the Isaichev is predicted to be noticeably lower than the other ORs, which is consistent with the CPI approach and drastically different than the slab method, which predicts it to be the highest. The agreement between the atomistic and the continuum interfacial energy values also suggests that on the first-order, lattice mismatch is the dominant factor in determining the interfacial energy. This is reasonable as the interfacial dislocation structure is likely the main contributor to the energy, and was shown be a function of lattice mismatch, as it follows O-lattice theory. In an attempt to create a simple metric to quantify the lattice mismatch, the strain tensors to transform between the two lattices are averaged:

$$\epsilon = \frac{F_{AB}F_{AB}^{T} + F_{BA}F_{BA}^{T}}{2} - I \tag{5.2}$$

where F_{AB} and F_{BA} are the transformation matrices between the two lattices and I is the identity matrix. The L_2 norm of the resultant tensor for each OR was calculated, and these strain values (Table 5.11) were found to trend with the energies of both atomistics using CPI and the continuum model, with the Isaichev having a significantly lower value than the other ORs, all of which have very similar magnitudes. This agreement with continuum concepts further cements the CPI as a more useful tool for the atomistic analysis of this system.

Table 5.11: Continuum interfacial energy [106] values (J/m^2) for the Tersoff and MEAM interatomic potential lattice and elastic constants, as well for experimental values. Numbers in parenthesis give the magnitude of lattice strain mismatch (Eq. 5.2).

	Isaichev	Bagaryatskii	Near Bagaryatskii	Pitsch-Petch	Near Pitsch-Petch
Tersoff	0.68 (0.039)	1.13 (0.097)	0.96 (0.099)	1.08 (0.115)	0.93 (0.109)
MEAM	0.22 (0.023)	0.83 (0.100)	0.66 (0.105)	0.59 (0.110)	0.40 (0.102)
Experimental	0.32 (0.25)	0.79 (0.104)	0.62 (0.101)	0.60 (0.111)	0.41(0.104)

It is worth noting that some of the energy trends presented here do vary from those proposed by Kim et al. [101], particularly with regards to the near ORs. The reason for this is likely twofold: they do not consider the various interfacial chemistries and they use the slab approach. In order to ensure that the observed results were not a function of the Tersoff potential, the energetics were also calculated with the Liyange MEAM potential. When considering all possible chemistries, the potentials are in agreement as to which interface is most favorable: the FeC-Fe for the Bagaryatskii and Pitsch-Petch, and the Fe(8d)-C for the Isaichev. While the general trends between these two interatomic potentials are the same (Tables 5.9 and 5.10), Isaichev has the lowest energy and the near Pitsch-Petch and Pitsch-Petch ORs have roughly the same energy, there is a noticable difference between the two with regards to the Bagaryatskii and near Bagaryatskii. The Tersoff potential predicts a distinct difference between the two, with the near Bagaryatskii being lower, while the MEAM potential finds them to have very similar energies.

In order to determine how much of this variation is from the interatomic potentials, the continuum model is once again utilized. Using the lattice and elastic constants for the potentials as well as experimental values [4, 155, 157], the continuum energetic values were calculated. The trends for the Isaichev, Bagaryatskii, and Pitsch-Petch were all the same as those observed in atomistics, with Isaichev having a distinctly lower energy and the Bagaryatskii and Pitsch-Petch having more similar energetics. The continuum model predict the near ORs to have lower interfacial energy than their parent ORs for all potentials. As the near and parent ORs have similar mismatch strain, this difference likely arises for the lower magnitude Burgers vectors in the near ORs. However, since the the continuum model does not account for larger atomic disregistry that occurs at the interface for the near ORs, it is difficult to definitively determine the exact magnitude of the difference of the energies between near and parent ORs. The near ORs do appear to be at least as energetically favorable as their parents, if not moreso.

While the lattice mismatch, and the resultant Burgers vectors that arise from it, seems to be the dominant factor in determining the interfacial energy, understanding how and why the various chemistries affect the energy is also important. By comparing each interfacial chemistry with its associated interfacial energy value, two main trends can be observed that result in low interfacial energy: keeping 8d or 4c iron pairs (like site pairs) near the interface intact and the presence of carbon. The former can best be observed in the Isaichev OR, where the Fe(8d)-C and Fe(4c)-Fe(4c) interfaces, in which these iron pairs remain intact, have the two lowest interfacial energies. Conversely, in the other chemistries of the Isiachev where these like site iron pairs are separated, the interfacial chemistries are found to have larger energy values. The presence of carbon near the interface also appears to reduce the interfacial energy. For the chemistries of Isaichev OR in which the iron pairs are broken, it can be observed that the energies trend with the distance of the carbon from the interface; the closer the carbon, the lower the interfacial energy. The same is found to be true for the chemistries in which the iron pairs remain intact. The relation of proximity of carbon to the interface and interfacial energy is not absolute however, it only holds true within the intact and broken iron pairs subsets of chemistries, suggesting that the affect of carbon is secondary to that of the iron pairs. The above observations are supported by the energy trends in the Bagaryatskii and Pitsch-Petch ORs. Due to the orientation of the cementite crystal, none of the like site iron pairs are broken, however the same trends with respect to carbon's proximity to the interface can be seen. Additionally, the discrepancy in the spread of interfacial energy values between the chemistries of the Bagaryatskii and Pitsch-Petch ORs and those of the Isaichev further supports the secondary nature of carbon's influence. The difference between the highest and lowest chemistries of the Isaichev OR, where the iron pairs are broken in some chemistries, is more than twice that of the other ORs, where all iron pairs remain intact and the only difference is the position of carbon. The favorability of both the like site iron pairs and the carbon near the interface is likely rooted in the breaking and reforming of bonds at the interface. When the interface plane is created, the preferred bonds of the cementite lattice are broken for the atoms closest to the plane. New bonds with the ferrite atoms are then created, but these are weaker than those in pure cementite, and this increase in energy contributes to the interfacial energy. DFT studies of the cementite structure [4,163], have found there to be a complicated mix of covalent, ionic, and metallic bonding present, making it difficult to precisely quantify these energy differences. It has been suggested though that bonds between iron atoms in the 4c and 8d sites are weaker than those between like sites [164]. This would be consistent with the results in this work, as it would be more energetically favorable to break and reform the weaker bonds than those between atoms in the same site. The influence of carbon can also be explained through this bonding argument. Carbon near the interface would more easily be able to form covalent bonds, which would be stronger and lower energy than purely metallic bonding, and results in a smaller energy increase. The bonding state at the interface will also play a role in the ability of dislocations to spread. From Figure 5.18 it can be observed that interfacial energy trends opposite of the dislocation widths observed by the cluster analysis: chemistries with the largest widths had the lowest interfacial energy. This suggests that the ability of the dislocation to spread results in a lower energy state. As dislocation spreading was shown to correlate with GSF energies, this raises the possibility that by generating GSF surfaces it may be possible to determine which chemistries are more favorable. Thus the aforementioned bonding factors and GSF surfaces both provide insight into the most favorable interfacial chemistry.

5.1.8 Continuum Analysis

The agreement of the continuum formulation with atomistics in the pearlite system raises the possibility of its use to expand the analysis of the system. Two areas are of particular interest, uncertainty quantification and mapping out the energies of these ORs as they change with temperature. Both applications use the ability of this continuum formulation to calculate energetics with variations in lattice and elastic constants. Interatomic potentials are generally constructed to minimize at 0 K to experimentally observed values, though often these experimental values are from tests performed at 300 K. As temperature is introduced and the simulations become dynamic, the observed minimum energy structures begin to vary from those in statics. For simple structures such as the BCC ferrite, this can be made to mirror the effects of temperature observed experimentally, but for more complicated structures, such as the cementite, this is much more difficult. As such, determining what the effect of specifics variations in lattice and elastic constants is difficult with atomistics.

Uncertainty quantification

One area of great interest in the field of computational modeling is uncertainty quantification. As any simulation will never perfectly match experimental conditions, understanding how these variations affect the results is extremely useful. The Vattré continuum model was already utilized in this way to determine how the variations of the lattice and elastic constants between the interatomic potentials, as well as experimental values would change the predicted energy (Table 5.11). It is desirable to further generalize this however, and determine how the variation in each of the lattice constants affect the interfacial energy for each OR. Figure 5.20 shows the change in energy as the cementite lattice constants (a_θ, b_θ, c_θ) and ferrite lattice constant (a_α) are individually varied +/- 5% from experimental values. This variation was chosen as it is larger than the difference between any of the potentials used in this work, as well as larger than the variation that occurs during temperature change.

A few observations can be made from these plots. For the most part, the change in energy with changing cementite lattice constants behaves linearly, which is to be expected as the lattice mismatch, which is the dominant factor in the energetics of the continuum model is increasing at a constant rate. One notable variation from this is the Isaichev, in which the interfacial energy is seen to initially decrease with reduction in the b lattice constant of cementite. Upon reaching approximately 99% of the original lattice constant however, it begins to rise. The change in trend represent the point at which the $[010]_\theta||[111]_\alpha$ become coherent. As the lattice constant approaches this point, mismatch becomes smaller, resulting in reduced interfacial energy, and once it is passed the lattice mismatch increases. The same phenomenon is responsible for the behavior of the ferrite

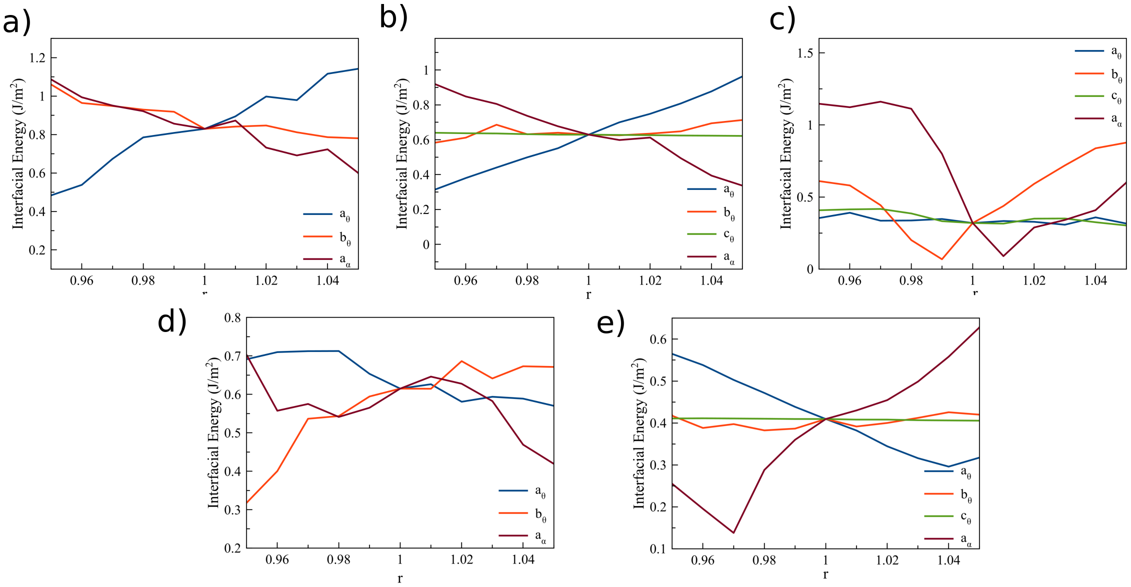

Figure 5.20: Change in interfacial energy as predicted by the continuum model with variation in lattice constants of the a) Bagaryatskii, b) Near Bagaryatskii, c) Isaichev, d) Pitsch-Petch, and e) Near Pitsch-Petch ORs.

lattice constant in the Isaichev. The other observation is the change in a_α undergoes for some ORs does not behave linearly like the cementite. This is particularly true for ORs in which the ferrite is in tension in one direction and compression in the other. When this is the case, changing the lattice parameter results in a reduction in mismatch in one direction and and an increase in the other. This, along with the resultant change in the dislocation spacing, accounts for the observed fluctuations. It is also worth noting that with the exception of the Isaichev, variation of the c lattice parameter in the cementite results in very little energetic change. While the variation in the Isaichev is to be expected as variation in the c lattice parameter will alter the length of the $[101]_\theta$ Burgers vectors, as well as the associated dislocation spacing, it was possible that change in c could also affect the the Near ORs. As these ORs are based on the $(103)_\theta||(110)_\alpha$ symmetry, changes in c could alter the reference lattice. It appears however, that small changes in c have almost no effect on the energetics of these ORs. One final observation on the response to lattice constant variation is with regards to the Near Pitsch-Petch. From Figure 5.20e, it can be seen that there is again non-linear behavior, with minimums occurring at 97% and 104% of the experimental values for a$_\alpha$ and a$_\theta$. Unlike the Isaichev where these minimums were a result of coherency, the Near Pitsch-Petch minimums are a result of a disappearing Burgers vector. From atomistic results and O-lattice theory, one of the Burgers vectors for this OR was the projection of the $\frac{1}{2}[1\bar{1}1]_\alpha$ onto the interface plane. As a$_\alpha$ is decreased or a$_\theta$ is increased, the projection of the $\frac{1}{2}[1\bar{1}1]_\alpha$ becomes progressively smaller, until the observed minimums are reached, at which point it begins to increase again. While lattice mismatch is the dominant factor in the interfacial energy values calculated by this continuum approach, the Burgers vector also contributes to a lesser degree. This can be observed in the differences in interfacial energy change between the Isaichev and Near Pitsch-Petch, with Isaichev energies varying by more than twice as much as the Near Pitsch-Petch. The Near Pitsch-Petch behavior highlights a limitation of extrapolating using the continuum approach, as the O-points near these minimums, where the $\frac{1}{2}[1\bar{1}1]_\alpha$ has a much larger out of interface plane component, may differ from those observed in atomistics. This means that there could potentially be different Burgers vectors in these states. However the differences between experimental values and the interatomic potentials values for both the a$_\alpha$ and a$_\theta$ are on the order of 1%, suggesting that the assumptions made with regards to the Burgers vectors of the Near Pitsch-Petch will still be valid when considering uncertainty of the potentials.

The relations observed in Figure 5.20 also allow for the development of an expression to quantify the predicted change in energy with these variations. The change in interfacial energy with the change in lattice constants can be expressed as:

$$d\gamma = \frac{\partial\gamma}{\partial a_\theta}da_\theta + \frac{\partial\gamma}{\partial b_\theta}db_\theta + \frac{\partial\gamma}{\partial c_\theta}dc_\theta + \frac{\partial\gamma}{\partial a_\alpha}da_\alpha \tag{5.3}$$

If this is related to the change in energy relative to percent variation of the lattice constants, this equation then becomes:

$$d\gamma = \frac{\partial\gamma}{\partial r_{a,\theta}}\frac{da_\theta}{a_{\theta,0}} + \frac{\partial\gamma}{\partial r_{b\theta}}\frac{db_\theta}{b_{\theta,0}} + \frac{\partial\gamma}{\partial r_{c,\theta}}\frac{dc_\theta}{c_{\theta,0}} + \frac{\partial\gamma}{\partial r_{a,\alpha}}\frac{da_\alpha}{a_{\alpha,0}} \tag{5.4}$$

Table 5.12: Parameters for variation in interfacial energy with change in lattice constants to be used in Equation 5.4. * represent the need to take variation from coherency point and use absolute values.

	$\partial/\partial r_{a,\theta}$	$\partial/\partial r_{b,\theta}$	$\partial/\partial r_{c,\theta}$	$\partial/\partial r_{a,\alpha}$
Bagaryatskii	7.23	-2.23	-	-3.38
Near Bagaryatskii	6.21	1.03	-	-5.67
Isaichev	-0.25	15.40*	-0.94	34.08*
Pitsch-Petch	-1.51	1.95		3.42
Near Pitsch-Petch	-2.99	0.72	-	6.12

where the $\frac{\partial \gamma}{\partial r}$ are the slopes of the lines in Figure 5.20 and $a_{\theta,0}$, $b_{\theta,0}$, $c_{\theta,0}$, and $a_{\alpha,0}$ are the experimental values for the lattice constants. The parameters of this expression for each OR can be found in Table 5.12. From these values it can be observed that outside of the Isaichev there is minimal change in interfacial energy with lattice constants, < 0.07 J/m^2 per percent change in lattice constants. The unique state of the Isaichev requires a slight adjustment to the formulation for this OR. Due to the minimums that occur at 99% and 101% for a_θ and a_α, respectively, it is not possible to produce a linear fit of the interfacial energy change about the experimentally observed values. It is therefore more appropriate to measure the variation from the minimums in order to make the method more robust. The contribution to $d\gamma$ from this term will therefore always be positive, and while there are discrepancies between the slopes on each sides of the minimum as observed in Figure 5.20c, the slope of the segment between the experimental values and the minimum is chosen to make this method more accurate for small variations in the lattice constant.

Elastic constants are also an important factor in determining the continuum energetics. It is difficult to create a metric to measure this affect as the constants will contribute in a collective manner. However each elastic constant was varied +/- 10% from experimental values for all ORs. This resulted in only a small change in the energetics. The most variation was found for the $C_{11,\alpha}$, $C_{11,\theta}$, and $C_{22,\alpha}$. This makes intuitive sense as these directions are within in the interface for all ORs, and would therefore affect dislocations stress fields more than other elastic constants. This change was still minor, with a maximum affect on the interfacial energetics of 0.05 J/m^2. This makes the formulation presented in Equation 5.4 an even more valid approximation of the system as lattice mismatch is clearly the dominant factor.

Temperature Effects

Another important factor to account for is how temperature, and the associated changes in lattice and elastic constants, will affect the energetics of the various ORs. This is difficult to do using atomistics, as the lattice and elastic constant variation predicted by the interatomic potentials is oftentimes not the same as the experimentally observed behavior. This provides yet another application for the continuum approach, however before this can be undertaken, it is first necessary to obtain temperature dependent data for all the material constants. The effect of temperature on ferrite [165, 166] is well studied, and have been expressed as follows:

$$
\begin{aligned}
a_\alpha &= 1.602\text{x}10^{-8}T^2 + 2.059\text{x}10^{-5}T + 2.860 \\
C_{11} &= C_{11,0}(1 - 12.779\text{x}10^{-4}(T - 300)) \\
C_{12} &= C - 12, 0(1 - 2.063\text{x}10^{-4}(T - 300)) \\
C_{44} &= C_{44,0}(1 - 1.380\text{x}10^{-4}(T - 300))
\end{aligned}
$$

where a is in Å and $C_{ij,0}$ are the room temperature elastic constants observed experimentally (or the 0 K values from atomistics) and the expressions above are a linear fitting of the data (Fig. 5.21). The temperature dependent lattice and elastic constants are significantly less studied, however experimental values for the lattice constants have been determined experimentally using neutron powder diffraction [167]. There was found to be significantly different trends below and above the Curie temperature of 480 K 5.22, so different fitting parameters were required for the two regimes, with a fifth order polynomial fit used below 480 K, and a second order polynomial fit used above it. The fitting parameters for all three of the cementite lattice constant can be found in Tables 5.13 and 5.14. There is an absence of temperature dependent elastic constant values for cementite, as it is extremely difficult to produce single crystals of the material to test. However, DFT has been used to approximate the temperature dependent elastic constants [168], with quasiharmonic (QH) scaled-volume calculations used to account for effect of thermal expansion and constant-volume calculations at finite temperatures (CVFT) used to account for the effects of phonon-phonon in-

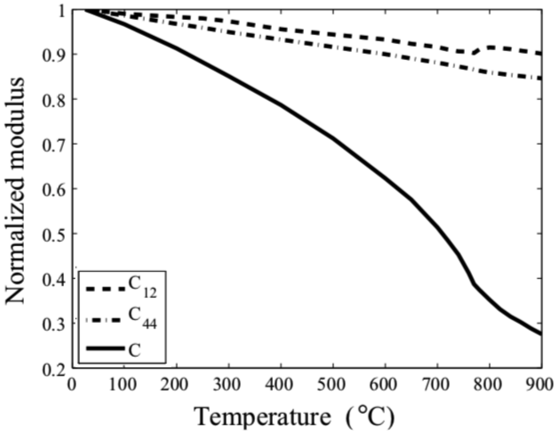

Figure 5.21: Percent change in elastic constants of ferrite with temperature [169], where C=(C_{11}-C_{12})/2. Reproduced from [166]

.

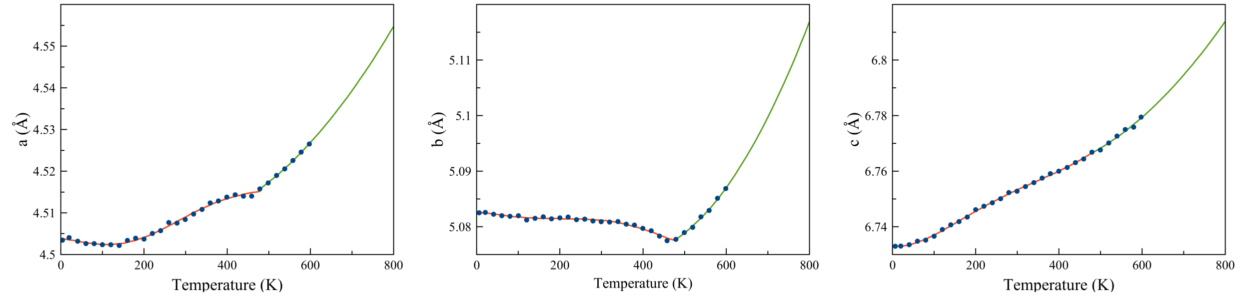

Figure 5.22: Variation of the a, b, and c lattice constants (Å) with temperature as predicted by Wood et al. [167].

teractions (Fig. 5.23). Here, a second order polynomial was used to fit the CVFT calculations for all nine cementite elastic constants, while a linear fit was use for the quasiharmonic calculations. The CVFT and QH components were then summed to determine the elastic constants. As DFT calculations were made only to the Curie temperature, the slope of the curve was determined at 480 K and the elastic constants assumed to continue changing at this constant rate above the Curie temperature.

While the temperature dependent curves for lattice constants for both the ferrite and cementite are given in definite terms, the elastic constant values are given in terms of percent change from $C_{ij,0}$. As such, ferrite elastic constants were expanded about experimental values at 300 K, while

Table 5.13: Constants for fifth order polynomial fit of temperature dependent lattice constant (Å) data of cementite (Fig. 5.22) below the Curie temperature of 480K. ($\alpha_0 + \alpha_1 \times 10^{-6} + \alpha_2 \times 10^{-8} + \alpha_3 \times 10^{-10} + \alpha_4 \times 10^{-12} + \alpha_5 \times 10^{-15}$)

	α_0	α_1	α_2	α_3	α_4	α_5
a	4.504	-5.915	-28.88	27.66	-6.645	5.011
b	5.083	-7.367	-6.420	7.011	-2.060	1.761
c	6.7331	-18.55	82.51	-28.22	3.951	-1.779

Table 5.14: Constants for second order polynomial fit of temperature dependent lattice constant (Å) data of cementite (Fig. 5.22) above the Curie temperature of 480K. ($\beta_0 + \beta_1 \times 10^{-5} + \beta_2 \times 10^{-7}$)

	β_0	β_1	β_2
a	4.5144	-6.814	1.482
b	5.1058	-16.64	2.254
c	6.7740	-11.37	2.045

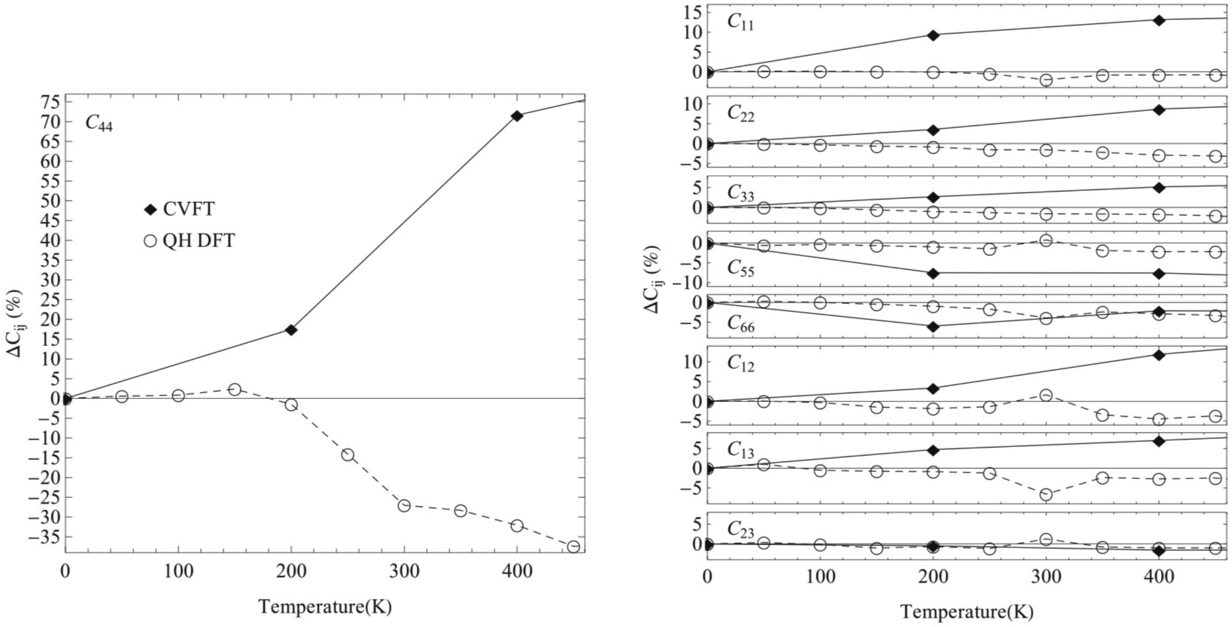

Figure 5.23: Percent change in elastic constants of cementite with temperature predicted by Mauger et al. [168] using the quasiharmonic (QH) and constant-volume finite-temperature approximations (CVFT). Crystal direction were defined as c < a < b. Elastic constants are seen to vary only modestly with temperature with the exception of C_{44}. Reproduced from [168].

the cementite values were expanded about the 0 K DFT values. The continuum method then used these temperature dependent values to determine the interfacial energy for all ORs from 0 to 600 K. From Figure 5.24 it can be seen that there is only a modest increase in the energy with temperature, with the notable exception of the Isaichev OR, which is observed to undergo a significant change in its interfacial energy. This is consistent with what was observed in Figure 5.20, as even small changes in the b_θ and a_α result in large variation in Isaichev energetics. This also suggests that while the Isaichev may be the most favorable at low temperatures, the lattice mismatch is significantly larger at higher temperature and it may therefore become less favorable. It is also worth noting that if only the change in lattice constants are considered and the change in energy approximated using Equation 5.4 about experimental values at 300 K, there is relatively good agreement between the estimated change (Fig. 5.25), and those determined using the full continuum model. The further supports the idea that lattice mismatch is the dominant factor in the energetics, and also raises the possibility of Equation 5.4 being used as a more lightweight model.

5.1.9 Summary

A multiscale approach is taken to analyze interfaces within the pearlite microstructure commonly found in steels. All the possible interfacial chemistries of each OR are constructed, and using atomistics, the energetics and structure of each is determined. This survey finds that when considering the lowest energy chemistries, the Isaichev is the most energetically favorable, with all other ORs having roughly the same energy. However, when the effects of changing lattice and elastic constants with temperature are considered, it is quite possible that the Isaichev is not the most favorable at the temperatures at which it would form. This may explain why it is reported significantly less than the other ORs despite being found to be the lowest energy interface by atomistics using multiple potentials. The proposed near ORs are also analyzed, however the atomistic results do not give a definitive answer on whether the near ORs are better than their parent ORs. The Tersoff potential find them to be more energetically favorable, while the MEAM finds them to be roughly equal. The continuum formulation reports lower energies for the near ORs, suggesting

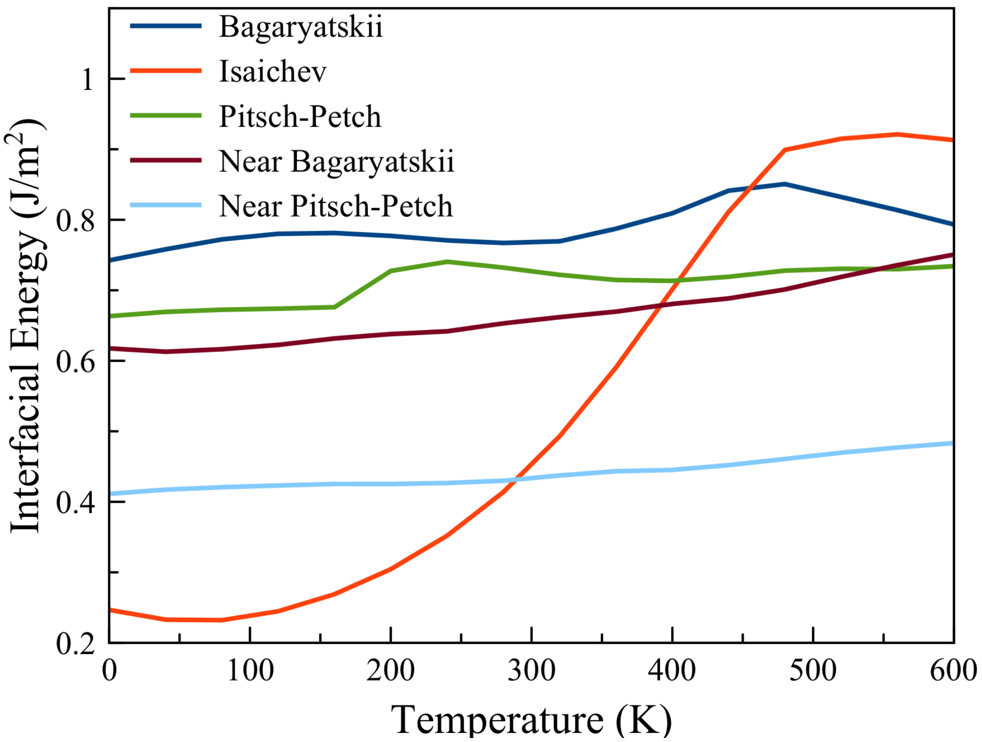

Figure 5.24: Change in interfacial energy with temperature as predicted by the Vattrè continuum formulation.

that the near ORs are at least slightly more favorable than their parents, despite the magnitude of this difference still being unknown. The atomistic and continuum analysis performed in this work address several outstanding question with regards to the structure and energetics of the pearlitic microstructure that would be extremely difficult to examine experimentally and highlight the ability of atomistics to supplement experimental observations.

5.2 Austenite-Cementite Interface

Using the method developed in the study of pearlite, it is also possible to use this approach to further understand the energetics and structure of the austenite-cementite interface.

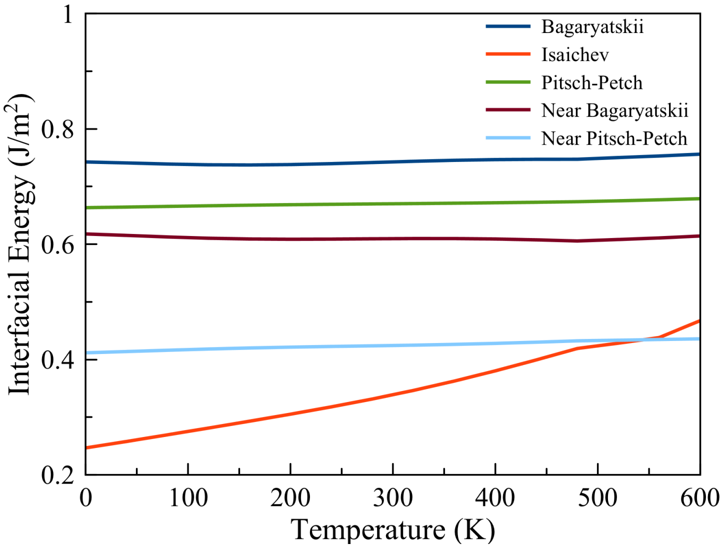

Figure 5.25: Change in interfacial energy with temperature as predicted by Equation 5.4 expanded about 300 K experimental values.

.

5.2.1 The Pitsch Orientation Relationship

As mentioned in Section 2.1.1, there are two commonly reported ORs for the austenite-cementite stystem. The first of these, and most commonly reported is the Pitsch. However, there are disagreements as to what is the habit plane of this OR, and as such there are three proposed formulations for the Pitsch:

Pitsch 1 [19,27]:

$$[010]_\theta || [10\bar{1}]_\gamma$$
$$(\bar{1}03)_\theta || (\bar{1}1\bar{1})_\gamma$$

Pitsch 2 [28]:

$$[010]_\theta || [10\bar{1}]_\gamma$$
$$[\bar{1}01]_\theta || [323]_\gamma$$
$$(101)_\theta || (1\bar{3}1)_\gamma$$

Pitsch 3 [29,30]:

$$[010]_\theta||[10\bar{1}]_\gamma$$

$$(405)_\theta||(1\bar{4}1)_\gamma$$

with γ denoting austenite.

The arguments for each of these formulations can be summarized as follows: the Pitsch 1 works on the assumption that the alignment of the $(\bar{1}03)_\theta$ and $(\bar{1}1\bar{1})_\gamma$ directions will result in the lowest energy, while the Pitsch 2 is based on the concept that the habit plane should have as high of a coherency as possible, which is indeed the case for the $(101)_\theta||(1\bar{3}1)_\gamma$. The Pitsch 3 uses reciprocal space to determine the plane that has the highest alignment with multiple high symmetry directions. While there there are valid arguments to have for all these formulation, there has never been an energetics study on the differences between them to the author's knowledge.

Atomistics is therefore used to calculate the interfacial energy of each. Following a similar procedure as the pearlite annealing, after the initial minimization, the system is given a temperature of 700 K and then ramped down to 5 K over a period of 100 ps using a Nosé-Hoover thermostat and Parrinello-Rahmen barostat. The system is then again minimized at 0 K and zero pressure. Due to the high coherency of the $[010]_\theta||[10\bar{1}]_\gamma$ direction, the simulation was made sufficiently small so as to not allow dislocations to form, as these two lattices are commonly assumed to match perfectly within this interface. While initially it had been hoped that both the Tersoff and the MEAM potentials could be used to study this system, it was found that during minimization the MEAM actually reverted the crystal structure back to BCC, as that is the miniminum energy structure. It was therefore not useful to this study so only the Tersoff was used. Both the CPI and slab approaches were used to calculate the energy for all chemistries of each formulation. The orientation of the cementite in both the Pitsch 1 and Pitsch 2 is the same as that in the Isaichev, and so the same chemistries were used for these. The Pitsch 3 was found to have a disordered interfacial chemistry, and therefore only one chemistry was calculated. Table 5.15 shows the result of this work.

Many of the same trends from the pearlite analysis can be found here. The slab method once agian calculates negative interfacial energies, further cementing the CPI as the proper way to an-

Table 5.15: Calculated interfacial energies (J/m^2) for the various formulation and chemistries of the Pitsch OR using the Tersoff potential

		Fe(8d)-C	Fe(4c)-Fe(4c)	C-Fe(8d)	Fe(4c)-Fe(8d)	Fe(8d)-Fe(4c)
Pitsch 1	CPI	0.30	0.51	0.32	0.44	0.52
	Slab	0.71	-0.12	-0.20	1.45	1.21
Pitsch 2	CPI	0.22	0.54	0.30	0.37	0.52
	Slab	0.82	-0.09	-0.22	1.40	1.26
Pitsch 3	CPI	0.43	-	-	-	-
	Slab	0.86	-	-	-	-

alyze these systems. The Pitsch 2 is found to have the lowest interfacial energy with a calculated value of 0.22 J/m^2. This was with the Fe(8d)-C interfacial chemistry, the same that was found to be lowest for the Isaichev.

5.2.2 Thompson-Howell Orientation Relationship

With the energies of the Pitsch OR documented, it was also necessary to consider the Thompson-Howell OR and its associated possible habit planes. The reasoning behind all of these tracks with the Pitsch, as TH-1 is based on the $(103)_\theta||(\bar{1}1\bar{1})_\gamma$ symmetery, the T-H 2 based on a coherent habit plane, $(10\bar{1})_\theta||(1\bar{3}1)_\gamma$, and the T-H 3 determined using reciprocal space. The formulations are given by:

T-H 1 [27]:

$$[010]_\theta||[10\bar{1}]_\gamma$$
$$(103)_\theta||(\bar{1}1\bar{1})_\gamma$$

T-H 2 [28]:

$$[010]_\theta||[10\bar{1}]_\gamma$$
$$[\bar{1}01]_\theta||[323]_\gamma$$
$$(10\bar{1})_\theta||(1\bar{3}1)_\gamma$$

T-H 3 [29,30]:

$$[010]_\theta||[10\bar{1}]_\gamma$$

Table 5.16: Calculated interfacial energies (J/m^2) for the various formulation and chemistries of the Thompson-Howell OR using the Tersoff potential

		Fe(8d)-C	Fe(4c)-Fe(4c)	C-Fe(8d)	Fe(4c)-Fe(8d)	Fe(8d)-Fe(4c)
T-H 1	CPI	0.33	0.55	0.53	0.32	0.38
	Slab	0.23	0.22	1.20	0.75	0.49
T-H 2	CPI	0.36	0.56	0.50	0.30	0.35
	Slab	0.35	2.21	1.28	0.84	0.49
T-H 3	CPI	0.56	-	-	-	-
	Slab	0.72	-	-	-	-

$$(30\bar{4})_\theta||(1\bar{4}1)_\gamma$$

Table 5.16 shows the energetic predictions for the Thompson-Howell, and the TH-2, based on the coherency of the $(10\bar{1})_\theta||(1\bar{3}1)_\gamma$ habit plane, is found to be the most energetically favorable at 0.30 J/m^2. Due to the symmetry of the cementite crystal structure, the $(10\bar{1})_\theta||(1\bar{3}1)_\gamma$ habit plane results in the same interfacial atomic coherency as the $(101)_\theta||(1\bar{3}1)_\gamma$ in the Pitsch OR, suggesting the favorability of this habit plane for austenite-cementite interfaces. However, the interfacial energies of the Thompson-Howell are larger than that of the Pitsch, suggesting that the Thompson-Howell is in fact less favorable. This is consistent with experimental results as well, as the Pitsch is reported far more often.

There are several other interesting points to be made here as well. The first is that the T-H was found to have a different lowest energy chemistry than the Pitsch. This suggests that the Thompson-Howell and Pitsch are unique ORs. If the secondary symmetries that are the primary difference between the two ORs played no role, it would be expected that the energies of the two would be nearly identical for each chemistry. It can also be observed that for both ORs, the third formulation, in which reciprocal space is used to determine a habit plane that has near alignment of multiple high symmetry directions, is found to have higher energy than the other proposed habit planes. This suggests that while this approach is certainly novel, it is not appropriate for this system.

Structurally the results of the two simulation sets are very similar. Due to the mirror symmetry of the $(10\bar{1})_\theta$, the interfacial structure, and thus the lattice parameters used in Frank-Bilby are the same. As a result, the direction and spacing of the single dislocation set that occurs are the same for both ORs. Only one dislocation set is observed because the $[010]_\theta$ and $[110]_\gamma$ are nearly coherent, with a predicted spacing of over 122 nm using lattice mismatch. Figure 5.26 shows the interfacial structure of the Pitsch and Thompson-Howell ORs. The line direction is found to lie in the $[010]_\theta||[110]_\gamma$ direction, identical to what is predicted by O-lattice theory, with a spacing of 46.1 Å, which is very close to the 46.6 Å predicted by O-lattice theory. The predicted Burgers vector is $\frac{1}{2}[101]_\theta$ in the Pitsch and $\frac{1}{2}[10\bar{1}]_\theta$ for the Thompson-Howell. There is however, no atom within the cementite lattice at this point, only one that also has a small translation in the $[010]_\theta$ direction (Fig. 5.27). This is likely the proper Burgers vector, but O-lattice theory is unable to account for the $[010]_\theta$ translation due to the presence of only one dislocation set. The continuum method was also applied to the system, however due to the identical lattice structure at the interface of the Pitsch and Thompson Howell ORs, it is unable to differentiate between the two. It does find an interfacial energy of 0.48 J/m^2 though. This is larger than the Isaichev and smaller than the other ORs in the cementite-ferrite system, which is consistent with where the atomistic energetics lie.

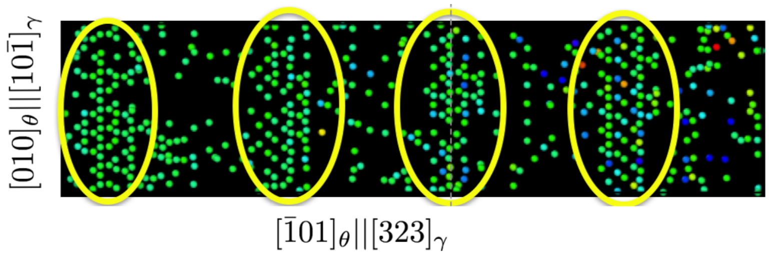

Figure 5.26: Interfacial structure of the Pitsch 2 and T-H 2 habit planes for austenite-cementite interface. Only one dislocation set is observed due to the near coherency of the $[010]_\theta$ and $[110]_\gamma$ directions.

.

5.3 Overview

A comparison of the energetics of the of the austenite-cementite and ferrite-cementite systems can give further insight to the relevant factors in determining the energetics of the system. The

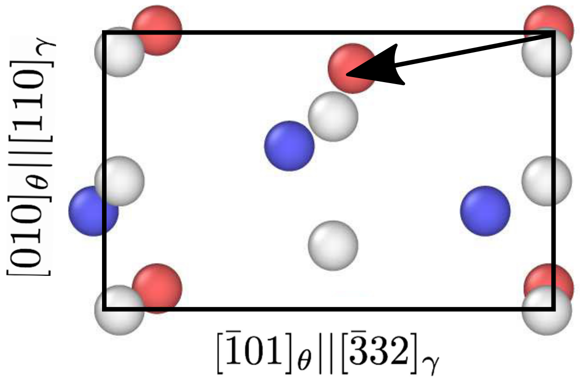

Figure 5.27: Predicted Burgers vector for the Pitsch and Thompson Howell ORs. The projection of this Burgers vector on to the $[101]_\theta$ direction is constant with atomistic results. The interfaces shown consist of austenite iron (white) and cementite carbon (blue) and iron (red and yellow).

.

most notable example focuses on the comparison of the Near ORs with their parent ORs. As the near ORs vary by only a few degrees from their parent, they are roughly analogous to being a different habit plane. For the ferrite-cementite system, this rotation from a habit plane with high atomic coherency to align high symmetry directions resulted either lower or equivalent energies. Conversely, in the austenite rotation from the $\{101\}_\theta||\{131\}_\gamma$ family of planes results in higher energies. The difference in these behaviors lies in whether the rotation alters the symmetries within the interface plane. For the ferrite-cementite system this is indeed the case, and different interfacial dislocation structures arise, which from a continuum perspective are found to be more favorable. In the austenite-cementite system the variations in habit plane within each of the two ORs only causes a slight change in dislocation spacing, with the Burgers vectors and line directions remaining the same. As such, there is little to no energetic gain from the operation, and the coherency of the interface is being reduced. The further supports the proposition that the lattice mismatch is the first order effect on the energetics of the system. The variation between the Pitsch and Thompson-Howell ORs does however show that the alignment of high symmetry directions out of the the habit plane does play a role though. If it didn't, these ORs would have identical energetics. The influence of these symmetries on the energetics appears to be on the same order as interfacial chemistry however, and the energetic effect of the alignment are insufficient to overcome a large drop in interface atomic coherency.

As atomistic analysis of both the ferrite-cementite and austenite systems show that the interfacial structure can be well defined through classic O-lattice theory, this raises the possibility of predicting both energetics and structure through continuum approaches. It may be possible to survey potentially favorable orientations using the continuum approach discussed in this work, and then performing atomistic analysis on systems that are found to be favorable. As more robust relations between lattice mismatch and the energetics are developed, there is also the possibility of these being implemented into mesoscale models, allowing for more accurate production models of these materials. Additionally, the deeper understanding of these iron-iron carbide systems should allow for improved models with regards to the formation of these structures, which will further aid in improving and targeting production of these microstructures found within steel.

Chapter 6

Mechanical Response

Following a similar approach as the structure and energetics analysis of the pearlitic system, the methodology for testing mechanical response was also developed and tested on the Bagaryatskii OR, and specifically the FeC-Fe interfacial chemistry. Simulations were identical in orientation and size as those constructed for the energetic analysis (Table 5.3), with the the exception of being made to periodic in the direction normal to the interface as well, thus simulating the lamellar structure of pearlite. Following the simulated annealing procedure, these unrelaxed structures first underwent a molecular statics energy minimization at 0 K and zero pressure using the conjugate gradient method and a Parrinello-Rahmen barostat. After the initial minimization, the system was given a temperature of 700 K and then ramped down to 5 K over a period of 100 ps using a Nosé-Hoover thermostat and Parrinello-Rahmen barostat, thus reproducing the interfacial dislocations that were observed during the energetic analysis of the system. The system was then equilibrated at 5 K and zero stress for 20 ps. Simulations were performed at this low temperature in order to minimize thermal noise when attempting to characterize the deformation mechanisms. This is a common approach for this type of simulation [43,170]. After equilibration, the simulations are then strained at a rate of 10^9, or 0.01$\%$ per timestep, using non-equilibrium molecular dynamics with a modified Nosé-Hoover thermostat. This approach adjusts the atomic velocities to account for the changing shape and size of the simulation cell using the SLLOD algorithm [171]. It has been shown to be produce the correct velocity gradients and proper values for work performed by stress [172]. There are however, inherit difficulties that come with using atomistics to model mechanical response. In order conduct the simulation in a reasonable amount of computational time, the strain rates used here are orders of magnitude higher than in experiments, so care must be taken to ensure that results are not an effect of this strain rate. As such, several test simulations were also run at lower strain rates, and while some smaller scale events are missed by the strain rates used here, the general behavioral trends to be analyzed here were seen be consistent. The simulations were strained to

30%, which was found to be sufficient to observe all relevant deformation mechanisms, and all work presented here were done using the Tersoff interatomic potential.

Following the methodology discussed in Section 2.3.3, the bulk stress state of the system was determined using the standard virial formulation, while the individual stress states of both the ferrite and cementite were determined by summing the per-atom virial of all atoms of each type and dividing by the total volume of the atoms in the phase as calculated by Voronoi tesselation. These component stress-strain relations were observed to be iso-stress when normal to the interface and iso-strain in the in-plane directions, which is consistent with composite theory. As the formation of dislocations was observed in both the ferrite and cementite, it was also necessary to use dislocation characterization techniques. Due to the common and well studied BCC character of the ferrite, these dislocations were analyzed using the dislocation extraction algorithm, or DXA [173], that has been implemented into the OVITO [159] visualization program. In this approach, common neighbor analysis [174] (CNA) is used to determine atoms in the bulk crystallographic structure. The CNA algorithm takes all neighbors within a cutoff radius of an atom and determines three values for each pair: the number of common neighbors of the two atoms, the number of pairs within these common neighbors, and the longest chain of atoms formed. These values are then matched to the known, theoretical values of common crystal structures (FCC, BCC, HCP). A Burgers circuit is then generated on the atoms not in the selected crystallographic structure (BCC for ferrite), and a Burgers vector is determined. Additionally, as DXA only requires the current state of the simulation, it is able to account for a significant amount of deformation in the crystal. The cementite crystal structure has not been implemented into DXA however, so an alternate approach was required. Atomic slip vector analysis [175] is used here, with the slip vectors (s) defined by:

$$s^{\alpha} = -\frac{1}{n_s}\sum_{\alpha \neq \beta}^{n}(x^{\alpha\beta} - X^{\alpha\beta}) \tag{6.1}$$

where n_s is the number of slipped vectors and $x^{\alpha\beta}$ and $X^{\alpha\beta}$ are the spatial vectors between atoms α and β in the current and reference states, respectively. These slip vectors were visualized using the Atomviewer [176] program. Unlike DXA, the calculation of slip vectors requires both the current state and a reference state. As the nucleation of dislocations in cementite was seen to occur in strains as high as 15%, there was significant deformation of the crystal. This results in some ambiguity in the determination of the exact Burgers vectors, however the direction and magnitude do allow for the determination of the general character. In order to produce clear images of slip planes, the atomic strain metric [177] within OVITO was also used to create the figures seen in this chapter unless otherwise noted. This metric was only used for visualization however, not to inform any of the values presented in this work.

6.1 Bagayatskii Orientation Relationship

Strain controlled tensile and compressive deformation of the simulation cells was undertaken in the $[100]_\theta||[1\bar{1}0]_\alpha$, $[010]_\theta||[111]_\alpha$, and $[001]_\theta||[11\bar{2}]_\alpha$ crystallographic directions. For the sake clarity and brevity, going forward these directions will be referred to using the deformation direction of the cementite. While much of the focus here is on the approximate 7:1 ratio of ferrite to cementite that occurs during the eutectoid transformation from austenite [83], additional ratios, as well as various lamella thicknesses at these ratios, are also considered. It has been proposed for other ferrite-cementite systems that reducing the 7:1 ratio and increasing the volume fraction of cementite can reduce the magnitude of the yield point drop [132]. Using advanced processing techniques, such as nitrocarburizing [133], it is already possible to increase the cementite volume fraction, making the quantification of the mechanical response over a range of values all the more important.

In addition to deforming the pearlitic microstructure, simulations using the same procedure discussed were also performed for both the ferrite and cementite individually. This allows for the relation of the component properties to those of the system. Elastic moduli in the relevant crystallographic directions can be found in Table 6.1.

Table 6.1: Elastic Moduli (GPa) for ferrite and cementite in the relevant crystallographic directions.

	$[100]_\theta \vert\vert [1\bar{1}0]_\alpha$	$[010]_\theta \vert\vert [111]_\alpha$	$(001)_\theta \vert\vert (11\bar{2})_\alpha$
Cementite	149.3	166.2	201.0
Ferrite	260.1	300.9	306.7

Figure 6.1 shows the mechanical response for the 7:1 ferrite to cementite ratio with a cementite lamella thickness of 4 nm. It can be observed for all simulations that three main events can be sequentially observed: 1) elastic deformation, 2) ferrite plasticity, and 3) cementite plasticity. The specifics of these deformation mechanisms will be discussed in the subsequent sections.

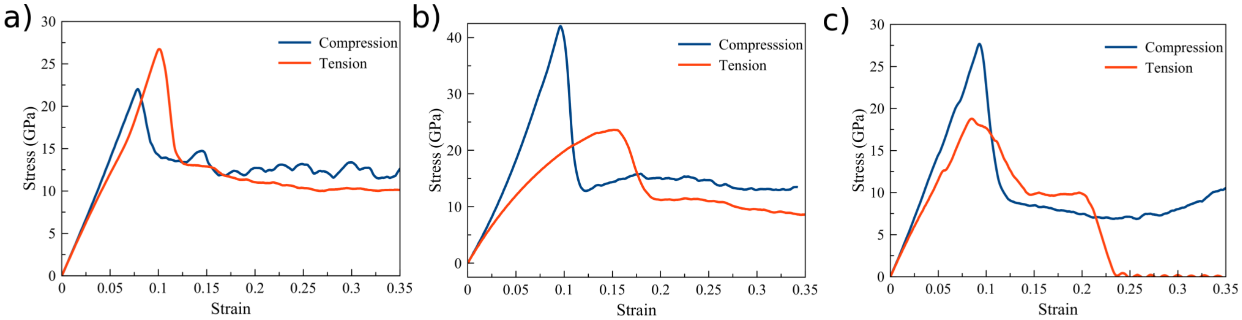

Figure 6.1: Stress-strain response of the entire pearlite structure in compression (blue) and tension (red) for deformation in the a)$[100]_\theta||[1\bar{1}0]_\alpha$ direction, b) $[010]_\theta||[111]_\alpha$ direction, c) $(001)_\theta||(11\bar{2})_\alpha$ direction for a 7:1 ferrite to cementite ratio with cementite lamella thickness of 4 nm.

6.1.1 Transverse Loading

Elastic Deformation

Due to the lamellar structure of cementite, it is possible to make a first order approximation of its behavior using simple composite theory. For a transverse (in-plane) straining, an iso-strain state exists in the direction of loading. In such a strain state, the effective elastic moduli of the system can be related to the component moduli simply using volume ratios:

$$E_{\text{eff}} = \frac{E_\theta V_\theta}{V} + \frac{E_\alpha V_\alpha}{V}$$

This formulation suggests that at a given ferrite to cementite ratio, the effective elastic moduli will remain constant regardless of lamella thickness. It can be observed from Figure 6.2 that this is not the case for the simulations performed, the effective moduli is seen to decrease with decreasing lamella thickness. This suggests there is a size effect to the effective elastic moduli. It has been commonly reported in literature that at the nanoscale the stress state is often influenced by the size of the crystal [178, 179], with the common approximation:

$$\sigma = \sigma_0 + \frac{C}{t}$$

where σ_0 represents the elastic-plastic stress state and the second term the size effects. C is a material constant and t is the thickness. A similar approximation is made for the elastic modulus. Accounting for the both the ferrite and cementite having common interfacial dimensions, the elastic relations can be expressed as:

$$E_{eff} = E_\theta r + E_\alpha (1 - r) + \frac{C}{t} \tag{6.2}$$

where r is the volume ratio of the cementite and t is the thickness of the bi-layer. The effective moduli were determined from simulations for ferrite to cementite ratios ranging from 1:1 to 7:1 and cementite lamella thicknesses ranging from 2 nm to 8 nm. Using the moduli for ferrite and cementite in the appropriate direction found in Table 6.1, C was calculated by minimizing the resultant error between calculated and predicted values. Excellent agreement was found between the analytical model formulation and the simulations, as the values predicted by Equation 6.2 were all within 10% of the values found in atomistics. The C constants were determined to be 2316 GPa·Å in the $[100]_\theta$ direction and 909 GPa·Å for the $[010]_\theta$. These values reflect the contribution of the interface, and the stress field it produces, to the effective modulus of the system with the positive values suggesting stiffening. This results in a much more robust method to determining the effective elastic modulus than attempting to calculate an interfacial stiffness and interfacial thickness.

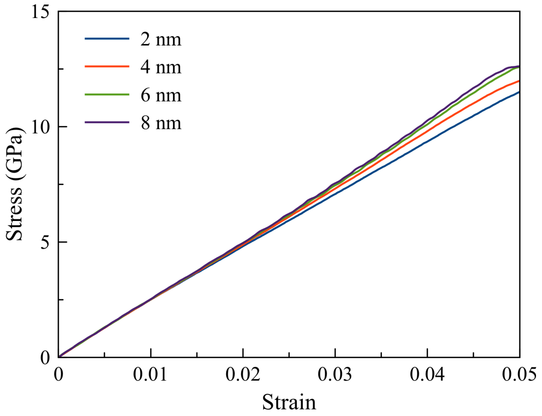

Figure 6.2: Variation of effective elastic moduli for the entire pearlite structure at a 1:1 ferrite to cementite ratio under $[001]_\theta$ tensile straining. Lamella thicknesses of 2 nm (blue), 4 nm (red), 6 nm (green) and 8 nm (purple). Variation of the effective moduli implies a size effect for the elastic modulus.

Ferrite Plasticity

The ferrite was found to plastically deform first in all simulations, regardless of ferrite to cementite ratio or lamella thickness. Upon reaching yield, dislocations loops nucleate at the interface (Fig. 6.3), specifically from regions of intersection between the interfacial dislocations, and into the ferrite matrix. The activated slip system was found to be that which had the highest Schmid factor, which was generally the $\frac{a}{2}\langle 111\rangle\{110\}_\alpha$, but under some loadings, the $\frac{a}{2}\langle 111\rangle\{112\}_\alpha$ system was activated instead. Intersection points between the interfacial dislocations are likely to have the highest local stress state, and are therefore generally the most favorable nucleation site. After the nucleation events, the stress drops to the flow stress (Table 6.2) as the initial nucleation stress is higher than that required for continued plastic flow. The resultant flow stress does vary with loading, but it is independent of the ferrite lamella thickness (Fig. 6.4). It is worth noting that while the flow stress of the ferrite does not vary with the lamellar thickness, the stress state of the whole system will still be a volume average of the stresses in the ferrite and cementite. Thus the reduction

Table 6.2: Slip systems and the resolved shear stresses (GPa) for yield (τ_y^{RSS}) and plastic flow (τ_f^{RSS}) in ferrite and cementite for various transverse loading states of the Bagaryatskii OR. Values in parenthesis represent the Schmid factor for for the slip system.

		$[100]_\theta$		$[010]_\theta$	
		Tension	Compression	Tension	Compression
Slip System	Ferrite	$[\bar{1}1\bar{1}](\bar{1}01)$ (0.408)	$[\bar{1}11](01\bar{1})$ (0.408)	$[11\bar{1}](112)$ (0.314)	$[11\bar{1}](112)$ (0.314)
	Cementite	$[111](\bar{1}10)$ (0.359)	$[111](\bar{1}10)$ (0.359)	$[11\bar{1}](011)$ (0.427)	$[11\bar{1}](\bar{1}10)$ (0.359)
τ_y^{RSS}	Ferrite	9.71	7.50	7.87	12.82
	Cementite	8.22	10.54	10.88	13.33
τ_f^{RSS}	Ferrite	3.87	4.80	2.80	3.84
	Cementite	6.89	5.71	3.63	9.13

in the bulk stress of the system from the nucleation of dislocations in the ferrite will increase with an increasing ferrite to cementite ratio.

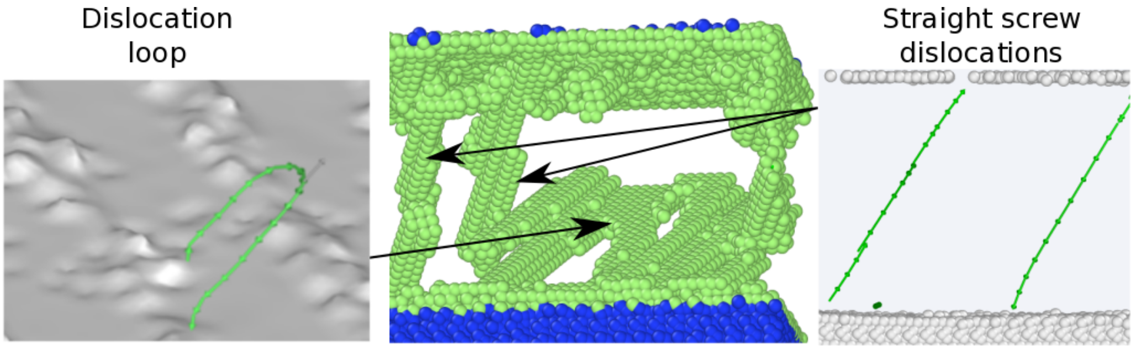

Figure 6.3: Formation of $\frac{a}{2}\langle 111\rangle\{110\}_\alpha$ type dislocations in the ferrite matrix, visualized both by removing all BCC atoms as determined by CNA as well through the use of DXA. Both dislocation loops and straight screw dislocations can be observed within the ferrite.

Cementite Plasticity

Since transverse loading results in an iso-strain state, the ferrite and cementite generally behave independently of each other. After the ferrite yields, it continues to plastically flow while cementite continues to elastically load prior to yield. Similar to the ferrite, this occurs at significantly lower stress than bulk cementite. The amount of accumulated plastic strain does not vary with lamella thickness or ratio, since in an iso-strain state the stress in the individual lamella is independent of these factors. Like the ferrite, once yield in the cementite occurs, dislocations will again nucleate from the interface, however these dislocations do not solely nucleate from the interfacial dislocations. This variation in nucleation sites is likely due to the change in the interfacial dislocation structure after the ferrite plasticity events; there is no longer a pristine interface and the interfacial dislocations will have been disrupted or destroyed. Due to the more complex crystal structure of cementite, the slip planes vary with loading state as well, however for all loadings of the Bagaryatskii they were found to belong to the $\{110\}$ family. This is consistent with the slip planes of cementite reported in literature [180]. The favorability of the slip planes seems to be related to its alignment with the ferrite slip planes of which are already undergoing plastic flow, and this combination of planes in the ferrite and cementite has been suggested as a potential slip transfer system [131]. This concept of slip transfer is particularly relevant to the $[010]_\theta$ tensile loading state, in which the $[11\bar{1}](112)_\alpha$ and $[11\bar{1}](011)_\theta$ slip planes are found to vary by less than 2° (Fig. 6.6). The alignment of slip planes allows for plastic flow of the system at the lower flow stress of the two slip systems, and as such during this loading the cementite can be observed to have a much lower flow stress than during the other loading states (Table 6.2). It is worth noting that different slip systems activate in the cementite during $[010]_\theta$ loading for compression and tension. This suggests that the critical resolved shear stresses for the slip systems of cementite vary with the direction of loading, which is unsurprising as ceramics are known to have different tensile and compressive response. Like ferrite, dislocations form until the plastic flow stress of cementite is reached, and the specific flow stress is independent of lamella thickness (Fig. 6.5). For the loading states in which the slip planes were not aligned, flow stresses are higher than those of bulk cementite, suggesting the interface plays a role in limiting plastic flow. After reaching the plastic flow stress, the entire system will then continue to deform plastically.

6.1.2 Longitudinal Loading

Whereas in transverse loading, the iso-strain state results in unique stress response within both the ferrite and cementite, the longitudinal loading state provides a much more coupled response. As such, the mechanical response will be presented as simply elastic deformation and plasticity, as opposed to discussing the individual behavior of both the ferrite and the cementite.

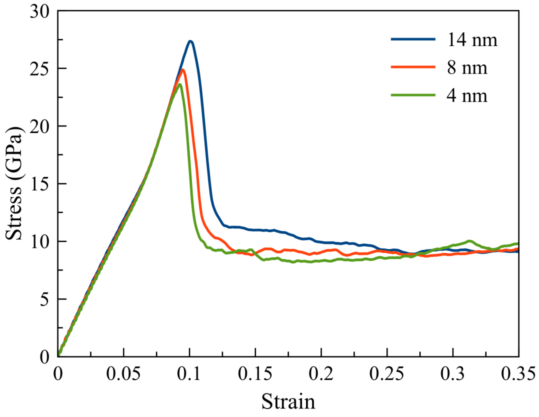

Figure 6.4: Stress-strain response for the ferrite component of the pearlite under $[100]_\theta$ tensile loading for lamella thicknesses of 14 nm (blue), 8 nm (red) and 4 nm (green) with a constant associated ferrite thickness (2 nm). All lamella thicknesses are observed to converge to the same flow stress for both different ferrite to cementite ratios and lamella size.

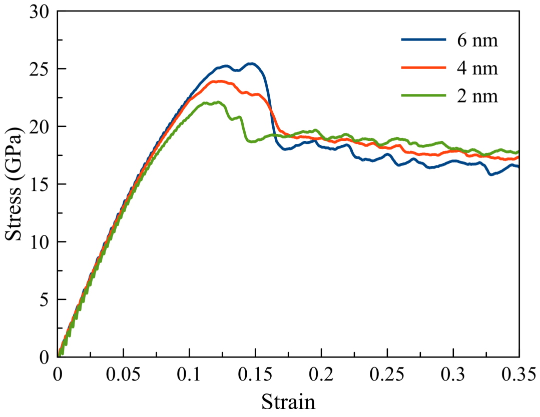

Figure 6.5: Stress-strain response for the cementite component of the pearlite with a 1:1 ferrite to cementite ratio under $[100]_\theta$ tensile loading for lamella thicknesses of 6 nm (blue), 4 nm (red) and 2 nm (green) for ferrite to cementite ratios of 7:1, 2:1, and 1:1, respectively. All lamella thicknesses are observed to converge to the same flow stress regardless of ferrite to cementite ratios or lamella size.

Elastic Deformation

Similar to the approach used in the transverse elastic deformation, simple composite theory is again considered. For longitudinal loading, the effective compliance of the system is the sum of the volume ratios of the component compliances:

$$\frac{1}{E_{eff}} = \frac{V_\theta}{VE_\theta} + \frac{V_\alpha}{VE_\alpha}$$

Combining this equation with a size effect term yields the expression:

$$E_{eff} = \frac{1}{\frac{r}{E_\theta} + \frac{1-r}{E_\alpha}} + \frac{C}{t} \tag{6.3}$$

Fitting simulation results to this equation yields a C value of -338 GPa·, smaller in absolute terms than those from the transverse simulations (Table 6.3). This suggests the interface plays a smaller role in the elastic response, while the negative value suggests softening from the interface.

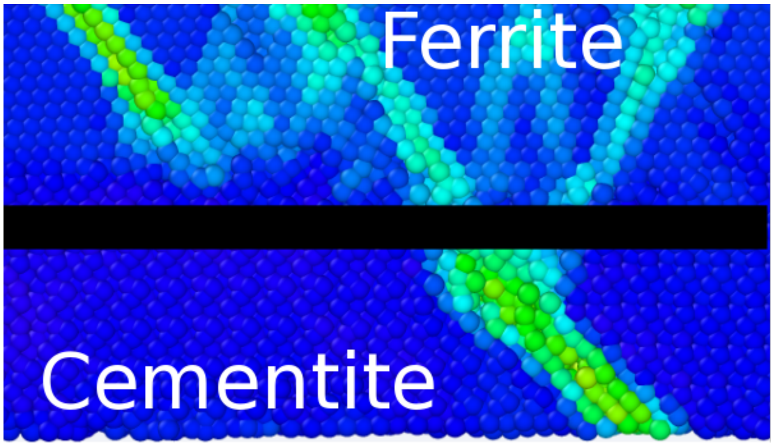

Figure 6.6: Alignment of the $[11\bar{1}](112)_\alpha$ and $[11\bar{1}](011)_\theta$ planes on which slip occurs during tensile $[010]_\theta$ and compressive $[001]_\theta$ loading of the Bagaryatskii OR. The alignment of these activated slip planes allows the cementite to plastically flow at lower stresses than is observed in other loading states.

While Equation 6.3 fully describes the elastic response in compression, there is an additional event that occurs during the longitudinal tensile simulations. From Figure 6.7 it can be observed that there is a stress drop at approximately 5% strain for simulations of all ratios. The magnitude of this stress drop decreases, however, as the ferrite to cementite ratio is increased. Simulations were performed in which the strains were reduced back to zero after this stress drop, revealing that this is a plastic event. Closer inspection of the atomic displacements reveals atomic movement along the core of the $[010]_\theta||[111]_\alpha$ (line direction) dislocations. This suggests plastic flow is occurring within the interface. It is worth noting that for the 7:1 ferrite to cementite ratio the resultant stress drop is very small, and would likely be imperceivable during macroscopic analysis.

Table 6.3: Calculated values of C (GPa·Å) (Eqs. 6.2 and 6.3) for the Bagaryatskii OR. This term accounts for size effects on the elastic response for the various loading states.

$[100]_\theta$	$[010]_\theta$	$[001]_\theta$
2316	909	-338

Plasticity

Much like the transverse loading states, plasticity in longitudinal loading begins with the nucleation of dislocations from the interfacial dislocations. However, due to the iso-stress state of the

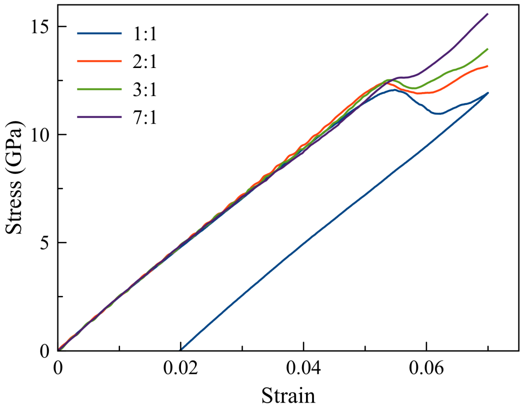

Figure 6.7: Tensile, longitudinal straining of pearlite with cementite lamellar thickness of 4 nm. Ferrite to cementite ratios of 7:1 (purple), 3:1 (green), 2:1 (red), and 1:1 (blue) all reveal a stress drop during straining, with the magnitude of the drop decreasing at higher ferrite to cementite ratios. The 1:1 ratio is also unloaded, revealing that this is a plasticity event resulting from plastic flow in the interfacial dislocations.

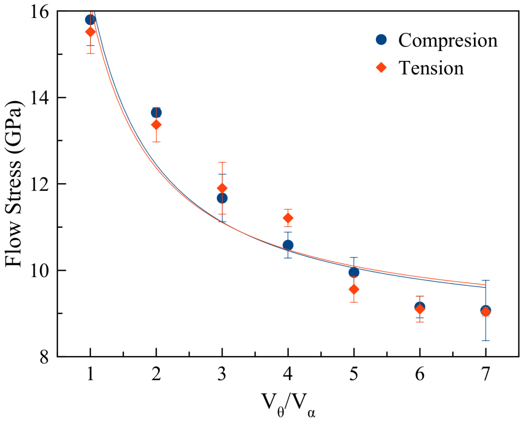

Figure 6.8: Flow stress vs volume ratio plot for $[001]_\theta$ tension (red) and compression (blue) and the associated fit to Equation 6.4). The nearly identical curves suggest that the response is independent of direction of straining and solely a function of volume ratio. Stress oscillates around the flow stess value, shown by the error bars.

system, the mechanical response is quite different. A simple one dimensional model would predict that the system would both yield and plastically flow at the ferrite flow stress, as all further straining would be accommodated by the ferrite. The flow stress of the system would therefore remain constant regardless of the ferrite to cementite ratio. The results of the tensile longitudinal loading, however, show that the resultant flow stress varies with the ratio (Fig. 6.8), with larger ratios observed to have a lower flow stress. This ratio dependent response can be explained by considering the compatibility within the interfacial plane, which was discussed in detail in Section 2.5. Once the ferrite begins to yield, the higher stiffness of the cementite acts a limiting factor to how much the ferrite can contract, and thus limits how much of the strain it will carry. This relation can be shown to follow:

$$\sigma_{\text{flow}} = \sigma_1 + K_1 \frac{V_\theta}{V_\alpha} \tag{6.4}$$

where V_θ and V_α are the volumes of the cementite and ferrite, respectively, and σ_1 and K_1 are material and orientation dependent constants. Simulation results are fit to this equation (Fig. 6.8), and the resultant constants can be found in Table 6.4. The value for σ_1 should be near the flow stress of bulk ferrite since as V_α approaches infinity, $\sigma_{\text{flow}} = \sigma_1$. These values are observed to be fairly close with $\sigma_1 = 8.58$ GPa and the flow stress of bulk ferrite being 9.22 GPa. The constraint of the cementite also affects the yield stress, providing additional stress to that of the applied stress, $\sigma_y = \sigma_{\text{app}} + \sigma_{\text{const}}$, and resulting in a similar relation for yield stress:

$$\sigma_y = \sigma_0 - K_0 \frac{V_\theta}{V_\alpha} \tag{6.5}$$

with σ_0 and K_0 being material and orientation dependent constants. The ductility of the system is a function of the yield stress, the flow stress, and the effective elastic modulus. As these are all volume ratio dependent quantities, it too can be expressed in a similar form:

$$\epsilon_p = \epsilon_0 - K_2 \frac{V_\theta}{V_\alpha} \tag{6.6}$$

The ductility reported here is evaluated as the strain if the simulation were elastically unloaded just prior to cementite plasticity. Equations 6.5 and 6.6 are fit to simulation results (Figs. 6.9 and 6.10) and the resultant constants are shown in Table 6.4.

Table 6.4: Calculated constants for the volume ratio dependent flow stress, yield stress, and ductility (Eqs. 6.4, 6.5, and 6.6) of the Bagaryatskii OR during longitudinal loading. Values were determined using a least squares fit of simulation data.

$\sigma_{0,t}$	$\sigma_{0,c}$	$K_{0,t}$	$K_{0,c}$	σ_1	K_1	ϵ_0	K_2
19.15 GPa	28.06 GPa	2.29 GPa	3.32 GPa	8.58 GPa	7.57 GPa	19.15%	2.29%

For tensile longitudinal loading, the $\frac{a}{2}[\bar{1}11](110)_\alpha$ slip system, which has a Schmid factor of 0.408, activates first. After plasticity begins in the ferrite, the system deforms in an elasto-plastic state at the volume ratio dependent flow stress until the cementite yields. There are two potential processes by which this could occur, either the plasticity mechanisms in the ferrite will be exhausted and the system will then continue deform elastically until the cementite yields, or the cementite will yield before the plasticity events are exhausted. The exhaustion of plasticity mechanisms in the ferrite would have a size dependence as, assuming a constant maximum allowable dislocation density, larger ferrite lamella would be able to accommodate more strain. The latter would be independent of size, as the stress state in the cementite is a function of only the ferrite to cementite ratio. Simulations reveal that there is no size dependence to the ductility of the system, results that are consistent with the findings of Modi et al. [110]. Simulation results also show that the cementite yield stress has the opposite trend of that of the ferrite; increasing the ferrite volume ratio results in lower yield. This is still consistent with Equation 6.5, as the constraints would produce opposite stress states in the ferrite and cementite. The cementite is found to slip within the $[111](10\bar{1})_\theta$ system, which has a Schmid factor of 0.393. The $(10\bar{1})_\theta$ plane in the cementite is found to vary from the $(110)_\alpha$ plane in the ferrite by less than 3°, explaining why the $[111](10\bar{1})_\theta$ slip was activated despite there being other slip systems in the cementite with slightly higher Schmid factors. Once slip occurs in the cementite, the system is seen to fail in short order through the process of delamination at the ferrite-cementite interface.

In compressive longitudinal loading, as the volume ratio of ferrite is increased, the compressive yield stress increases and the flow stress decreases. While it may seem counterintuitive that the same trends occur in both tension and compression, this is consistent with interface compatibility. As the sign of the applied stress is changed, so will the sign of the constraint stresses. As a result, in absolute terms, the interfacial constraints will affect the mechanical response the same in both tension and compression. There are differences in the activated slip systems between tension and compression that warrant further discussion however. The most notable is difference in the activated ferrite slip system, as in compression it is the $\frac{a}{2}[11\bar{1}](112)_\alpha$ system that contains the dislocations. This slip systems has a Schmid factor of 0.314, which is significantly lower than the 0.408 Schmid factor of the $\frac{a}{2}[\bar{1}11](01\bar{1})_\alpha$ activated in tensile loading. This is also inconsistent with all other loadings considered for the Bagaryatskii OR, in which it was the highest Schmid factor slip system that was activated. It can, however, be observed that the $[11\bar{1}](011)_\theta$ slip system

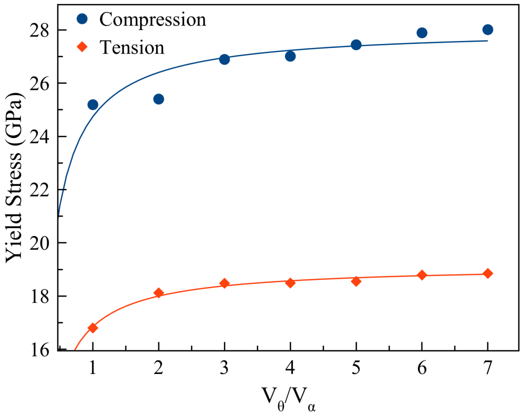

Figure 6.9: Predicted yield stress in tension (red) and compression (blue) under $[001]_\theta$ loading for various volume ratios and associated fit of Equation 6.5. Higher compressive yield strength can be observed due to the compressive strength of cementite, a ceramic. Error in values is smaller than data markers.

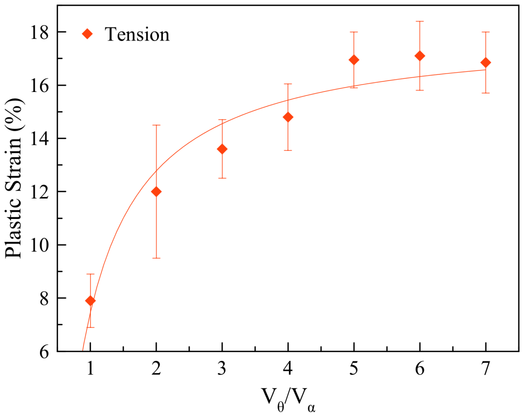

Figure 6.10: Ductility between ferrite and cementite yield in $[001]_\theta$ tensile straining as a function of volume ratio and associated fit to Equation 6.6. Error bars represent strain from ferrite yield to failure.

is activated at roughly the same strain as the ferrite slip system, and this cementite slip systems has a Schmid factor of 0.427, which is the largest among the relevant slip system for this loading. The concurrent yield of the two lamella, in conjunction with the alignment of these slip planes (Fig. 6.6), allows for a slip system to activate within the ferrite that would not otherwise be observed. Once the cementite yields in compressive loading, the system continues to flow plastically as the applied strain direction prevents the delamination observed in tensile loading.

6.2 Near Bagaryatskii Orientation Relationship

For nearly all loading of all ORs, the same behavioral trends seen in the Bagaryatskii are observed. In transverse loading, ferrite is seen to yield first, then the cementite, followed by a constant plastic flow in both materials, with the net response of the system being well defined through composite theory. In longitudinal loading, the plasticity events occur in the same order, with volume ratio playing a significant factor with regards to the yield and flow stresses. Due to these behavioral similarities, the following sections will focus on fully characterizing the system, including slip systems and flow stresses, before moving on to a discussion on how factors such as orientation, dislocation structure, and interface energetics affect the mechanical response of the system. Also to reiterate, for the sake of simplicity, the loading state will be defined relative to the cementite unit cell.

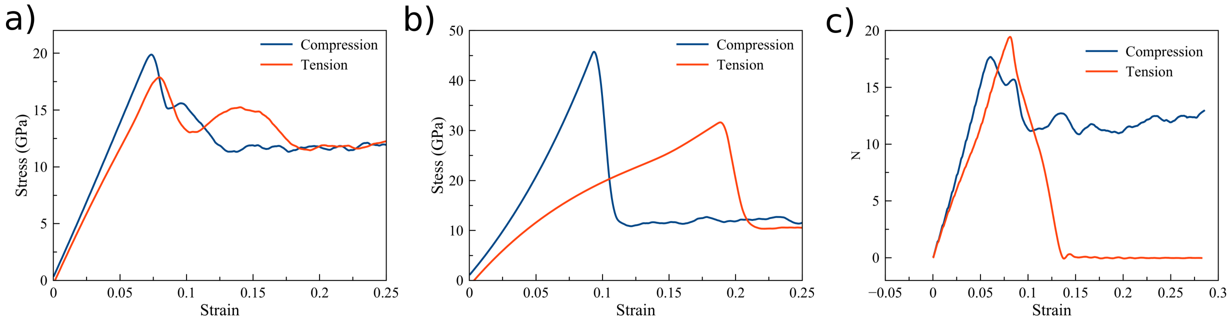

Figure 6.11: Stress-strain response of the Near Bagaryatskii structure in compression (blue) and tension (red) for deformation in the a) $[100]_\theta$ direction, b) $[010]_\theta$ direction, c) $[001]_\theta$ direction for a 7:1 ferrite to cementite ratio with cementite lamella thickness of 4 nm.

From initial observation of Figure 6.11, it can be seen that despite only varying from the Bagaratskii by a few degrees, there are differences in the mechanical response for several of the loading states of the Near Bagaryatskii. In compression, these difference are minor (Fig. 6.12), as the Near Bagaryatskii is observed to have nearly identical elastic moduli and very similar yield and flow stresses to its parent OR. When the resolved shear stresses are considered (Table 6.5), the differences in yield and flow stresses between the two ORs is reduced further. In $[100]_\theta$ compressive loading for example, the resolved shear stress at yield are 7.31 GPa and 9.40 GPa for the ferrite and cementite, respectively, in the Near Bagaryatskii, while the associated values in the Bagaryatskii are 7.50 GPa and 10.54 GPa. Similarly, the ferrite and cementite flow resolved shear stresses for the Near Bagaryatskii are 4.36 GPa and 6.18 GPa in the Near Bagaryatskii and 4.80 GPa and 5.71 GPa in the Bagaryatskii. The slight differences between the two ORs for both yield and flow is likely a result of the different dislocation structure at the interface, which will result in different localized stress states as well as slightly alter the way in which the interface acts as a barrier to plastic flow within the whole system. As would be expected for two ORs that have such similar

Table 6.5: Slip systems and the resolved shear stresses (GPa) for yield (τ_y^{RSS}) and plastic flow (τ_f^{RSS}) in ferrite and cementite for various transverse loading states of the Near Bagaryatskii OR. Values in parenthesis represent the Schmid factor for for the slip system.

		$[100]_\theta$		$[010]_\theta$	
		Tension	Compression	Tension	Compression
Slip System	Ferrite	$[11\bar{1}](101)$ (0.368)	$[\bar{1}1\bar{1}](\bar{1}01)$ (0.368)	$[11\bar{1}](112)$ (0.314)	$[11\bar{1}](112)$ (0.314)
	Cementite	$[\bar{3}11](103)$ (0.369)	$[\bar{1}11](110)$ (0.359)	$[11\bar{1}](011)$ (0.359)	$[11\bar{1}](\bar{1}10)$ (0.359)
τ_y^{RSS}	Ferrite	6.64	7.31	14.22	9.74
	Cementite	5.84	9.40	14.31	11.25
τ_f^{RSS}	Ferrite	4.40	4.36	3.73	3.24
	Cementite	4.86	6.18	9.17	4.82

responses, the slip systems of each of these compressive loading state in both the Bagaryatskii and the Near Bagaryatskii are the same.

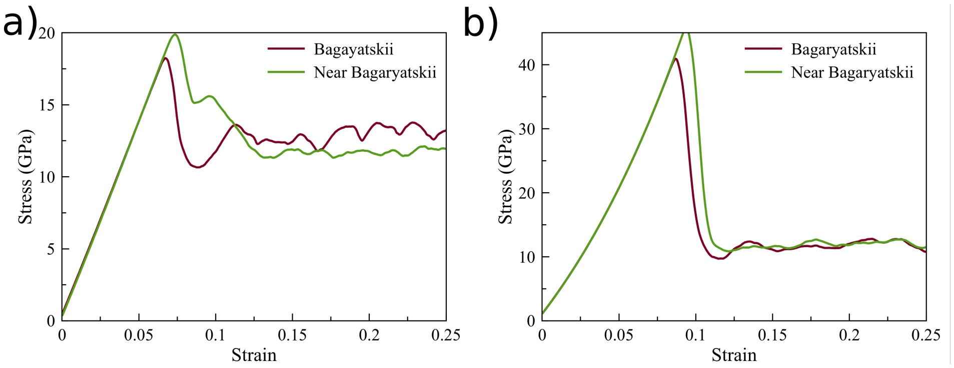

Figure 6.12: Stress-strain comparison between the Bagaryatskii and Near Bagaryatskii ORs during compression in the a) $[100]_\theta$ direction and b) $[010]_\theta$ direction for a 7:1 ferrite to cementite volume ratio. Response is seen to be similar due to the activation of the same slip systems in both ORs.

For tensile straining, the differences between the Near Bagaryatskii and its parent OR are more pronounced (Fig. 6.13). The elastic responses are still roughly the same, which is to be expected due to the similar orientations, but for both the $[100]_\theta$ and $[010]_\theta$ there are variations once plasticity occurs. These observed differences in yield and flow can be shown to be a function of the alignment of slip planes between the ferrite and cementite. In $[100]_\theta$ tensile loading of the Near Bagaryatskii, the ferrite yields first with slip occurring on the $\frac{a}{2}[11\bar{1}](101)_\alpha$ slip system, as it does in the Bagaryatskii. When the cementite yields however, the slip occurs in the $0.15[\bar{3}11](103)_\theta$ slip system, while the $\frac{a}{2}[\bar{1}1\bar{1}](110)_\alpha$ secondary slip system is activated simultaneously in the ferrite.

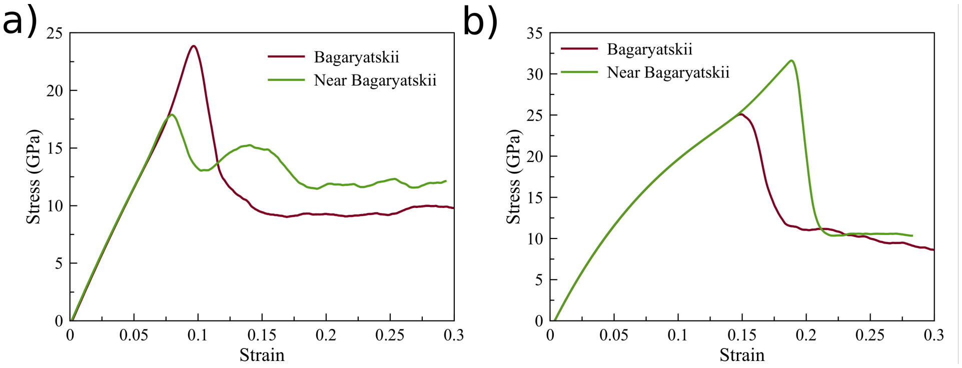

Figure 6.13: Stress-strain comparison between the Bagaryatskii and Near Bagaryatskii ORs during tension in the a) $[100]_\theta$ direction and b) $[010]_\theta$ direction for a 7:1 ferrite to cementite volume ratio. Variation between the two ORs is due to the altering of alignment between the slip systems in the ferrite and cementite.

These two slip planes are perfectly aligned, as they are part of the defined symmetries of the two crystal within the Near Bagaryatskii OR. The alignment of $0.15[\bar{3}11](103)_\theta$ and the $\frac{a}{2}[\bar{1}1\bar{1}](110)_\alpha$ further aids in the activation of the slip system in cementite, which is why the system does not activate in the Bagaryatskii where the two are not perfectly aligned. While the slight differences in orientation between the Bagaryatskii and Near Bagaryatskii result in slip plane alignments in the two crystals that activates in the Near Bagaryatskii during $[100]_\theta$ loading, it also results in a rotation away from the aligned slip planes that activated during the $[010]_\theta$ tensile loading of the Bagaryatskii, the $[11\bar{1}](112)_\alpha$ and $[11\bar{1}](011)_\theta$. These are still the activated slip systems in the Near Bagaryatskii, however due to the lack of alignment, the critical resolved shear stress for each of them is higher than in the Bagaryatskii. Once yield occurs, the flow stresses of the two ORs are found to be very similar, which is to be expected since the same slip systems were activated. However the Near Bagaryatskii does flow at a slightly higher stress as the cementite can no longer flow at the same stress as the ferrite since the planes are no longer aligned. This raises the the net flow stress of the system, a volume average of the two components, since the cementite has a higher flow stress than the ferrite.

Perhaps the most glaring difference between the Bagaryatskii and Near Bagaryatskii is the lack of a ductile phase during the tensile, longitudinal loading of the Near Bagayatskii. During the ductile phase, it is necessary for the cementite to allow stress to flow between lamella. This is seen

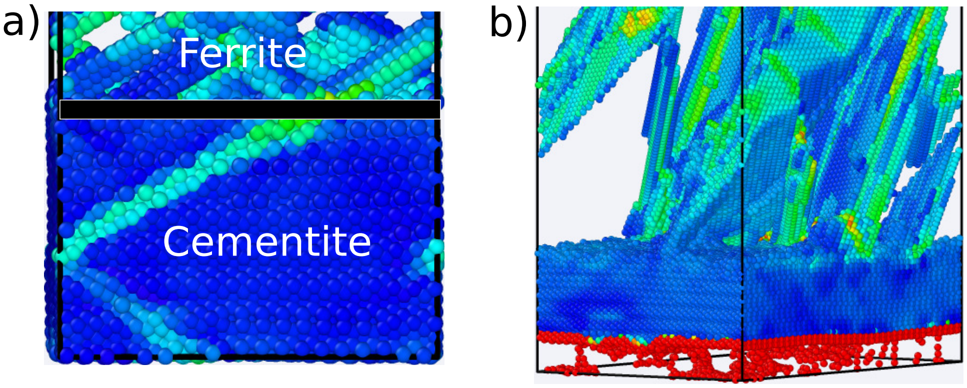

Figure 6.14: a) Alignment of the $(110)_\alpha$ and $(101)_\theta$ in the Bagaryatskii OR that allows plastic flow during longitudinal loading. b) Delamination caused by lack of alignment of the slip planes in the Near Bagaryatskii.

to be the case in the Bagaryatskii, where the $(110)_\alpha$ on which the ferrite is slipping aligns nearly perfectly with the $(101)_\theta$ (Fig. 6.14a). However in the Near Bagaryatskii, the rotation of ferrite means that these planes no longer align. As a result, the ferrite slip plane forms at a very low angle to the interface, resulting in a shear on the interface plane. As a result, the system simply fails through delamination as opposed to ductile flow. While the same lack of alignment holds true for in compression, the strain state prevents delamination, and therefore the system plastically flows. The yield and flow stresses are still found to be a function of the volume ratio, as seen in Figure 6.15, with the fitting parameters given in Table 6.6.

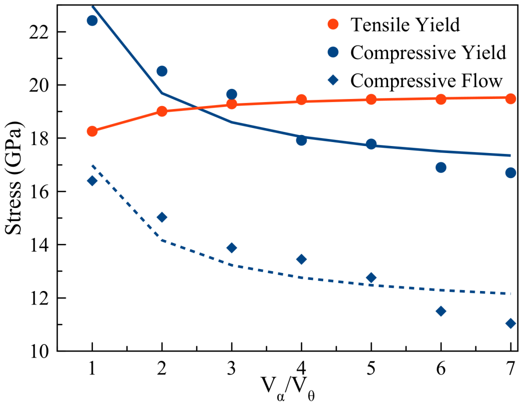

Figure 6.15: Yield and flow stress as a function of volume ratio for longitudinal loading of the Near Bagaryatskii OR.

Table 6.6: Calculated constants for the volume ratio dependent flow stress and yield stress (Eqs. 6.4 and 6.5) of the Near Bagaryatskii OR during longitudinal loading. As there is no plastic flow in tensile loading, the system fails rapidly after the initial ferrite yielding, only the compressive flow stress terms are given. Values were determined using a least squares fit of simulation data.

$\sigma_{0,t}$	$\sigma_{0,c}$	$K_{0,t}$	$K_{0,c}$	$\sigma_{1,c}$	$K_{1,c}$
19.74 GPa	16.41 GPa	-1.47 GPa	6.56 GPa	11.35 GPa	5.64 GPa

6.3 Pitsch-Petch and Near Pitsch-Petch Orientation Relationships

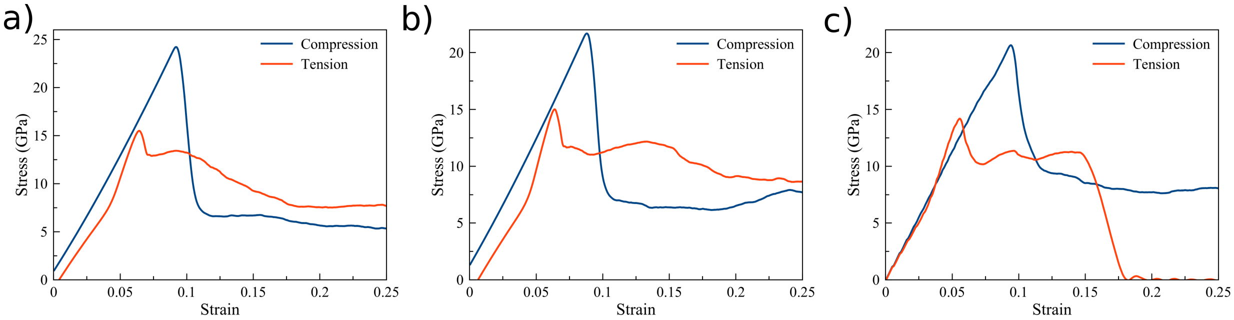

Figure 6.16: Stress-strain response of the Pitsch-Petch OR in compression (blue) and tension (red) for deformation in the a) $[100]_\theta$ direction, b) $[010]_\theta$ direction, c) $(001)_\theta$ direction for a 7:1 ferrite to cementite ratio with cementite lamella thickness of 4 nm.

From Figures 6.16 and 6.17, it can be observed that the Pitsch-Petch and Near Pitsch-Petch have nearly identical mechanical response, as for a given loading the same slip systems are activated in each OR, and the yield and flow stress values are found to vary by less than 5%. Therefore all values for yield and flow stress presented in this section will be with regards to the Pitsch-Petch OR, however there will be discussion on why the Near Pitsch-Petch behaves so similarly to its parent OR. It is notable though that the structure of the interfaces for these ORs are not the same, suggesting that interfacial structure may be of limited importance to mechanical response.

The ferrite slip systems for all transverse loadings of the Pitsch-Petch were found to lie on the $\{110\}_\alpha$ family of planes, with most having Schmid factors greater than 0.44 (Table 6.7). The one exception to this is the tensile $[100]_\theta$ loading, for which the Schmid factor of the activated ferrite slip system is 0.377. The activation of this lower Schmid factor slip system is result of

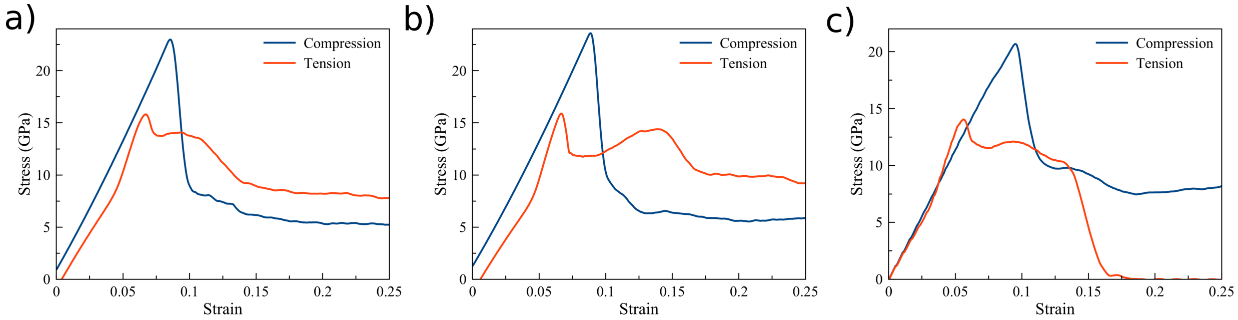

Figure 6.17: Stress-strain response of the Near Pitsch-Petch OR in compression (blue) and tension (red) for deformation in the a) $[100]_\theta$ direction, b) $[010]_\theta$ direction, c) $(001)_\theta$ direction for a 7:1 ferrite to cementite ratio with cementite lamella thickness of 4 nm.

Table 6.7: Slip systems and the resolved shear stresses (GPa) for yield (τ_y^{RSS}) and plastic flow (τ_f^{RSS}) in ferrite and cementite for various transverse loading states of the Pitsch-Petch OR. Values in parenthesis represent the Schmid factor for for the slip system.

		$[100]_\theta$		$[010]_\theta$	
		Tension	Compression	Tension	Compression
Slip System	Ferrite	$[1\bar{1}1](110)$ (0.377)	$[11\bar{1}](1\bar{1}0)$ (0.458)	$[111](10\bar{1})$ (0.441)	$[11\bar{1}](011)$ (0.457)
	Cementite	$[\bar{3}11](103)$ (0.369)	$[111](\bar{1}01)$ (0.393)	$[111](\bar{1}10)$ (0.359)	$[11\bar{1}](011)$ (0.359)
τ_y^{RSS}	Ferrite	5.72	11.05	6.20	9.88
	Cementite	8.17	9.04	7.15	9.02
τ_f^{RSS}	Ferrite	2.34	2.87	3.82	2.80
	Cementite	5.78	7.38	5.77	7.81

the alignment of the $(110)_\alpha$ and $(103)_\theta$ planes, which are the same slip system that activated for this loading in the Near Bagaryatskii OR. It is notable that this system for Pitsch-Petch, Near Pitsch-Petch, and Near Bagaryatskii, only activates in tensile straining, suggesting that the critical resolved shear stress for this slip system is lower in tension. Plasticity in the cementite is found to occur on slip systems that align well with those that were activated in the ferrite, as has been observed in the other ORs. For longitudinal loading, in both compression and tension, $[11\bar{1}](112)_\alpha$ dislocation are found to form in the ferrite, which has a Schmid factor of 0.424, while cementite deformation occurs on the $[111](01\bar{1})_\theta$ slip system, with a Schmid factor of 0.427. The mechanical response is found to have the volume ratio dependence (Fig. 6.18) seen in the Bagaryatskii and Near Bagarystkii. The fitting parameters of the curves can be found in Table 6.9.

An interesting observation is the near identical response of the Pitsch-Petch and its associated near OR, while the Bagaryatskii and its near OR are found to have notable differences. This

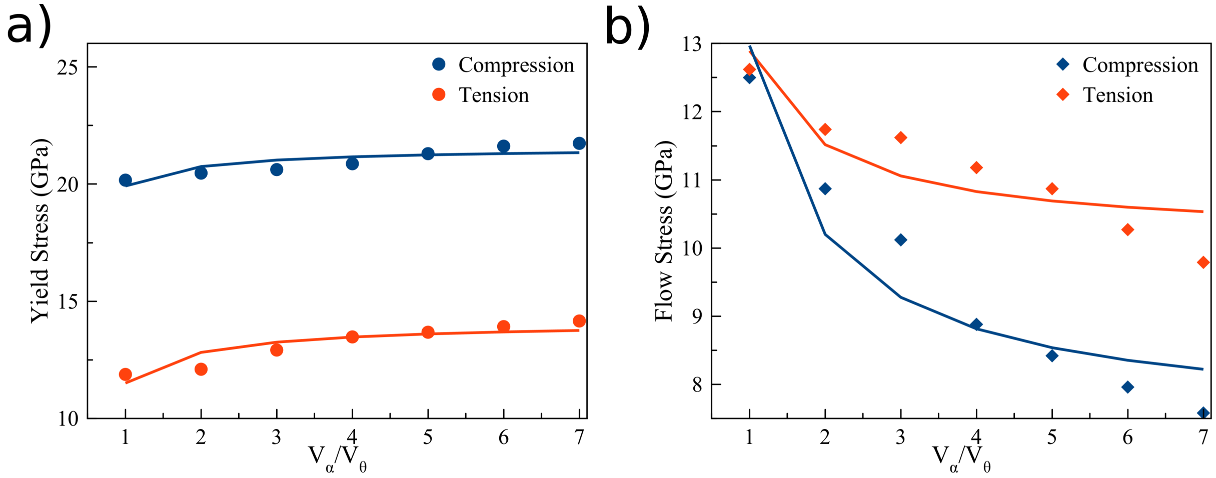

Figure 6.18: Yield and flow stress as a function of volume ratio for compressive and tensile longitudinal loading of the Pitsch-Petch OR.

Table 6.8: Schmid factors for the Near Pitsch-Petch OR under transverse loading. For all loading states, the same slip systems are activated in the Near Pitsch-Petch and the Pitsch-Petch ORs (Table 6.7).

$[100]_\theta$		$[010]_\theta$	
Tension	Compression	Tension	Compression
0.383	0.468	0.445	0.445

discrepancy likely arises from the axis about which the system is rotated to create the Near OR. For the Near Bagaryatskii the rotation is about the $[111]_\alpha$, and as such there are multiple $\{110\}$ and $\{112\}$ planes that undergo the full magnitude of this rotation, thus having a larger impact on the Schmid factor. In the Near Pitsch-Pitsch, the rotation is first about the $[521]_\alpha$ axis, and then about the $[\bar{1}3\bar{1}]_\alpha$ direction. Both of these rotations are more modest than the one performed in the Bagaryatskii. In addition, none of the slip planes that are activated during the straining of the Pitsch-Petch ORs contain these vectors, and as such the magnitude of the rotation is reduced. The limited effect of this rotation can be shown with the Schmid factors of the Near Pitsch-Petch (Table 6.8), which are seen to closely correspond to the Schmid factors of the Pitsch-Petch.

Table 6.9: Calculated constants for the volume ratio dependent flow stress and yield stress (Eqs. 6.4 and 6.5) of the Pitsch-Petch OR during longitudinal loading. Values were determined using a least squares fit of simulation data.

$\sigma_{0,t}$	$\sigma_{0,c}$	$K_{0,t}$	$K_{0,c}$	$\sigma_{1,t}$	$\sigma_{1,c}$	$K_{1,t}$	$K_{1,c}$
14.13 GPa	21.58 GPa	-2.62 GPa	-1.66 GPa	10.14 GPa	7.43 GPa	2.75 GPa	5.54 GPa

6.4 Isaichev Orientation Relationship

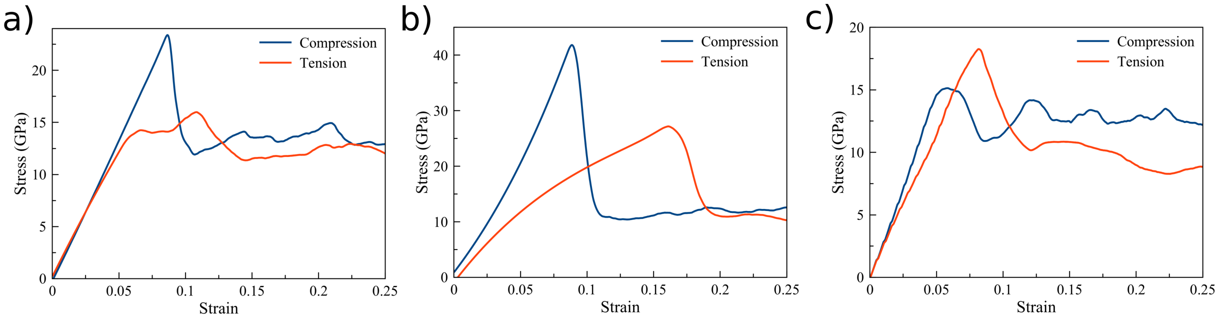

Figure 6.19: Stress-strain response of the Isaichev in compression (blue) and tension (red) for deformation in the a) $[\bar{1}01]_\theta$ direction, b) $[010]_\theta$ direction, c) $[101]_\theta$ direction for a 7:1 ferrite to cementite ratio with cementite lamella thickness of 4 nm.

While the Bagaryatskii, the Pitsch-Petch, and their associated near ORs all have the same orientation of the cementite relative to the interface plane, the Isaichev differs from these ORs, as the $[\bar{1}01]_\theta$ direction lies in its interface plane as opposed to the $[100]_\theta$. While this limits the ability to discern trends within the pearlite system from the Isaichev mechanical response, it does give the opportunity to better understand other potential slip planes within the cementite as many of the $\{110\}_\theta$ family of slip planes that have been observed in the other ORs will result in a Schmid factor of zero. As is the case for all the other ORs, in transverse loading the ferrite yields first. The orientation of the ferrite relative to the loading in the Isaichev OR is identical to that of the Bagaryatskii OR, and as such, the transverse slip systems within the ferrite are identical for the two. There are variations in the activated slip systems of the cementite though (Table 6.10). The $[210](\bar{1}21)$ system can be observed for loading in the $[010]_\theta$ direction, while the $\{100\}$ family of slip planes are seen to be activated for $[\bar{1}01]_\theta$ loading. As has been the case for all ORs, these slip planes are found to have high Schmid factors and align with slip planes in the ferrite.

One of the more interesting response mechanisms is that of the tensile, longitudinal loading. The cementite in these simulations had still not failed at 40% strain. This is due to the alignment of the $[100](001)$ slip plane in the cementite with the $[\bar{1}11](01\bar{1})$ in the ferrite (Fig. 6.20). As other ORs have been found to have aligned slip planes activated during longitudinal loading, the

Table 6.10: Slip systems and the resolved shear stresses (GPa) for yield (τ_y^{RSS}) and plastic flow (τ_f^{RSS}) in ferrite and cementite for various transverse loading states of the Isaichev OR. Values in parenthesis represent the Schmid factor for for the slip system.

		$[\bar{1}01]_\theta$		$[010]_\theta$	
		Tension	Compression	Tension	Compression
Slip System	Ferrite	$[\bar{1}1\bar{1}](110)$ (0.408)	$[\bar{1}11](01\bar{1})$ (0.408)	$[11\bar{1}](112)$ (0.314)	$[11\bar{1}](112)$ (0.314)
	Cementite	$[100](001)$ (0.468)	$[001](100)$ (0.468)	$[210](\bar{1}21)$ (0.403)	$[210](\bar{1}21)$ (0.403)
τ_y^{RSS}	Ferrite	9.71	7.34	7.82	12.49
	Cementite	8.15	10.33	8.51	23.85
τ_f^{RSS}	Ferrite	4.02	5.29	3.07	3.82
	Cementite	9.00	7.58	4.56	5.74

inference here would be that the $[100](001)$ is particularly adept plastically flowing without failure. This slip system is also interesting in that in compression the ferrite and cementite yield at the same time, at a stress of $\approx$15 GPa. As a result, the interface compatibility no longer causes a volume ratio dependent response, as this constraint was a result of the plastically deforming ferrite expanding or contracting more than the elastically deforming cementite. The flow stress is also seen to be independent of the volume ratio, with a value of $\approx$13 GPa for all ferrite to cementite ratios. This is unique to the compressive response, as in tension the ferrite yields first and the same volume ratio dependence as seen in the other ORs is observed (Fig. 6.21 and Table 6.11).

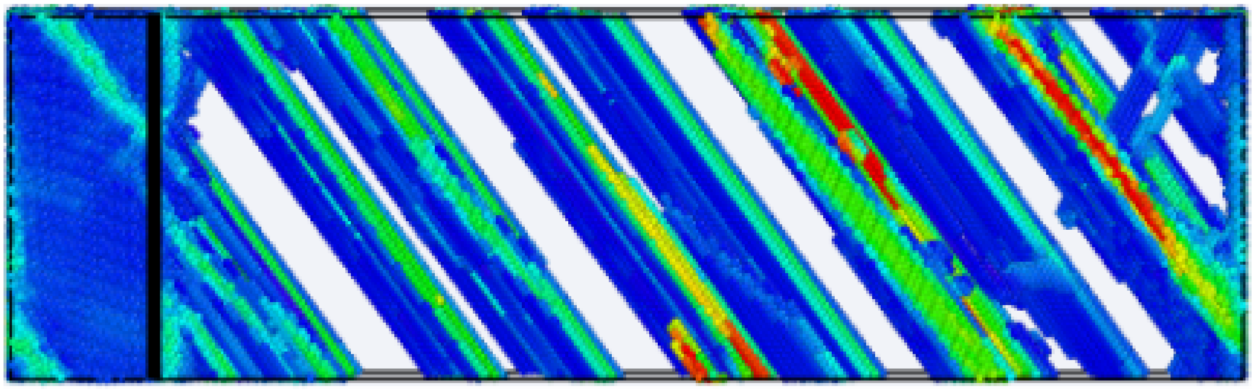

Figure 6.20: Alignment between the $[100](001)_\theta$ slip plane in the cementite (left) with the $[\bar{1}11](01\bar{1})_\alpha$ in the ferrite (right), allowing stress to flow between lamella.

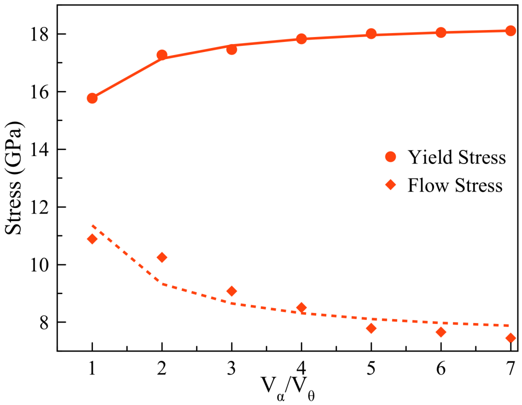

Figure 6.21: Yield and flow stress as a function of volume ratio for longitudinal loading of the Isaichev OR.

Table 6.11: Calculated constants for the volume ratio dependent flow stress and yield stress (Eqs. 6.4 and 6.5) of the Isaichev OR during tensile longitudinal loading. Values were determined using a least squares fit of simulation data.

$\sigma_{0,t}$	$K_{0,t}$	$\sigma_{1,t}$	$K_{1,t}$
18.50 GPa	-2.71 GPa	7.30 GPa	4.06 GPa

6.5 Comparison of the Orientation Relationships

For all ORs, the activated slip systems in both the ferrite and cementite was generally found to be the one which had the largest Schmid factor. In the cases, where lower Schmid factor slip systems were activated, this was found to be the result of closely aligned slip planes in the ferrite and cementite. As both the Schmid factor and the alignment of slip planes are determined by the relative orientation of the crystals, it would appear that it is in fact the orientation that is the dominant factor in determining mechanical response. Furthermore, the elastic response in all cases was well defined using composite theory in conjunction with the appropriate elastic modulus for the orientation of the crystal. There are however other considerations that should also be accounted for. One of these is the effect of interfacial chemistry on mechanical response, which can also give some insight into the effect of interfacial energy on the response, as the various chemistries within an OR will have identical orientation and interface structure. Thus by comparing the mechanical response of the chemistries, some insight can be gained into the role of interfacial energy on mechanical response. This is relevant as it has been proposed in this work that the reason the Pitsch-Petch and near Pitsch-Petch had near identical responses while the Bagaryatskii and near Bagaryatskii had more variation was related to slip plane alignment. However, it is also possible energetic played a role, as the difference in interfacial energy between the former set is 0.01 J/m^2, while for the latter it is 0.12 J/m^2. Thus simulations were performed, at a 7:1 ferrite to cementite ratio, for all chemistries of each OR. Figure 6.22 shows mechanical testing performed on the three chemistries of the Pitsch-Petch, which has a range of interfacial energy between its lowest and highest energy chemistries of 0.20 J/m^2, more than the variation between the Bagaryatskii and the Near Bagaryatskii. It can clearly be observed that there is only minimal variation between the chemistries. The only differences in response, are with regards to yield stress, which would to be expected to have some variation with changes in chemistry, as the different interfacial energies are likely to be at least partially a result of different localized stress states at the interface.

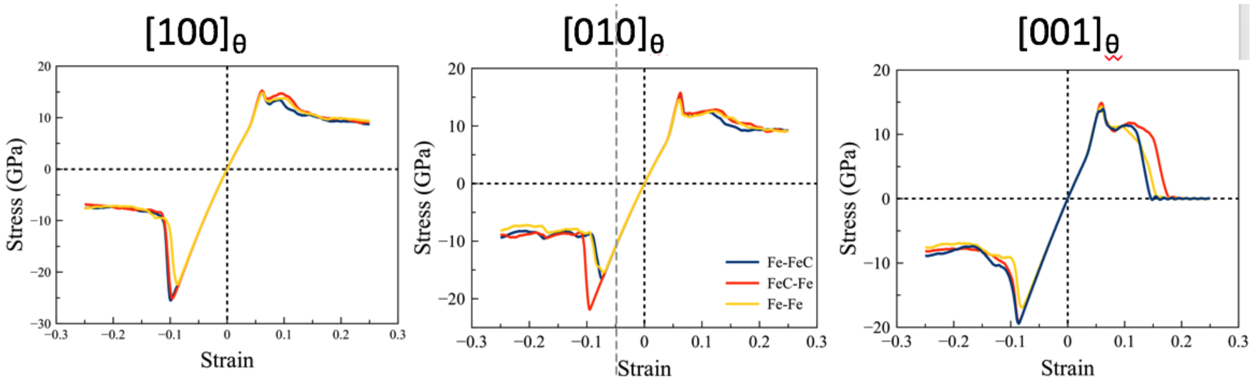

Figure 6.22: Stress strain response of the three interfacial chemistries of the Pitsch-Petch OR.

It therefore appears that alignment of slip system is the dominant consideration when considering the mechanical response. Most of the individual events that occur during these simulations is fairly well defined. Plasticity begins in the ferrite, generally with the formation of $\langle 111\rangle\{110\}$ dislocations that form on slip systems with high Schmidt factors, although some slip systems do form on $\{112\}$ planes. Plasticity in the cementite is preferred on the $\{100\}$ and $\{110\}$ planes, unless a ferrite slip plane aligns well with a different plane in the cementite, and again, it does so on planes with high Schmid factors. Transverse loading are well explained through volume averaged behavior of the two lamella, while longitudinal loading requires the consideration of interface compatibility.

6.6 Summary

Atomistic simulations are used to characterize and quantify the mechanical response of the various proposed ORs of pearlite. Simulations reveal that the interface and volume ratios of ferrite and cementite play a significant role in this response. Flow stresses within both the ferrite and cementite are observed to be constant regardless of size, with the ferrite flow stress consistent with bulk values, while the cementite flow stress is noticeably higher than the bulk values. The strains at which plasticity begins in both the ferrite and cementite also remain constant, meaning that the ductility of the system is the same regardless of size or volume ratio, consistent with the results of Modi et al. Using the tabulated values for elastic modulus, yield stress, flow stress, and ductility, it is now possible to interpolate mechanical response in the transverse direction over a large range of volume ratios.

The mechanical response in the longitudinal direction was found to be slightly more complicated. As ferrite was observed to plastically deform first, the compatibility of the interface was found to play a major role in the yield stress, flow stress, and ductility of the system. Relations were developed for these values for both tensile and compressive loading, again allowing for the interpolation of these values over a range of volume ratios. For specific volume ratios, strength and ductility were found to be size independent, again consistent with the findings of Modi et al. Ferrite was observed to play the dominant role in plastic flow. In tension, the system flows at the constrained ferrite value and then rapidly fails once cementite begins to nucleate dislocations. In compression, the system simply flows at the constrained ferrite flow stress. Both of these observations are consistent with metal-ceramic laminates, which are known to have high strength in compression but are brittle in tension.

The development of these models will allow for the potential tuning of size and volume ratio to desired mechanical properties. One example would be the ability to balance strength, which increases with ferrite volume ratio, with a more continuous plastic response, which occurs as the ferrite volume ratio decreases. Additionally, the ability of aligned slip systems to increase the ductility of the system could allow for the ability to use materials of specific orientation relationships based on the deformation state that they will undergo.

Chapter 7

Future Work

While this work has sought to provide a thorough study of the ferrite-cementite and austenite-cementite interfaces there is still a significant amount of work that could still be conducted in this field. Several potential avenues of research will be summarized in this section.

Pearlite Habit Planes

The results of the atomistic analysis of the mechanical response of pearlite highlighted the importance of aligning favorable slip planes within the ferrite and cementite. It therefore could prove fruitful to analyze alternative habit planes for commonly reported ORs found in literature that better align these slip planes. Furthermore, as the technology to create pearlite artificially, such as through nitrocarburizing, is improved, it may become possible to create alternative ORs that also align the slip planes. One possible approach to search out these alternative habit planes and ORs is that of Zhang et al. [29, 30], which was used to determine potential habit planes for the Pitsch and Thompson-Howell ORs in austenite. As this approach requires the consideration of the reciprocal space structure of both the ferrite and the cementite, it would first be necessary to generate these structures. This could be done through the already implemented virtual diffraction package within LAMMPS [181]. By combining these generated structures with the metric created by Zhang, it would be possible to create scripts that could scan for favorable habit planes and ORs, on which energetic and mechanical simulations could then be run.

Surface Energies

While this work sought to characterize the energetics of the interface that forms between the ferrite and cementite lamella in pure pearlite, this will not be the only interface for many pearlite colonies. Since pearlite is a line compound, any surplus or deficiency of carbon will result in the formation of pearlite in a matrix of ferrite or cementite. As such, in addition to the interfaces analyzed in this work, there will also be interfaces between cementite and ferrite on the “sides" of the lamella. These additional interfaces will further influence the energetics of the system, and may influence which OR is most likely to form. The construction of these simulations is far from trivial as these additional interfaces will form on all sides of the lamella and therefore cannot be simulated by a single habit plane. One possible approach is to create a “coin" of cementite in a ferrite matrix, or vice versa, and after relaxation analyze the resultant shape and energetics. The consideration of these additional interfaces is also likely important to the austenite-cementite interface, as the stepped structure results in a second interface plane between the two crystals. The analysis of these interfaces is however more straightforward, as the habit plane should be perpendicular to the favorable austenite-cementite planes determined in this work.

Austenite Mechanical Testing

With a methodology and framework developed to run mechanical testing simulations on the pearlite, this same approach could be adapted rather quickly to austenite with the hope that the manner in which the austenite-cementite system fails under various loading states can be better understood. It seems likely that the alignment of favorable slip systems within the two lamella will allow for better ductility, as is the case for the ferrite-cementite system. Defining these slip systems, as well creating constitutive laws to define the response, could allow for better models for the failure of austenitic steels.

Multi-scale Modeling

Part of the impetus for implementing the continuum method used in this work was to create models for the pearlite system that have at a lower computational cost than atomistics. When creating larger-scale models, such as those for grain growth, it is not plausible to atomistically analyze all relative orientations that might occur. As such, existing mesoscale models often use bulk properties when considering values such as interfacial energies. By developing these continuum models, it may be possible to create relations that are computationally efficient enough to be implemented into the mesoscale models. This would allow for the consideration of microstructural properties that are often times not considered. The same is true for the developed constitutive relations in relation to processing models. While these continuum models are undeniably less precise than atomistics, there lower cost allows t them to be used in ways that are oftentimes more relevant to both industry and the military. .

Shock Response

An area of particular interest for steel is how it responds to impact shock, as there are obvious industry and military applications to this topic. The methodology simulation shock is well established in LAMMPS, and as such the various ORs could be subjected to shock, and determination made on the influence of orientation, interface structure, and energetics on the response.

Bibliography

[1] Taleff, E. M., Lewandowski, J. J. & Pourladian, B. Microstructure-property relationships in pearlitic eutectoid and hypereutectoid carbon steels. *JOM* **54**, 25–30 (2002).

[2] Callister, W. D. & Rethwisch, D. G. *Materials Science and Engineering: An Introduction*, vol. 7 (Wiley New York, 2007).

[3] Phillpot, S. R., Wolf, D. & Yip, S. Effects of atomic-level disorder at solid interfaces. *MRS Bulletin* **15**, 38–45 (1990).

[4] Jiang, C., Srinivasan, S., Caro, A. & Maloy, S. Structural, elastic, and electronic properties of Fe_3C from first principles. *Journal of Applied Physics* **103**, 043502 (2008).

[5] Was, G. & Foecke, T. Deformation and fracture in microlaminates. *Thin Solid Films* **286**, 1–31 (1996).

[6] Wang, J., Hoagland, R. G. & Misra, A. Mechanics of nanoscale metallic multilayers: From atomic-scale to micro-scale. *Scripta Materialia* **60**, 1067–1072 (2009).

[7] Song, W. *et al.* Atomic-scale investigation of ε and θ precipitates in bainite in 100Cr6 bearing steel by atom probe tomography and ab initio calculations. *Acta Materialia* **61**, 7582–7590 (2013).

[8] Howell, P. R. The pearlite reaction in steels mechanisms and crystallography: Part I. From HC Sorby to RF Mehl. *Materials Characterization* **40**, 227–260 (1998).

[9] Bagaryatskii, Y. A., Nosova, G. & Tagunova, T. O kristallicheskoi strukture i prirode omega-fazy v splavakh titana s khromom. *Doklady Akademii Nauk Sssr* **105**, 1225 (1955).

[10] Zhang, M.-X. & Kelly, P. Accurate orientation relationships between ferrite and cementite in pearlite. *Scripta Materialia* **37**, 2009–2015 (1997).

[11] Mangan, M. & Shiflet, G. The Pitsch-Petch orientation relationship in ferrous pearlite at small undercooling. *Metallurgical and Materials Transactions A* **30**, 2767–2781 (1999).

[12] Zhou, D. & Shiflet, G. Ferrite: cementite crystallography in pearlite. *Metallurgical Transactions A* **23**, 1259–1269 (1992).

[13] Morgan, R. & Ralph, B. A field-ion microscope study of pearlite. *J. Iron Steel Inst.* **206** (1968).

[14] Bowden, H. & Kelly, P. The crystallography of the pressure induced phase transformations in iron alloys. *Acta Metallurgica* **15**, 1489–1500 (1967).

[15] Shackleton, D. & Kelly, P. Orientation relationship in pearlite and the pearlite-austenite interface. *J. Iron Steel Inst.* **207**, 1253–1254 (1969).

[16] Schastlivtsev, V. & Yakovleva, I. Electron-microscope study of structural transformations in pearlite. *Fizika Metallov Metallovedenie* **38**, 571–579 (1974).

[17] Sukhomlin, G. Crystal-geometry characteristics of the pearlite of hypoeutectoid steel. *Fiz. Met. Metalloved.* **42**, 965–970 (1976).

[18] Guo, N. & Liu, Q. Back-scattered electron imaging combined with EBSD technique for characterization of pearlitic steels. *Journal of Microscopy* **246**, 221–228 (2012).

[19] Pitsch, W. Der orientierungszusammenhang zwischen zementit und austenit. *Acta Metallurgica* **10**, 897–900 (1962).

[20] Samuel, F. & Hussein, A. A crystallographic study of nucleation of pearlite. *Transactions of the Iron and Steel Institute of Japan* **23**, 65–70 (1983).

[21] Dippenaar, R. & Honeycombe, R. The crystallography and nucleation of pearlite. *Proc. R. Soc. Lond. A* **333**, 455–467 (1973).

[22] Zhang, X. *et al.* Carbon-content dependent effect of magnetic field on austenitic decomposition of steels. *Journal of Magnetism and Magnetic Materials* **324**, 1385–1390 (2012).

[23] Zhang, Y., Esling, C., Calcagnotto, M., Zhao, X. & Zuo, L. New insights into crystallographic correlations between ferrite and cementite in lamellar eutectoid structures, obtained by SEM–FEG/EBSD and an indirect two-trace method. *Journal of Applied Crystallography* **40**, 849–856 (2007).

[24] Zhong, N., Wang, X., Guo, Z. & Rong, Y. Orientation relationships between ferrite and cementite by edge-to-edge matching principle. *Journal of Materials Science & Technology* **27**, 475–480 (2011).

[25] Tekin, E. & Kelly, P. A study of the tempering of steel using transmission electron microscopy (1965).

[26] Spanos, G. & Kral, M. The proeutectoid cementite transformation in steels. *International Materials Reviews* **54**, 19–47 (2009).

[27] Thompson, S. & Howell, P. A preliminary comparison of two apparently diverse cementite/austenite orientation relationships. *Scripta Metallurgica* **22**, 229–233 (1988).

[28] Spanos, G. & Aaronson, H. The interfacial structure and habit plane of proeutectoid cementite plates. *Acta Metallurgica et Materialia* **38**, 2721–2732 (1990).

[29] Zhang, W.-Z., Ye, F., Zhang, C., Qi, Y. & Fang, H.-S. Unified rationalization of the Pitsch and T–H orientation relationships between Widmanstätten cementite and austenite. *Acta Materialia* **48**, 2209–2219 (2000).

[30] Howe, J. & Spanos, G. Atomic structure of the austenite-cementite interface of proeutectoid cementite plates. *Philosophical Magazine A* **79**, 9–30 (1999).

[31] Yang, K. & Choo, W. The variants of the orientation relationship between austenite and cementite in Fe-30wt% Mn-1.0 wt% C alloy. *Acta Metallurgica et Materialia* **42**, 263–269 (1994).

[32] Sutton, A. P. & Balluffi, R. W. *Interfaces in crystalline materials* (Clarendon Press, 1995).

[33] Olmsted, D. L., Foiles, S. M. & Holm, E. A. Survey of computed grain boundary properties in face-centered cubic metals: I. Grain boundary energy. *Acta Materialia* **57**, 3694–3703 (2009).

[34] Foiles, S. M. Temperature dependence of grain boundary free energy and elastic constants. *Scripta Materialia* **62**, 231–234 (2010).

[35] Sangid, M. D., Sehitoglu, H., Maier, H. J. & Niendorf, T. Grain boundary characterization and energetics of superalloys. *Materials Science and Engineering: A* **527**, 7115–7125 (2010).

[36] Tschopp, M. A., Spearot, D. E. & McDowell, D. L. Influence of grain boundary structure on dislocation nucleation in FCC metals. *Dislocations in Solids* **14**, 43–139 (2008).

[37] Homer, E. Investigating the mechanisms of grain boundary migration during recrystallization using molecular dynamics. In *IOP Conference Series: Materials Science and Engineering*, vol. 89, 012006 (IOP Publishing, 2015).

[38] Coleman, S. P., Spearot, D. E. & Foiles, S. M. The effect of synthetic driving force on the atomic mechanisms associated with grain boundary motion below the interface roughening temperature. *Computational Materials Science* **86**, 38–42 (2014).

[39] Van Swygenhoven, H. & Derlet, P. Grain-boundary sliding in nanocrystalline FCC metals. *Physical Review B* **64**, 224105 (2001).

[40] Homer, E. R., Patala, S. & Priedeman, J. L. Grain boundary plane orientation fundamental zones and structure-property relationships. *Scientific Reports* **5**, 15476 (2015).

[41] Mishin, Y., Asta, M. & Li, J. Atomistic modeling of interfaces and their impact on microstructure and properties. *Acta Materialia* **58**, 1117–1151 (2010).

[42] Dillon, S. J. & Harmer, M. P. Multiple grain boundary transitions in ceramics: A case study of alumina. *Acta Materialia* **55**, 5247–5254 (2007).

[43] Tucker, G. J. & McDowell, D. L. Non-equilibrium grain boundary structure and inelastic deformation using atomistic simulations. *International Journal of Plasticity* **27**, 841–857 (2011).

[44] Tucker, G. J. & Foiles, S. M. Molecular dynamics simulations of rate-dependent grain growth during the surface indentation of nanocrystalline nickel. *Materials Science and Engineering: A* **571**, 207–214 (2013).

[45] Misra, A., Demkowicz, M., Zhang, X. & Hoagland, R. The radiation damage tolerance of ultra-high strength nanolayered composites. *JOM* **59**, 62–65 (2007).

[46] Ratanaphan, S. *et al.* Grain boundary energies in body-centered cubic metals. *Acta Materialia* **88**, 346–354 (2015).

[47] Kim, H.-K., Ko, W.-S., Lee, H.-J., Kim, S. G. & Lee, B.-J. An identification scheme of grain boundaries and construction of a grain boundary energy database. *Scripta Materialia* **64**, 1152–1155 (2011).

[48] Tschopp, M. A. *et al.* Probing grain boundary sink strength at the nanoscale: Energetics and length scales of vacancy and interstitial absorption by grain boundaries in α-Fe. *Physical Review B* **85**, 064108 (2012).

[49] Wolf, D. Correlation between the energy and structure of grain boundaries in BCC metals I. symmetrical boundaries on the (110) and (100) planes. *Philosophical Magazine B* **59**, 667–680 (1989).

[50] Wolf, D. Structure and energy of general grain boundaries in BCC metals. *Journal of Applied Physics* **69**, 185–196 (1991).

[51] Tsurekawa, S., Tanaka, T. & Yoshinaga, H. Grain boundary structure, energy and strength in molybdenum. *Materials Science and Engineering: A* **176**, 341–348 (1994).

[52] Demkowicz, M., Hoagland, R. & Hirth, J. Interface structure and radiation damage resistance in Cu-Nb multilayer nanocomposites. *Physical Review Letters* **100**, 136102 (2008).

[53] Zhang, R., Wang, J., Beyerlein, I. & Germann, T. Dislocation nucleation mechanisms from FCC/BCC incoherent interfaces. *Scripta Materialia* **65**, 1022–1025 (2011).

[54] Demkowicz, M. J., Wang, J. & Hoagland, R. G. Interfaces between dissimilar crystalline solids. *Dislocations in Solids* **14**, 141–205 (2008).

[55] Demkowicz, M. & Hoagland, R. Structure of Kurdjumov–Sachs interfaces in simulations of a copper–niobium bilayer. *Journal of Nuclear Materials* **372**, 45–52 (2008).

[56] Demkowicz, M. & Thilly, L. Structure, shear resistance and interaction with point defects of interfaces in Cu–Nb nanocomposites synthesized by severe plastic deformation. *Acta Materialia* **59**, 7744–7756 (2011).

[57] Zhou, J., Averback, R. & Bellon, P. Stability and amorphization of Cu–Nb interfaces during severe plastic deformation: Molecular dynamics simulations of simple shear. *Acta Materialia* **73**, 116–127 (2014).

[58] Wang, B. & Urbassek, H. M. Phase transitions in an Fe system containing a BCC/FCC phase boundary: An atomistic study. *Physical Review B* **87**, 104108 (2013).

[59] Coleman, S. P. & Spearot, D. E. Atomistic simulation and virtual diffraction characterization of homophase and heterophase alumina interfaces. *Acta Materialia* **82**, 403–413 (2015).

[60] Coleman, S. P., Tschopp, M. A., Weinberger, C. R. & Spearot, D. E. Bridging atomistic simulations and experiments via virtual diffraction: understanding homophase grain boundary and heterophase interface structures. *Journal of Materials Science* **51**, 1251–1260 (2016).

[61] Toby Kelsey, E. & de Leeuw, N. H. Atomistic simulation of dislocations, surfaces and interfaces in MgO. *Journal of the Chemical Society, Faraday Transactions* **92**, 433–438 (1996).

[62] Harding, J., Harris, D. & Parker, S. Computer simulation of general grain boundaries in rocksalt oxides. *Physical Review B* **60**, 2740 (1999).

[63] Phillpot, S. R. & Wolf, D. Grain boundaries in silicon from zero temperature through melting. *Journal of the American Ceramic Society* **73**, 933–937 (1990).

[64] Shenderova, O., Brenner, D. W. & Yang, L. Atomistic simulations of structures and mechanical properties of polycrystalline diamond: Symmetrical $\langle 001 \rangle$ tilt grain boundaries. *Physical Review B* **60**, 7043 (1999).

[65] Wojdyr, M., Khalil, S., Liu, Y. & Szlufarska, I. Energetics and structure of $\langle 001 \rangle$ tilt grain boundaries in SiC. *Modelling and Simulation in Materials Science and Engineering* **18**, 075009 (2010).

[66] Jiang, S., Zhang, H., Zheng, Y. & Chen, Z. Atomistic study of the mechanical response of copper nanowires under torsion. *Journal of Physics D: Applied Physics* **42**, 135408 (2009).

[67] Koh, S. & Lee, H. Molecular dynamics simulation of size and strain rate dependent mechanical response of FCC metallic nanowires. *Nanotechnology* **17**, 3451 (2006).

[68] Weinberger, C. R. & Cai, W. Plasticity of metal nanowires. *Journal of Materials Chemistry* **22**, 3277–3292 (2012).

[69] Arroyo, M. & Belytschko, T. Nonlinear mechanical response and rippling of thick multi-walled carbon nanotubes. *Physical Review Letters* **91**, 215505 (2003).

[70] Xiao, J., Gama, B. & Gillespie, J. An analytical molecular structural mechanics model for the mechanical properties of carbon nanotubes. *International Journal of Solids and Structures* **42**, 3075–3092 (2005).

[71] Weinberger, C. R., Jennings, A. T., Kang, K. & Greer, J. R. Atomistic simulations and continuum modeling of dislocation nucleation and strength in gold nanowires. *Journal of the Mechanics and Physics of Solids* **60**, 84–103 (2012).

[72] Zhang, W. & Smith, J. Nonstoichiometric interfaces and Al_2O_3 adhesion with Al and Ag. *Physical Review Letters* **85**, 3225 (2000).

[73] Subramaniyan, A. K. & Sun, C. Continuum interpretation of virial stress in molecular simulations. *International Journal of Solids and Structures* **45**, 4340–4346 (2008).

[74] Thompson, A. P., Plimpton, S. J. & Mattson, W. General formulation of pressure and stress tensor for arbitrary many-body interaction potentials under periodic boundary conditions. *The Journal of Chemical Physics* **131**, 154107 (2009).

[75] Rycroft, C. Voro++: A three-dimensional Voronoi cell library in C++ (2009).

[76] Olson, G. & Cohen, M. Interphase-boundary dislocations and the concept of coherency. *Acta Metallurgica* **27**, 1907–1918 (1979).

[77] Weatherly, G. & Nicholson, R. An electron microscope investigation of the interfacial structure of semi-coherent precipitates. *Philosophical Magazine* **17**, 801–831 (1968).

[78] Shao, S., Wang, J., Misra, A. & Hoagland, R. G. Spiral patterns of dislocations at nodes in (111) semi-coherent FCC interfaces. *Scientific Reports* **3**, 2448 (2013).

[79] Bramfitt, B. & Marder, A. A transmission-electron-microscopy study of the substructure of high-purity pearlite. *Metallography* **6**, 483–495 (1973).

[80] Takahashi, T., Ponge, D. & Raabe, D. Investigation of orientation gradients in pearlite in hypoeutectoid steel by use of orientation imaging microscopy. *Steel Research International* **78**, 38 (2007).

[81] Zhang, W.-Z. & Purdy, G. O-lattice analyses of interfacial misfit. I. general considerations. *Philosophical Magazine A* **68**, 279–290 (1993).

[82] Bilby, B. & Frank, F. The analysis of the crystallography of martensitic transformations by the method of prism matching. *Acta Metallurgica* **8**, 239–248 (1960).

[83] Zener, C. *et al.* Kinetics of the decomposition of austenite. *Trans. Aime* **167**, 550–595 (1946).

[84] Milstein, F., Fang, H. E. & Marschall, J. Mechanics and energetics of the bain transformation. *Philosophical Magazine A* **70**, 621–639 (1994).

[85] Mehl, R. F. & Hagel, W. C. The austenite: pearlite reaction. *Progress in Metal Physics* **6**, 74–134 (1956).

[86] Hagel, W., Pound, G. & Mehl, R. Calorimetric study of the austenite: pearlite transformation. *Acta Metallurgica* **4**, 37–46 (1956).

[87] Wells, C., Batz, W. & Mehl, R. F. Diffusion coefficient of carbon in austenite. *JOM* **2**, 553–560 (1950).

[88] Verhoeven, J. & Pearson, D. Forced velocity pearlite in high purity Fe-C alloys: Part II. theoretical. *Metallurgical and Materials Transactions A* **15**, 1047–1054 (1984).

[89] Steinbach, I. & Apel, M. The influence of lattice strain on pearlite formation in Fe–C. *Acta Materialia* **55**, 4817–4822 (2007).

[90] Zhang, X. *et al.* Structural transformations among austenite, ferrite and cementite in Fe-C alloys: A unified theory based on ab initio simulations. *Acta Materialia* **99**, 281–289 (2015).

[91] Pandit, A. S. *Theory of the pearlite transformation in steels*. Ph.D. thesis, University of Cambridge (2011).

[92] Das, S., Biswas, A. & Ghosh, R. Volume fraction dependent particle coarsening in plain carbon steel. *Acta Metallurgica et Materialia* **41**, 777–781 (1993).

[93] Deb, P. & Chaturvedi, M. Coarsening behavior of cementite particles in a ferrite matrix in 10b30 steel. *Metallography* **15**, 341–354 (1982).

[94] Kramer, J., Pound, G. & Mehl, R. The free energy of formation and the interfacial enthalpy in pearlite. *Acta Metallurgica* **6**, 763–771 (1958).

[95] Kirchner, H., Mellor, B. & Chadwick, G. A calorimetric determination of the interfacial enthalpy of Cu-In and Cu-Al lamellar eutectoids. *Acta Metallurgica* **26**, 1023–1031 (1978).

[96] Ruda, M., Farkas, D. & Garcia, G. Atomistic simulations in the Fe-C system. *Computational Materials Science* **45**, 550–560 (2009).

[97] Kim, J., Kang, K. & Ryu, S. Characterization of the misfit dislocations at the ferrite/cementite interface in pearlitic steel: An atomistic simulation study. *International Journal of Plasticity* **83**, 302–312 (2016).

[98] Zhou, Y. *et al.* Atomic structure of the Fe/Fe$_3$C interface with the isaichev orientation in pearlite. *Philosophical Magazine* 1–12 (2017).

[99] Martin, A. & Sellars, C. Measurement of interfacial energy from extraction replicas of particles on grain boundaries. *Metallography* **3**, 259–273 (1970).

[100] Zhou, Y. *et al.* Atomic structure of the Fe/Fe$_3$C interface with the Isaichev orientation in pearlite. *Philosophical Magazine* 1–12 (2017).

[101] Kim, J., Kang, K. & Ryu, S. Characterization of the misfit dislocations at the ferrite/cementite interface in pearlitic steel: An atomistic simulation study. *International Journal of Plasticity* **83**, 302–312 (2016).

[102] Guziewski, M., Coleman, S. P. & Weinberger, C. R. Atomistic investigation into the atomic structure and energetics of the ferrite-cementite interface: The Bagaryatskii orientation. *Acta Materialia* **119**, 184–192 (2016).

[103] Guziewski, M., Coleman, S. P. & Weinberger, C. R. Interface energetics and structure of the pearlitic microstructure in steels: An atomistic and continuum investigation. *Acta Materialia* (2018).

[104] Wang, J., Zhang, R., Zhou, C., Beyerlein, I. J. & Misra, A. Characterizing interface dislocations by atomically informed Frank-Bilby theory. *Journal of Materials Research* **28**, 1646–1657 (2013).

[105] Wang, J., Zhang, R., Zhou, C., Beyerlein, I. J. & Misra, A. Interface dislocation patterns and dislocation nucleation in face-centered-cubic and body-centered-cubic bicrystal interfaces. *International Journal of Plasticity* **53**, 40–55 (2014).

[106] Vattré, A. & Demkowicz, M. Determining the Burgers vectors and elastic strain energies of interface dislocation arrays using anisotropic elasticity theory. *Acta Materialia* **61**, 5172–5187 (2013).

[107] Vattré, A. & Demkowicz, M. Effect of interface dislocation Burgers vectors on elastic fields in anisotropic bicrystals. *Computational Materials Science* **88**, 110–115 (2014).

[108] Vattré, A. Elastic interactions between interface dislocations and internal stresses in finite-thickness nanolayered materials. *Acta Materialia* **114**, 184–197 (2016).

[109] Vattré, A. & Pan, E. Interaction between semicoherent interfaces and Volterra-type dislocations in dissimilar anisotropic materials. *Journal of Materials Research* 1–11 (2017).

[110] Modi, O. *et al.* Effect of interlamellar spacing on the mechanical properties of 0.65% C steel. *Materials Characterization* **46**, 347–352 (2001).

[111] Gladman, T., McIvor, I. & Pickering, F. Some aspects of the structure-property relationships in high-C ferrite-pearlite steels. *J. Iron Steel Inst.* **210**, 916–930 (1972).

[112] Q'Donnelly, B., Reuben, R. & Baker, T. Quantitative assessment of strengthening parameters in ferrite-pearlite steels from microstructural measurements. *Metals Technology* **11**, 45–51 (1984).

[113] Kemp, I. Control of mechanical properties in high strain wire drawing of pearlitic steel. In *Materials Forum*, vol. 14, 270–275 (Institute of Metals and Materials Australasia, 1990).

[114] Dollar, M., Bernstein, I. & Thompson, A. Influence of deformation substructure on flow and fracture of fully pearlitic steel. *Acta Metallurgica* **36**, 311–320 (1988).

[115] Janecek, M., Louchet, F., Doisneau-Cottignies, B., Bréchet, Y. & Guelton, N. Specific dislocation multiplication mechanisms and mechanical properties in nanoscaled multilayers: the example of pearlite. *Philosophical Magazine A* **80**, 1605–1619 (2000).

[116] Bae, C. M., Nam, W. L. & Lee, C. S. Effect of interlamellar spacing on the delamination of pearlitic steel wires. *Scripta Materialia* **35**, 641–646 (1996).

[117] Li, Y. *et al.* Atomic-scale mechanisms of deformation-induced cementite decomposition in pearlite. *Acta Materialia* **59**, 3965–3977 (2011).

[118] Carlson, M., Rao, B. N. & Thomas, G. The effect of austenitizing temperature upon the microstructure and mechanical properties of experimental Fe/Cr/C steels. *Metallurgical Transactions A* **10**, 1273–1284 (1979).

[119] Lewandowski, J. J. & Thompson, A. W. Effects of the prior austenite grain size on the ductility of fully pearlitic eutectoid steel. *Metallurgical Transactions A* **17**, 461–472 (1986).

[120] Embury, J. & Fisher, R. The structure and properties of drawn pearlite. *Acta Metallurgica* **14**, 147–159 (1966).

[121] Langford, G. Deformation of pearlite. *Metallurgical Transactions A* **8**, 861–875 (1977).

[122] Zhang, X., Godfrey, A., Huang, X., Hansen, N. & Liu, Q. Microstructure and strengthening mechanisms in cold-drawn pearlitic steel wire. *Acta Materialia* **59**, 3422–3430 (2011).

[123] Sevillano, J. G. Substructure and strengthening of heavily deformed single and two-phase metallic materials. *Journal de Physique III* **1**, 967–988 (1991).

[124] Guziewski, M., Coleman, S. P. & Weinberger, C. R. Atomistic investigation into the mechanical properties of the ferrite-cementite interface: The Bagaryatskii orientation. *Acta Materialia* **144**, 656–665 (2018).

[125] Inoue, A., Ogura, T. & Masumoto, T. Dislocation structures of cementite in cold-rolled c steels. *J. Japan Inst. Metals* **37**, 875–882 (1973).

[126] Cooke, R. & Beevers, C. Slow fatigue crack propagation in pearlitic steels. *Materials Science and Engineering* **13**, 201–210 (1974).

[127] Koreeda, A. & Shimizu, K. Dislocations in cementite. *Philosophical Magazine* **17**, 1083–1086 (1968).

[128] Inoue, A., Ogura, T. & Masumoto, T. Transmission electron microscope study on deformation and fracture of cementite in cold-rolled steels. *Transactions of the Japan Institute of Metals* **17**, 149–157 (1976).

[129] Inoue, A., Ogura, T. & Masumoto, T. Burgers vectors of dislocations in cementite crystal. *Scripta Metallurgica* **11**, 1–5 (1977).

[130] Kar'kina, L., Kar'kin, I. & Kuznetsov, A. Atomistic simulation of stacking faults in (001),(010), and (100) planes of cementite. *The Physics of Metals and Metallography* **115**, 85–97 (2014).

[131] Karkina, L., Karkin, I., Kabanova, I. & Kuznetsov, A. Crystallographic analysis of slip transfer mechanisms across the ferrite/cementite interface in carbon steels with fine lamellar structure. *Journal of Applied Crystallography* **48**, 97–106 (2015).

[132] Mohsenzadeh, M. S. & Mazinani, M. On the yield point phenomenon in low-carbon steels with ferrite-cementite microstructure. *Materials Science and Engineering: A* **673**, 193–203 (2016).

[133] Nikolussi, M., Leineweber, A. & Mittemeijer, E. Microstructure and crystallography of massive cementite layers on ferrite substrates. *Acta Materialia* **56**, 5837–5844 (2008).

[134] Beltz, G. & Rice, J. Dislocation nucleation at metal-ceramic interfaces. *Acta Metallurgica et Materialia* **40**, S321–S331 (1992).

[135] Cepeda-Jimenez, C., Pozuelo, M., Garcia-Infanta, J., Ruano, O. & Carreno, F. Influence of the alumina thickness at the interfaces on the fracture mechanisms of aluminium multilayer composites. *Materials Science and Engineering: A* **496**, 133–142 (2008).

[136] Dauskardt, R., Lane, M., Ma, Q. & Krishna, N. Adhesion and debonding of multi-layer thin film structures. *Engineering Fracture Mechanics* **61**, 141–162 (1998).

[137] Lhuissier, P., Inoue, J. & Koseki, T. Strain field in a brittle/ductile multilayered steel composite. *Scripta Materialia* **64**, 970–973 (2011).

[138] Mishin, Y., Asta, M. & Li, J. Atomistic modeling of interfaces and their impact on microstructure and properties. *Acta Materialia* **58**, 1117–1151 (2010).

[139] Kulkarni, Y. & Asaro, R. J. Are some nanotwinned FCC metals optimal for strength, ductility and grain stability? *Acta Materialia* **57**, 4835–4844 (2009).

[140] Terentyev, D., He, X., Serra, A. & Kuriplach, J. Structure and strength of $\langle 110 \rangle$ tilt grain boundaries in BCC Fe: An atomistic study. *Computational Materials Science* **49**, 419–429 (2010).

[141] Song, H.-y. & Li, Y.-l. Effect of twin boundary spacing on deformation behavior of nanotwinned magnesium. *Physics Letters A* **376**, 529–533 (2012).

[142] Spearot, D. E., Jacob, K. I. & McDowell, D. L. Nucleation of dislocations from [001] bicrystal interfaces in aluminum. *Acta Materialia* **53**, 3579–3589 (2005).

[143] Spearot, D. E., Jacob, K. I. & McDowell, D. L. Dislocation nucleation from bicrystal interfaces with dissociated structure. *International Journal of Plasticity* **23**, 143–160 (2007).

[144] Han, W. *et al.* Deformation and spallation of shocked Cu bicrystals with $\Sigma 3$ coherent and symmetric incoherent twin boundaries. *Physical Review B* **85**, 024107 (2012).

[145] Luo, S.-N., Germann, T. C., Tonks, D. L. & An, Q. Shock wave loading and spallation of copper bicrystals with asymmetric $\Sigma 3$ $\langle 110 \rangle$ tilt grain boundaries. *Journal of Applied Physics* **108**, 093526 (2010).

[146] Luo, S.-N., Germann, T. C., Desai, T. G., Tonks, D. L. & An, Q. Anisotropic shock response of columnar nanocrystalline Cu. *Journal of Applied Physics* **107**, 123507 (2010).

[147] Heino, P. Microstructure and shear strength of a Cu–Ta interface. *Computational Materials Science* **20**, 157–167 (2001).

[148] Lau, T. T. *et al.* Many-body potential for point defect clusters in Fe-C alloys. *Physical Review Letters* **98**, 215501 (2007).

[149] Hepburn, D. J. & Ackland, G. J. Metallic-covalent interatomic potential for carbon in iron. *Physical Review B* **78**, 165115 (2008).

[150] Lee, B.-J. A modified embedded-atom method interatomic potential for the Fe–C system. *Acta Materialia* **54**, 701–711 (2006).

[151] Liyanage, L. S. *et al.* Structural, elastic, and thermal properties of cementite (Fe_3C) calculated using a modified embedded atom method. *Physical Review B* **89**, 094102 (2014).

[152] Henriksson, K. O. & Nordlund, K. Simulations of cementite: An analytical potential for the Fe-C system. *Physical Review B* **79**, 144107 (2009).

[153] Henriksson, K., Björkas, C. & Nordlund, K. Atomistic simulations of stainless steels: a many-body potential for the Fe–Cr–C system. *Journal of Physics: Condensed Matter* **25**, 445401 (2013).

[154] Oganov, A. R. & Glass, C. W. Crystal structure prediction using ab initio evolutionary techniques: Principles and applications. *The Journal of Chemical Physics* **124**, 244704 (2006).

[155] Hirth, J. P. & Lothe, J. *Theory of dislocations* (Krieger Pub. Co, 1982).

[156] Müller, M., Erhart, P. & Albe, K. Analytic bond-order potential for BCC and FCC iron—comparison with established embedded-atom method potentials. *Journal of Physics: Condensed Matter* **19**, 326220 (2007).

[157] Okamoto, H. The C-Fe (carbon-iron) system. *Journal of Phase Equilibria* **13**, 543–565 (1992).

[158] Plimpton, S. Fast parallel algorithms for short-range molecular dynamics. *Journal of Computational Physics* **117**, 1–19 (1995).

[159] Stukowski, A. Visualization and analysis of atomistic simulation data with OVITO–the Open Visualization Tool. *Modelling and Simulation in Materials Science and Engineering* **18**, 015012 (2009).

[160] Nabarro, F. Fifty-year study of the peierls-nabarro stress. *Materials Science and Engineering: A* **234**, 67–76 (1997).

[161] Tolman, R. C. Consideration of the gibbs theory of surface tension. *The Journal of Chemical Physics* **16**, 758–774 (1948).

[162] Wang, Z. *et al.* Atom-resolved imaging of ordered defect superstructures at individual grain boundaries. *Nature* **479**, 380–383 (2011).

[163] Shein, I., Medvedeva, N. & Ivanovskii, A. Electronic and structural properties of cementite-type M_3X (M= Fe, Co, Ni; X= C or B) by first principles calculations. *Physica B: Condensed Matter* **371**, 126–132 (2006).

[164] Chiou, W. C. & Carter, E. A. Structure and stability of Fe_3C-cementite surfaces from first principles. *Surface Science* **530**, 88–100 (2003).

[165] Seki, I. & Nagata, K. Lattice constant of iron and austenite including its supersaturation phase of carbon. *ISIJ international* **45**, 1789–1794 (2005).

[166] Aubry, S., Fitzgerald, S., Dudarev, S. & Cai, W. Equilibrium shape of dislocation shear loops in anisotropic α-Fe. *Modelling and Simulation in Materials Science and Engineering* **19**, 065006 (2011).

[167] Wood, I. *et al.* Thermal expansion and crystal structure of cementite, fe3c, between 4 and 600 k determined by time-of-flight neutron powder diffraction. *Journal of Applied Crystallography* **37**, 82–90 (2004).

[168] Mauger, L. *et al.* Phonons and elasticity of cementite through the Curie temperature. *Physical Review B* **95**, 024308 (2017).

[169] Dever, D. Temperature dependence of the elastic constants in α-iron single crystals: relationship to spin order and diffusion anomalies. *Journal of Applied Physics* **43**, 3293–3301 (1972).

[170] Hyde, B., Espinosa, H. D. & Farkas, D. An atomistic investigation of elastic and plastic properties of Au nanowires. *JOM* **57**, 62 (2005).

[171] Morriss, G. P. & Evans, D. J. *Statistical Mechanics of Nonequilbrium Liquids* (ANU Press, 2013).

[172] Daivis, P. J. & Todd, B. A simple, direct derivation and proof of the validity of the SLLOD equations of motion for generalized homogeneous flows. *The Journal of Chemical Physics* **124**, 194103 (2006).

[173] Stukowski, A. & Albe, K. Extracting dislocations and non-dislocation crystal defects from atomistic simulation data. *Modelling and Simulation in Materials Science and Engineering* **18**, 085001 (2010).

[174] Honeycutt, J. D. & Andersen, H. C. Molecular dynamics study of melting and freezing of small Lennard-Jones clusters. *Journal of Physical Chemistry* **91**, 4950–4963 (1987).

[175] Zimmerman, J., Kelchner, C., Klein, P., Hamilton, J. & Foiles, S. Surface step effects on nanoindentation. *Physical Review Letters* **87**, 165507 (2001).

[176] Begau, C., Hua, J. & Hartmaier, A. A novel approach to study dislocation density tensors and lattice rotation patterns in atomistic simulations. *Journal of the Mechanics and Physics of Solids* **60**, 711–722 (2012).

[177] Shimizu, F., Ogata, S. & Li, J. Theory of shear banding in metallic glasses and molecular dynamics calculations. *Materials Transactions* **48**, 2923–2927 (2007).

[178] Greer, J. R., Weinberger, C. R. & Cai, W. Comparing the strength of FCC and BCC submicrometer pillars: Compression experiments and dislocation dynamics simulations. *Materials Science and Engineering: A* **493**, 21–25 (2008).

[179] Kunz, A., Pathak, S. & Greer, J. R. Size effects in al nanopillars: Single crystalline vs. bicrystalline. *Acta Materialia* **59**, 4416–4424 (2011).

[180] Sevillano, J. G. Room temperature plastic deformation of pearlitic cementite. *Materials Science and Engineering* **21**, 221–225 (1975).

[181] Coleman, S. P., Sichani, M. M. & Spearot, D. E. A computational algorithm to produce virtual x-ray and electron diffraction patterns from atomistic simulations. *JOM* **66**, 408–416 (2014).